



저작자표시-비영리-변경금지 2.0 대한민국

이용자는 아래의 조건을 따르는 경우에 한하여 자유롭게

- 이 저작물을 복제, 배포, 전송, 전시, 공연 및 방송할 수 있습니다.

다음과 같은 조건을 따라야 합니다:



저작자표시. 귀하는 원저작자를 표시하여야 합니다.



비영리. 귀하는 이 저작물을 영리 목적으로 이용할 수 없습니다.



변경금지. 귀하는 이 저작물을 개작, 변형 또는 가공할 수 없습니다.

- 귀하는, 이 저작물의 재이용이나 배포의 경우, 이 저작물에 적용된 이용허락조건을 명확하게 나타내어야 합니다.
- 저작권자로부터 별도의 허가를 받으면 이러한 조건들은 적용되지 않습니다.

저작권법에 따른 이용자의 권리는 위의 내용에 의하여 영향을 받지 않습니다.

이것은 [이용허락규약\(Legal Code\)](#)을 이해하기 쉽게 요약한 것입니다.

[Disclaimer](#)

공학박사학위논문

스트레인 및 진동 측정을 위한
직접 인쇄 나노물질 센서

Directly Printed Nanomaterial Sensor for Strain
and Vibration Measurement

2020년 8월

서울대학교 대학원

기계공학부

민 수 홍

스트레인 및 진동 측정을 위한 직접 인쇄 나노물질 센서

Directly Printed Nanomaterial Sensor for Strain
and Vibration Measurement

지도교수 안 성 훈

이 논문을 공학박사 학위논문으로 제출함
2020년 4월

서울대학교 대학원
기계공학부
민 수 홍

민수홍의 공학박사 학위논문을 인준함
2020년 6월

위 원 장 : 박 희 재 (인)

부위원장 : 안 성 훈 (인)

위 원 : 차 석 원 (인)

위 원 : 이 윤 석 (인)

위 원 : 이 길 용 (인)

Abstract

Directly Printed Nanomaterial Sensor for Strain and Vibration Measurement

Soo–Hong Min

Department of Mechanical Engineering

The Graduate School

Seoul National University

Most discussions about Industrie 4.0 tacitly assume that any such system would involve the processing and evaluation of large data volumes. Specifically, the operation of complex production processes requires stable and reliable data measurement and communication systems. However, while modern sensor technology may already be capable of collecting a wide range of machine and production data, it has been proving difficult to measure and analyse the data which is not easy to measurable and feed the results quickly back into an optimised production cycle. This is why the cost and installation of sensor, data acquisition, and transmission systems for flexible and adaptive manufacturing process have not been match the requirement of industrial demands.

In this dissertation, directly printed nanomaterial sensor capable of strain and vibration measurement with high sensitivity and wide measurable range was fabricated using aerodynamically focused nanomaterial (AFN) printing system which is a direct printing technique for conductive and stretchable pattern printing onto flexible substrate. Specifically, microscale porous conductive pattern composed of silver nanoparticles (AgNPs) and multi-walled carbon nanotubes (MWCNTs) composite was printed onto polydimethylsiloxane (PDMS).

Printing mechanism of AFN printing system for nanocomposite onto flexible substrate in order of mechanical crack generation, seed layer deposition, partial aggregation, and fully deposition was demonstrated and experimentally validated. The printed nanocomposite sensor exhibited gauge factor (GF) of 58.7, measurable range of 0.74, and variance in peak resistance under 0.05 during 1,000 times life cycle evaluation test. Furthermore, vibration measurement performance was evaluated according to vibration amplitude and frequency with Q-factor evaluation and statistical verification.

Sensing mechanism for nanocomposite sensor was also analysed and discussed by both analytical and statistical methods. First, electron tunnelling effect among nanomaterials was analysed statistically using bivariate probit model. Since electrical property varies by the geometrical properties of nanomaterial, Monte Carlo simulation method based on Lennard-Jones (LJ) potential model and the voter model was developed for deeper understanding of the

dynamics of nanomaterial by strain. By simply counting the average attachment among nanomaterials by strain, electrical conductivity was easily estimated with low simulation cost.

The main objective of all processes to manufacture high-tech products is compliance with the specified ranges of permissible variation. In this perspective, all data must be recorded that might provide some evidence of status changes anywhere along the process chain. This dissertation covers the monitoring of forming and milling process. By measurement of mechanical deformation of stamp during forming process, it was possible to estimate the forming force according to various process parameters including maximum force, force gradient, and the thickness of sheet metal.

Furthermore, accurate and reliable vibration monitoring was also conducted during milling process by simple and direct attachment of printed sensor to workpiece. Using frequency and power spectrum analysis of obtained data, the vibration of workpiece was measured during milling process according to process parameters including RPM, feed rate, cutting depth and width of spindle. Finally, developed sensor was applied to the digital twin of turbine blade manufacturing that vibration greatly affects the quality of product to predict the process defects in real time.

To overcome the wire required data acquisition and transmission system, directly printed wireless communication sensor was also developed using chipless radio frequency identification (RFID) technology. It is one of the widely used technique for internet-of-things (IoT) devices due to low-cost, printability, and simplicity. The

developed stretchable and chipless RFID sensor exhibited GF more than 0.6 and maximum measurable range more than 0.2 with high degree-of-freedom of motion. Since it showed its original characteristics of sensing in only one direction independently, sensor patch composed of various sensor with different resonance frequency was capable of measuring not only normal strains but also shear strains in all directions.

Sensors in machinery and equipment can provide valuable clues as to whether or not the actual values will fall into the tolerance range. In this aspect, a real-time, accurate, and reliable process monitoring is a basic and crucial enabler of intelligent manufacturing operations and digital twin applications. In this dissertation, developed sensor was used for various manufacturing process include forming process, milling process, and wireless communication using highly sensitive and wide measuring properties with low fabrication cost. It is expected that developed sensor could be applied for the digital twin and process defects prediction in real-time.

Keywords: Sensor, Nanomaterial, AFN printing, Sensitivity, Stretchability, Process monitoring, Smart manufacturing

Student Number: 2016-20684

Table of Contents

| | |
|---|------------|
| Chapter 1. Introduction..... | 1 |
| 1.1. Toward smart manufacturing | 1 |
| 1.2. Sensor in manufacturing | 4 |
| 1.3. Research objective | 11 |
| Chapter 2. Background | 16 |
| 2.1. Aerodynamically focused nanomaterial printing | 16 |
| 2.2. Printing system envelope | 26 |
| 2.3. Highly sensitive sensor printing | 34 |
| Chapter 3. Sensor fabrication and evaluation | 42 |
| 3.1. Highly sensitive and wide measuring sensor printing..... | 42 |
| 3.2. Sensing performance evaluation | 59 |
| 3.3. Environmental and industrial evaluation..... | 87 |
| Chapter 4. Sensing mechanism analysis..... | 97 |
| 4.1. Theoretical background | 97 |
| 4.2. Statistical regression analysis..... | 101 |
| 4.3. Monte Carlo simulation | 104 |
| Chapter 5. Application to process monitoring | 126 |
| 5.1. Forming process monitoring..... | 126 |
| 5.2. Milling process monitoring | 133 |
| 5.3. Wireless communication monitoring | 149 |
| Chapter 6. Conclusion..... | 185 |
| Bibliography | 192 |
| Abstract in Korean | 211 |

List of Tables

| | |
|--|----|
| Table 1.1. Description of Industrie 4.0 | 2 |
| Table 1.2. Examples of manufacturing process monitoring by sensing type | 6 |
| Table 1.3. Requirements of sensor for smart manufacturing with respect to SMEs | 7 |
| Table 1.4. Performance indicators for piezoresistive type strain and vibration sensor | 12 |
| Table 1.5. Previous researches of multivariate measurable sensor | 13 |
| Table 2.1. Evaluation of direct printing technology for sensor fabrication | 18 |
| Table 2.2. Review of low temperature nanomaterial printing process | 19 |
| Table 2.3. Description of AFN process and its effect to fabricated sensor | 20 |
| Table 2.4. Process parameters of AFN printing process | 28 |
| Table 3.1. Material–substrate compatibility of AFN printing process | 42 |
| Table 3.2. Material–substrate compatibility of AFN printing process focused on AgNP, MWCNT, and AgNP/MWCNT composite | 43 |
| Table 3.3. Optimised design variables for fabrication of highly sensitive and wide measuring sensor..... | 56 |
| Table 3.4. The resistance and resolution of electrical components for experimental setup... | 61 |
| Table 3.5. The reliability evaluation results during life–cycle test | 64 |
| Table 3.6. The results of frequency response of printed sensor according to induced frequency with Q–factor at 70.7% | 75 |
| Table 3.7. The statistical results of printed sensor according to induced frequency with 200 Hz | 77 |

| | |
|---|-----|
| Table 3.8. The statistical results of printed sensor according to induced frequency with 400 Hz..... | 78 |
| Table 3.9. The statistical results of printed sensor according to induced frequency with 600 Hz..... | 78 |
| Table 3.10. The results of p-value and Cronbach's alpha according to induced frequency..... | 80 |
| Table 3.11. The statistical analysis of RMS value of life cycle evaluation test..... | 83 |
| Table 3.12. The datasheet of fabricated sensor in comparison to commercial sensor | 94 |
| Table 3.13. Evaluation of cost of fabricated sensor according to cost-based pricing method | 95 |
| Table 3.14. Evaluation of sensor based on low-cost smart sensor indicator for SMEs..... | 96 |
| Table 4.1. The geometrical properties of nanomaterial used for Monte Carlo simulation method | 109 |
| Table 4.2. The simulation parameter used for Monte Carlo simulation method | 110 |
| Table 4.3. Characteristics and limitations of suggested model in comparison to other simulation method | 118 |
| Table 5.1. The process parameters of forming process monitoring..... | 128 |
| Table 5.2. The process parameters of milling process monitoring..... | 138 |
| Table 5.3. The design parameters of resonance circuit printing | 161 |

List of Figures

| | |
|---|----|
| Figure 1.1. The capable indices of various fields by Industrie 4.0..... | 2 |
| Figure 1.2. The schematic diagram of sensor-enabled smart manufacturing | 5 |
| Figure 1.3. The sensor-enabled process monitoring for process optimisation..... | 7 |
| Figure 1.4. Toward appropriate smart sensor..... | 10 |
| Figure 1.5. Previous researches of sensor according to measruable range and gauge factor | 12 |
| Figure 1.6. Technological approach for this dissertation | 15 |
| Figure 2.1. The schematic diagram of sensing mechanism for piezoresistive type sensor fabricated by (a) solvent required, (b) high temperature, and (c) AFN printing process | 16 |
| Figure 2.2. Categorisation of direct printing technology for sensor fabrication by printing source | 17 |
| Figure 2.3. The principle of AFN printing process by successive repetition of excitation and purging | 20 |
| Figure 2.4. Time sequence of excitation and purging of aerosol control in AFN printing process..... | 20 |
| Figure 2.5. The free body diagram of drag and Saffman's lift forces for the upstream in the nozzle | 22 |
| Figure 2.6. The free body diagram of drag and centrifugal forces for the downstream in the nozzle | 23 |
| Figure 2.7. Schematic diagram of AFN printing system..... | 26 |
| Figure 2.8. The photograph of AFN printing system | 27 |
| Figure 2.9. The measurement results of pressure of chamber and feeder during AFN printing process | 29 |

| | |
|---|----|
| Figure 2.10. The optical microscopic image of AFN printed pattern with (a) concentric shape and (b) number “3” shapes..... | 30 |
| Figure 2.11. The optical microscopie image of AFN printed line pattern with pattern width of (a) 16.31, (b) 27.8, (c) 49.29 μm | 30 |
| Figure 2.12. The measurement results of packing ratio of AFN printed pattern with respect to the scan velocity | 32 |
| Figure 2.13. The measurement results of relative electrical resistance of AFN printed pattern with respect to the scan velocity | 32 |
| Figure 2.14. The schematic diagram of fabrication process of highly sensitive sensor composed of AgNP..... | 34 |
| Figure 2.15. The photograph of fabricated highly sensitive sensor | 35 |
| Figure 2.16. The confocal microscopic image of highly sensitive sensor | 36 |
| Figure 2.17. (a) SEM image of highly sensitive sensor and (b) its magnified view..... | 36 |
| Figure 2.18. The photograph of experimental setup for sensing performance evaluation based on standardised 4–points bending method | 37 |
| Figure 2.19. The evaluation results of sensing performance of highly sensitive sensor | 38 |
| Figure 2.20. The schematic diagram of sensing mechanism for highly sensitive sensor | 39 |
| Figure 2.21. SEM image of mechanical crack in highly sensitive sensor | 40 |
| Figure 2.22. State–of–the–art and research objective according to GF and maximum strain limit..... | 41 |
| Figure 3.1. The printing principle according to impact | |

| | |
|--|----|
| velocity and particle diameter..... | 45 |
| Figure 3.2. The schematic diagram for the observation of interfacial layer..... | 46 |
| Figure 3.3. The photograph of experimental setup for micro–machining for detaching printed pattern..... | 46 |
| Figure 3.4. SEM image of mechanical crack in interfacial layer..... | 47 |
| Figure 3.5. The schematic diagram of printing mechanism of nanocomposite composed of AgNPs and MWCNTs on flexible substrate..... | 47 |
| Figure 3.6. SEM image of nanocomposite printing by printing steps..... | 48 |
| Figure 3.7. The schematic diagram of AFN printed pattern by printing steps to investigate printing mechanism | 49 |
| Figure 3.8. The optical microscopic image of AFN printed pattern by printing steps to investigate printing mechanism | 50 |
| Figure 3.9. SEM image of nanocomposite printing in order of (a) seed layer deposition, (b) partial aggregation, and (c) fully deposition | 50 |
| Figure 3.10. SEM image of nanoparticle printing in order of (a), (b), and (c) | 51 |
| Figure 3.11. The free body diagram of drag and Saffman’s lift forces for CNT in the upstream of the nozzle..... | 51 |
| Figure 3.12. The free body diagram of drag and centrifugal forces for CNT in the downstream of the nozzle | 52 |
| Figure 3.13. The optical microscopic image of nanocomposite printing by printing steps | 53 |
| Figure 3.14. The confocal microscopic image of nanocomposite printing by printing steps | 54 |
| Figure 3.15. The schematic diagram of fabrication | |

| | |
|--|----|
| process of highly sensitive and wide measuring sensor | 55 |
| Figure 3.16. Design variables for the fabrication of highly sensitive and wide measuring sensor .. | 56 |
| Figure 3.17. The photograph of fabricated highly sensitive and wide measuring sensor | 57 |
| Figure 3.18. The optical microscopic image of fabricated highly sensitive and wide measuring sensor ... | 58 |
| Figure 3.19. The schematic diagram of strain sensing mechanism of nanocomposite sensor | 59 |
| Figure 3.20. The schematic diagram of experimental setup for strain sensing performance evaluation | 60 |
| Figure 3.21. The photograph of experimental setup for strain sensing performance evaluation | 60 |
| Figure 3.22. The evaluation results of sensing performance of highly sensitive and wide measuring sensor | 61 |
| Figure 3.23. (a) The evaluation results of life-cycle test for highly sensitive and wide measuring sensor and (b) its magnified view | 63 |
| Figure 3.24. The evaluation results for average and standard deviation value during life-cycle test according to strain | 64 |
| Figure 3.25. The experimental results of sensitivity and stretchability according to composition ratio | 66 |
| Figure 3.26. The experimental results of sensitivity and stretchability according to scan time | 66 |
| Figure 3.27. The results of this research according to GF and maximum strain limit in comparison to state-of-the-art | 67 |
| Figure 3.28. The schematic diagram of vibration sensing mechanism of nanocomposite sensor | 68 |
| Figure 3.29. The experimental results of relative | |

| | |
|---|----|
| resistance change of printed sensor by various vibrations with amplitude of 8 μm | 69 |
| Figure 3.30. FFT results of relative resistance change of printed sensor by vibration amplitude of 8 μm and frequency of 100 Hz..... | 69 |
| Figure 3.31. FFT results of relative resistance change of printed sensor by vibration amplitude of 8 μm and frequency of 200 Hz..... | 70 |
| Figure 3.32. FFT results of relative resistance change of printed sensor by vibration amplitude of 8 μm and frequency of 400 Hz..... | 70 |
| Figure 3.33. The experimental results of relative resistance change of printed sensor by various vibration with frequency of 200 Hz.... | 71 |
| Figure 3.34. FFT results of relative resistance change of printed sensor by vibration amplitude of 4 μm and frequency of 200 Hz..... | 72 |
| Figure 3.35. FFT results of relative resistance change of printed sensor by vibration amplitude of 8 μm and frequency of 200 Hz..... | 72 |
| Figure 3.36. FFT results of relative resistance change of printed sensor by vibration amplitude of 12 μm and frequency of 200 Hz | 73 |
| Figure 3.37. The bandwidth of amplitude power spectrum of 100 Hz vibration at Q-factor at 70.7%..... | 74 |
| Figure 3.38. The evaluation results of frequency response of printed sensor according to induced frequency with Q-factor at 70.7% | 74 |
| Figure 3.39. The normalised evaluation results of frequency response of printed sensor according to induced frequency with Q-factor at 70.7% | 75 |
| Figure 3.40. The comparison of amplitude by frequency of printed sensor to commercial accelerometer . | 80 |

| | |
|--|----|
| Figure 3.41. The 3dB test of printed sensor for evaluation of dynamic performance | 81 |
| Figure 3.42. The life cycle evaluation test of vibration sensing | 82 |
| Figure 3.43. The RMS value of life cycle evaluation test of vibration sensing..... | 82 |
| Figure 3.44. The relative resistance change by time according to vibration direction..... | 83 |
| Figure 3.45. The RMS value of relative resistance change by time according to vibration direction..... | 84 |
| Figure 3.46. The results of this research according to frequency and measurable range in comparison to state-of-the-art..... | 85 |
| Figure 3.47. The results of this research in comparison to interoperable sensor..... | 86 |
| Figure 3.48. The XRD measurement results of highly sensitive sensor..... | 87 |
| Figure 3.49. The DSC measurement results of highly sensitive sensor | 88 |
| Figure 3.50. The XRD measurement results of highly sensitive and wide measuring sensor..... | 89 |
| Figure 3.51. The DSC measurement results of highly sensitive and wide measuring sensor..... | 90 |
| Figure 3.52. The photograph of experimental setup for temperature and humidity characterisation of AFN printed sensor | 90 |
| Figure 3.53. The measurement results of relative resistance change of highly sensitive sensor according to temperature | 91 |
| Figure 3.54. The measurement results of relative resistance change of highly sensitive sensor according to relative humidity | 92 |
| Figure 3.55. The measurement results of relative resistance change of highly sensitive and | |

| | |
|--|-----|
| wide measuring sensor according to temperature | 92 |
| Figure 3.56. The measurement results of relative resistance change of highly sensitive and wide measuring sensor according to relative humidity..... | 93 |
| Figure 4.1. The schematic diagram of electron tunnelling effect between NPs | 98 |
| Figure 4.2. The schematic diagram of mechanical attachment between (a) NPs, (b) NP and CNT, and (C) CNTs | 99 |
| Figure 4.3. The validation of model by comparison of model value to experimental value with respect to composition ratio of AgNPs and MWCNTs | 103 |
| Figure 4.4. The flowcharts of Monte Carlo simulation method for electrical conductivity calculation of nanocomposite..... | 107 |
| Figure 4.5. The optimised distribution of nanocomposite simulation domain with minimised energy..... | 110 |
| Figure 4.6. A magnified view of optimised nanocomposite distribution with minimised energy..... | 111 |
| Figure 4.7. The distribution of simulated AgNPs according to diameter | 112 |
| Figure 4.8. The distribution of simulated CNTs according to diameter | 113 |
| Figure 4.9. The distribution of simulated CNTs according to length..... | 113 |
| Figure 4.10. The simulation results of average electrical attachment with various composition ratio of nanocomposite according to strain | 114 |

| | |
|--|-----|
| Figure 4.11. The simulation results of average electrical attachment with various packing ratio of nanocomposite according to strain... | 115 |
| Figure 4.12. Comparison of simulation results of change of electrical conductivity by strain to experimental values of GF by composition ratio | 116 |
| Figure 4.13. Comparison of simulation results of change of electrical conductivity by strain to experimental values of GF by packing ratio . | 117 |
| Figure 4.14. The flowchart of Monte Carlo simulation method for vibration sensing of nanocomposite..... | 120 |
| Figure 4.15. The simulation results of relative resistance change at vibration with 100 Hz.. | 121 |
| Figure 4.16. The simulation results of relative resistance change at vibration with 200 Hz.. | 121 |
| Figure 4.17. The simulation results of relative resistance change at vibration with 400 Hz.. | 122 |
| Figure 4.18. Comparison of simulation results of Frequency to experimental values by induced frequency | 123 |
| Figure 4.19. Comparison of simulation results of amplitude to experimental values by induced frequency | 123 |
| Figure 4.20. Comparison of simulation results of frequency to experimental values by induced amplitude | 124 |
| Figure 4.21. Comparison of simulation results of amplitude to experimental values by induced amplitude | 125 |
| Figure 5.1. The schematic diagram of mechanical deformation of stamp during forming process . | 127 |
| Figure 5.2. The photograph of experimental setup for | |

| | |
|--|-----|
| forming process monitoring using printed sensor | 128 |
| Figure 5.3. Comparison of relative resistance change of sensor to force obtained by dynamometer according to maximum force..... | 129 |
| Figure 5.4. Comparison of relative resistance change of sensor to force obtained by dynamometer according to force gradient..... | 130 |
| Figure 5.5. Comparison of relative resistance change of sensor to force obtained by dynamometer according to metal thickness | 130 |
| Figure 5.6. The photograph of formed sheet metal fabricated by rubber forming process | 132 |
| Figure 5.7. The surface profile measurement results of channel of formed sheet metal fabricated by rubber forming process..... | 132 |
| Figure 5.8. The photograph of experimental setup for milling process monitoring using printed sensor | 134 |
| Figure 5.9. Comparison of relative resistance change of sensor to vibration obtained by accelerometer in x-direction | 135 |
| Figure 5.10. Comparison of relative resistance change of sensor to vibration obtained by accelerometer in y-direction..... | 135 |
| Figure 5.11. Comparison of relative resistance change of sensor to vibration obtained by accelerometer in z-direction | 136 |
| Figure 5.12. Comparison of power spectrum of relative resistance change to vibration in x-direction | 137 |
| Figure 5.13. Comparison of power spectrum of relative resistance change to vibration in y-direction | 137 |

| | |
|---|-----|
| Figure 5.14. Comparison of power spectrum of relative resistance change to vibration in z-direction | 138 |
| Figure 5.15. Comparison of power spectrum of relative resistance change to vibration according to RPM..... | 139 |
| Figure 5.16. Comparison of power spectrum of relative resistance change to vibration according to feed rate | 139 |
| Figure 5.17. Comparison of power spectrum of relative resistance change to vibration according to cutting depth of spindle..... | 140 |
| Figure 5.18. Comparison of power spectrum of relative resistance change to vibration according to cutting width of spindle..... | 140 |
| Figure 5.19. The photograph of experimental setup of turbine blade milling process monitoring using printed sensor | 142 |
| Figure 5.20. The schematic diagram of turbine blade milling process in order of (a) pre-finishing and (b) finishing | 142 |
| Figure 5.21. The schematic diagram of real time data processing of relative resistance change of sensor | 144 |
| Figure 5.22. The schematic diagram of real time data fusion of tool path data and processed sensor data..... | 144 |
| Figure 5.23. The photograph of fabricated turbin blade with good surface quality | 146 |
| Figure 5.24. The sensor data visualisation of turbine blade with good surface quality | 146 |
| Figure 5.25. The photograph of fabricated turbin blade with bad surface quality..... | 147 |
| Figure 5.26. The sensor data visualisation of turbine blade | |

| | |
|---|-----|
| with bad surface quality | 147 |
| Figure 5.27. The schematic diagram of fabrication process for stretchable and wireless communication sensor | 150 |
| Figure 5.28. The optical microscopic image of stretchable and wireless communication sensor printed by printed steps..... | 151 |
| Figure 5.29. The photograph of fabricated stretchable and wireless communication sensor | 152 |
| Figure 5.30. The optical microscopic image of finger capacitor in stretchable and wireless communication sensor | 153 |
| Figure 5.31. The photograph of stretching motion of stretchable and wireless communication sensor..... | 153 |
| Figure 5.32. The photograph of twisting motion of stretchable and wireless communication sensor..... | 154 |
| Figure 5.33. The photograph of folding motion of stretchable and wireless communication sensor..... | 154 |
| Figure 5.34. The schematic diagram of VNA of stretchable and wireless communication sensor..... | 155 |
| Figure 5.35. The photograph of experimental setup for VNA of stretchable and wireless communication sensor | 158 |
| Figure 5.36. The experimental results of voltage gain of resonance circuit by frequency according to finger gap | 162 |
| Figure 5.37. The experimental results of voltage gain of resonance circuit by frequency according to finger length..... | 162 |
| Figure 5.38. The experimental results of voltage | |

| | |
|--|-----|
| gain of resonance circuit by frequency according to outer diameter | 163 |
| Figure 5.39. The experimental results of voltage gain of resonance circuit by frequency according to turn width..... | 163 |
| Figure 5.40. The experimental results of resonance frequency of AFN printed circuit by finger gap | 164 |
| Figure 5.41. The experimental results of resonance frequency of AFN printed circuit by finger length..... | 164 |
| Figure 5.42. The experimental results of resonance frequency of AFN printed circuit by outer diameter | 165 |
| Figure 5.43. The experimental results of resonance frequency of AFN printed circuit by turn width..... | 165 |
| Figure 5.44. (a) The schematic diagram of resonance circuit stretching and (b) the photograph of 3D printed jig for stretching | 166 |
| Figure 5.45. The experimental results of RCS spectrum during resonance circuit stretching in horizontal direction..... | 167 |
| Figure 5.46. The schematic diagram of inductance and capacitance behaviour of resonance circuit | 167 |
| Figure 5.47. The experimental results of resonance frequency of printed circuit by tensile strain in horizontal direction..... | 169 |
| Figure 5.48. The experimental results of frequency shift ratio of printed circuit by tensile strain in horizontal direction | 169 |
| Figure 5.49. The experimental results of resonance frequency of printed circuit by tensile strain | |

| | |
|--|-----|
| in vertical direction | 170 |
| Figure 5.50. The experimental results of frequency shift ratio of printed circuit by tensile strain in vertical direction | 170 |
| Figure 5.51. The schematic diagram of normal strain sensing in each direction explained by Mohr's circle | 172 |
| Figure 5.52. The photograph of fabricated normal strain sensor composed of two perpendicular resonance circuit | 172 |
| Figure 5.53. The experimental results of RCS spectrum of stretchable and wireless communication sensor for normal strain in horizontal direction | 174 |
| Figure 5.54. The experimental results of RCS spectrum of stretchable and wireless communication sensor for normal strain in 30 ° direction.... | 174 |
| Figure 5.55. The experimental results of RCS spectrum of stretchable and wireless communication sensor for normal strain in 45 ° direction.... | 175 |
| Figure 5.56. The experimental results of RCS spectrum of stretchable and wireless communication sensor for normal strain in 60 ° direction.... | 175 |
| Figure 5.57. The experimental results of RCS spectrum of stretchable and wireless communication sensor for normal strain in vertical direction | 176 |
| Figure 5.58. The experimental results of frequency shift ratio of stretchable and wireless communication sensor by normal strain | 176 |
| Figure 5.59. The schematic diagram of shear strain sensing in each direction explained by Mohr's circle | 178 |
| Figure 5.60. The photograph of fabricated shear strain sensor composed of three resonance circuit | 178 |

| | |
|--|-----|
| Figure 5.61. The experimental results of RCS spectrum of stretchable and wireless communication sensor for shear strain in 45 ° direction..... | 179 |
| Figure 5.62. The experimental results of RCS spectrum of stretchable and wireless communication sensor for shear strain in 60 ° direction..... | 180 |
| Figure 5.63. The experimental results of RCS spectrum of stretchable and wireless communication sensor for shear strain in 75 ° direction..... | 180 |
| Figure 5.64. The experimental results of frequency shift ratio of stretchable and wireless communication sensor by shear strain..... | 181 |
| Figure 5.65. The schematic diagram of strain measurement of air tube by stretchable and wireless communication sensor | 183 |
| Figure 5.66. The photograph of printed stretchable and wireless communication sensor onto air tube | 183 |
| Figure 5.67. The experimental results of RCS spectrum of stretchable and wireless communication sensor by air blowing of air tube | 184 |

Chapter 1. Introduction

1.1. Toward smart manufacturing

Industrie 4.0 is a newly emerging paradigm which can change human life in various aspects [1, 2]. Manufacturing is one of the most potential fields with the change followed by Industrie 4.0 in terms of not only digitisation and automation of manufacturing process but also the digital twin and predictive maintenance as shown in **figure 1.1** [3]. Environments in which machines, production systems, databases, and simulation systems can communicate with each other and share data and services. Human users can use mobile devices to access the process and can interact with all subsystems, control these systems or request specific data.

Such decentralised and modular systems allow engineers to plan, implement, monitor and configure individual manufacturing processes as well as entire process chains quickly and cost-effectively [4, 5]. Efficient networks allow the provision of flexible and easily adjustable systems for all stages of the customised production cycle, from the drawing board to the recycling facility. With comprehensive technological knowledge and understanding of individual processes as well as integrated process chains in the pilot lines, virtual representations of each process and processing status can be delivered anywhere along the production chain.

Table 1. Description of Industrie 4.0

| Industrie 1.0 | Industrie 2.0 | Industrie 3.0 | Industrie 4.0 |
|---|--|--|--|
| Mechanisation and the introduction of steam and water power | Mass production assembly lines using electricity | Automated production, computers, IT-Systems and robotics | Smart factory, autonomous systems, IoT, machine learning |

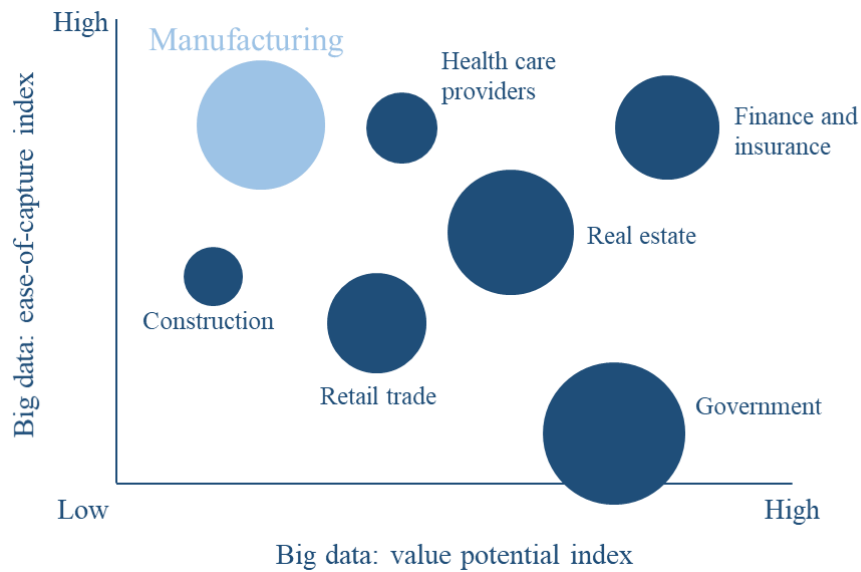


Figure 1.1. The capable indices of various fields by Industrie 4.0 [3]

Not only does networked and adaptive production improve production by making additional knowledge available, but it also opens up the possibility of completely new forms of economic value added via extended or completely new physical processes and products [6, 7]. Digital and data-based business models can be developed, classified, and evaluated even for digital services such as machining-as-a-service or power-by-the-hour.

Digital assistance systems and technology applications in networked and adaptive production operations help engineers to monitor the data, to control process conditions and to apply their personal skills and competences with maximum efficiency [8]. Visualization tools such as phones, tablets and smart glasses can provide immediate information, allowing flexible adjustments and quick changes of production plans or processes.

Data from model-based simulations optimise the decision making about possible improvements of products and processes [9, 10]. The software detects critical situations during the manufacturing process and accounts for frequent changes of product specifications, allowing the process planning to reach high levels of efficiency even before the first component leaves the production line. Constant checks and comparisons of real data and matching simulation data ensure that the models are continuously improved, allowing the improvement of quality and performance of the end-product.

1.2. Sensor in manufacturing

Data acquisition is the first step on the way to networked and adaptive production [13, 14]. It is vital to establish which data can be recorded directly in the control unit of the production machine concerned and which can only be obtained via additional sensors. When additional sensors are required to measure parameters such as temperature, speed or pressure for example, these must be integrated robustly and reliably within the manufacturing process. The data from sensors detects the critical situations during the manufacturing process and accounts for frequent changes of product specifications in the production of prototypes or small series, allowing the process planning to reach high levels of efficiency with direct benefits for the quality and performance of the end-product.

All data from the sensors and the production system will be stored individually for each product, creating a digital twin that retains a full production history including project data and order specifications [15, 16]. Identification systems allow this twin to be assigned to the individual component, making it available for every downstream process steps. The extended product data models provide relevant, context-specific data from the manufacturing history for further analyses, accelerating process development and process optimization in the production of prototypes as well as large series.



Figure 1.2. The schematic diagram of sensor-enabled smart manufacturing

Despite the benefit of Industrie 4.0 and its technologies, especially small and medium-sized enterprises (SMEs) seem to struggle with their implementation [17, 18]. This is due to SMEs' lower available resources leading to a high demand of cost-efficiency and their limited experience in managing new technologies in comparison to large companies [19, 20]. In addition, SMEs often follow a short-term strategy which increases the risks of long-term investments with fuzzy revenues as it is often the case for investments in Industrie 4.0 technologies. This leads to the fact that the smaller SMEs are, the higher is the risk for them to fall behind on technological advance within Industrie 4.0, smart manufacturing, and digitisation.

Table 1.2. Examples of manufacturing process monitoring by sensing type

| Process | Example | Defect | Sensor mounting | Sensing type |
|-----------|----------------------|--|--|---------------------------------------|
| Forming | Rubber forming | Wrinkle, Seizure, | Workpiece, Stamp, Die | Strain, Force, Pressure |
| | Hydraulic forming | Dimension error | | |
| Machining | Milling | Burr, | Workpiece, Tool, Tool holder, Clamp, Machine | Strain, Force, Vibration, Temperature |
| | Turning | Seizure, | | |
| | Grinding | Scratch, | | |
| | Polishing | Dimension error | | |
| Joining | Welding | Nut weld miss, | Clamp, Part | Pressure, Electricity, Temperature |
| | Riveting | Pin hold, Weld crack, | | |
| | Adhesive bonding | Detached | | |
| Moulding | Injection moulding | White mark, Shrinkage, Dimension error | Mould, Cylinder, Screw | Strain, Humidity, Temperature |
| | Blow moulding | | | |
| | Compression moulding | | | |
| | Rotational moulding | | | |

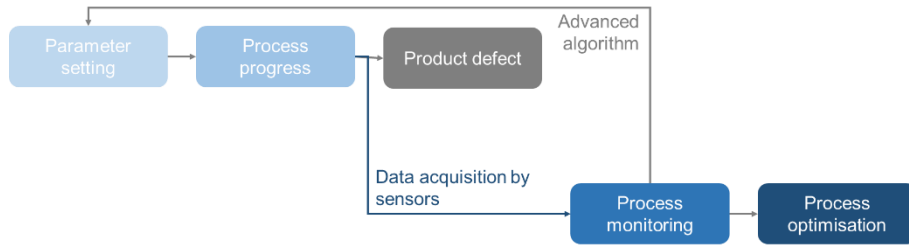


Figure 1.3. The sensor-enabled process monitoring for process optimisation

Sensor is a key enabler for process monitoring and process optimisation to deter the product defect or overall process shutdown. Data obtained by sensors and real-time feedback to process parameters using advanced algorithm enable the efficient and stable manufacturing process including forming, machining, joining, and moulding process as shown in **table 1.2** and **figure 1.3**.

Table 1.3. Requirements of sensor for smart manufacturing with respect to SMEs

| Essential | Affordable | Simple | Interoperable |
|---|---|---|---|
| –Perform essential functions –Not include unnecessary features | –Cost reasonable price to adopt –Provide low management cost | –Be used without additional equipment –Be utilised by untrained labour | –Be used in multiple applications –Be utilised in various process parameters |

Combining the given situations of sensor being a key technology for the utilisation of Industrie 4.0 technologies on the one hand and the high demand of cost-efficient strategies to implement Industrie 4.0 into SMEs on the other hand, reducing the costs for sensors represents a promising approach to lower the Industrie 4.0 entry barrier for SMEs. Therefore, a novel paradigm for low-cost smart sensor fabrication is presented as shown in **table 1.3**.

Black–Scholes model is a mathematical model for the dynamics of a financial market containing derivative investment instruments [21, 22]. The key idea behind the model is to hedge the option by buying and selling the underlying asset to eliminate risk as shown in **equations 1.1** and **1.2** where S and f are the price of the underlying asset and the price of the option as a function of S at time t , respectively. In addition, μ and σ denote the drift rate and standard deviation of S , respectively.

$$dS = \mu S dt + \sigma S dW \quad \text{Equation 1.1}$$

$$df = \left(\frac{\partial f}{\partial S} \mu S + \frac{\partial f}{\partial t} + \frac{1}{2} \frac{\partial^2 f}{\partial S^2} \sigma^2 S^2 \right) dt + \frac{\partial f}{\partial S} \sigma S dW \quad \text{Equation 1.2}$$

The appropriate cost of adopting sensor for smart manufacturing is a function of asset price, depreciation, and expected production yield of manufacturing equipment. This is the reason why large companies and SMEs have to spend a different amount of cost for adopting smart manufacturing equipment.

If S represents the asset price of manufacturing equipment with the depreciation rate μ and shutdown or failure rate σ followed by uncertain Wiener process W in **equation 1.1** and **1.2**, it is possible to estimate the appropriate adoption cost for smart manufacturing components f as a function of S and time t to eliminate the risk of process shutdown by process monitoring as shown in equation 1.3.

$$\Delta P = -\frac{\partial f}{\partial S} \Delta S + \Delta f = \left(\frac{\partial f}{\partial t} + \frac{1}{2} \frac{\partial^2 f}{\partial S^2} \sigma^2 S^2 \right) \Delta t \quad \text{Equation 1.3}$$

Using the properties that the expected output of the sum of manufacturing equipment and smart manufacturing components is same with the production yield of the price of total manufacturing equipment, **equations 1.4** and **1.5** are derived. By calculating **equation 1.5**, adoption cost for smart manufacturing component could be suggested based on operation situation for each company as shown in **equations 1.6–1.9**.

$$\Delta P = r \left(\frac{\partial f}{\partial S} S - f \right) \Delta t \quad \text{Equation 1.4}$$

$$rf = \frac{\partial f}{\partial t} + \frac{1}{2} \frac{\partial^2 f}{\partial S^2} \sigma^2 S^2 + r \frac{\partial f}{\partial S} S \quad \text{Equation 1.5}$$

$$f = N(d_1)S_t - N(d_2)PV(K) \quad \text{Equation 1.6}$$

$$d_1 = \frac{1}{\sigma\sqrt{T-t}} \left[\ln \left(\frac{S_t}{K} \right) + \left(r + \frac{\sigma^2}{2} \right) (T-t) \right] \quad \text{Equation 1.7}$$

$$d_2 = d_1 - \sigma\sqrt{T-t} \quad \text{Equation 1.8}$$

$$PV(K) = Ke^{-r(T-t)} \quad \text{Equation 1.9}$$

According to **equation 1.6**, it is necessary to adopt smart sensor with low-cost K , less amorisation $T - t$, multivariate measurable properties that do not require highly trained personnel for SMEs. It is a way to increase the operation cash flow by high production yield and overall equipment effectiveness (OEE) gain and decrease the investing cash flow by labour cost reduction, less amortization, and lowered capital expenditure (CAPEX) [23, 24].

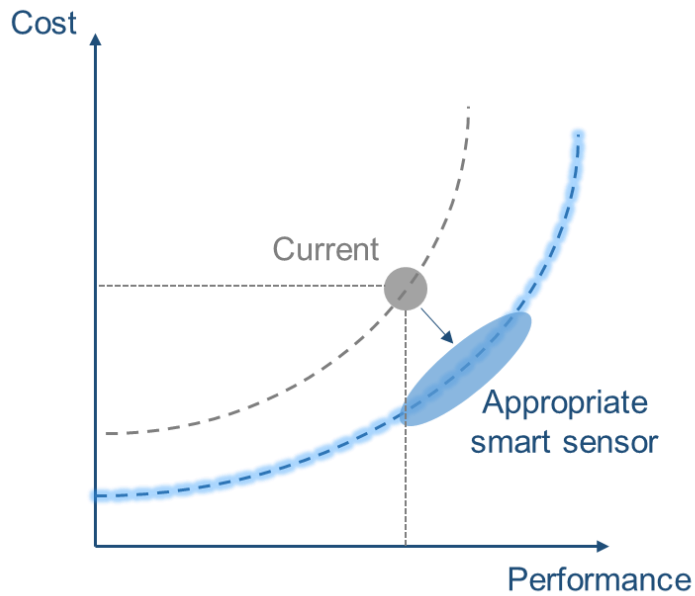


Figure 1.4. Toward appropriate smart sensor

1.3. Research objective

This dissertation has aimed to develop the low-cost smart sensor for manufacturing process monitoring to lower entry barrier of smart manufacturing adoption by decreasing required capital and labour. According to Solow–Swan model which is an economic model of long-run economic growth set within the framework of neoclassical economics, technological progress could compensate capital accumulation, labour or population growth for same amount of economic output as shown in **equation 1.10** where $K(t)$ and $L(t)$ represent capital and labour, respectively while $A(t)$ denotes the technological knowledge at time t [25, 26].

$$Y(t) = K(t)^\alpha (A(t)L(t))^{1-\alpha} \quad \text{Equation 1.10}$$

Since the end-user could calculate mechanical strain or vibration just by measuring the resistance, piezoresistive type sensor is one of the most widely used sensor for manufacturing process monitoring including forming and milling process [27, 28]. The piezoresistive effect is a change in the electrical resistivity of a metal when mechanical strain is applied as shown in **equation 1.11** where $\partial\rho$, ρ , and ε denote the change in resistivity, original resistivity, and strain, respectively [29].

$$\rho_\sigma = \frac{\partial\rho}{\rho} / \varepsilon \quad \text{Equation 1.11}$$

Table 1.4. Performance indicators for piezoresistive type strain and vibration sensor

| | |
|----------------|---|
| Sensitivity | – How much resistance change with strain |
| Stretchability | – How much strain range can be measured |
| Durability | – How long the sensor is available |
| Printability | – How easy to fabricate desired sensor |
| Attachability | – How easy to install sensor in equipment |

According to **figure 1.5**, it has been confirmed that existing studies have limitations in both high sensitivity and measurable range [30–41]. Furthermore, the study was not only insufficient but also limited in terms of high performance for multivariate measurable sensor as shown in **table 1.5** [36, 38, 39, 42, 43].

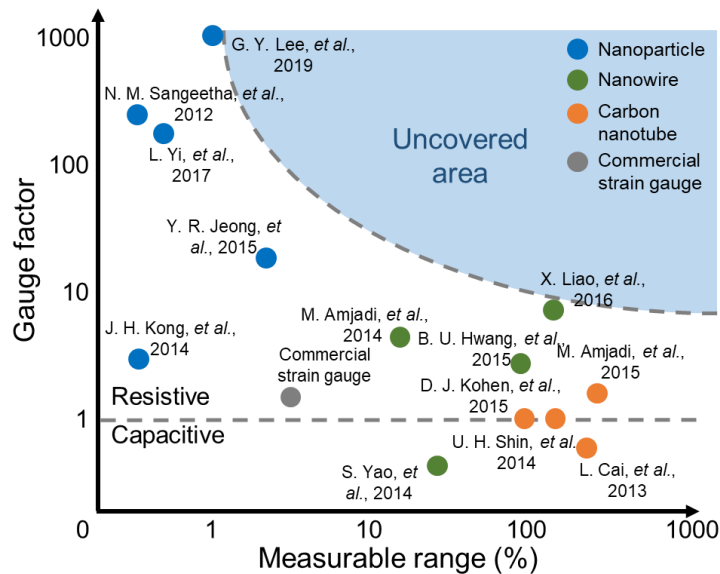


Figure 1.5. Previous researches of sensor according to measurable range and gauge factor

Table 1.5. Previous researches of multivariate measurable sensor

| Previous studies | Gauge factor | Measurable range (%) | Sensing type |
|------------------------------------|--------------|----------------------|---|
| C. S. Boland, <i>et al.</i> , 2014 | 3.5 | 80 | Strain + Vibration |
| X. Liao, <i>et al.</i> , 2016 | 9.65 | 150 | Strain + Temperature |
| U. H. Shin, <i>et al.</i> , 2014 | 1 | 150 | Strain + Pressure |
| S. Yao and Y. Zhu, 2014 | 0.7 | 50 | Strain + Pressure |
| W. Fan, <i>et al.</i> , 2016 | – | 100 | Strain + Temperature, UV, Electrocardiogram |

Representative performance indicators for the piezoresistive type sensor is shown in **table 1.4**. Recent advances in nanomaterial technology open the new possibility to fabricate high performance piezoresistive type sensor [44–46]. Accumulated technological progress for piezoresistive type sensor has decreased the required labour and capital for same amount of economic output. Representatively, there have been several efforts to fabricate highly sensitive sensors with high sensitivity and large stretchability [47–49]. According to previous studies, metal nanoparticle (NP) are widely used nanomaterial for highly sensitive strain sensors [50–53]. The high sensitivity for NPs based strain sensor is not due to

materials intrinsic properties like piezoresistive effect but to the current transport mechanism itself which is based on current tunnelling through nanogaps between NPs [54–58].

However, major disadvantage of NPs based strain sensor is low stretchability also due to sensing mechanism itself. Electrical disconnection by mechanical separation between NPs is major reason for narrow measurable range [59–62]. To overcome the intrinsic limitation of NPs based strain sensor, there have been several efforts to utilise nanocomposite composed of NPs with carbon nanotubes (CNTs) [63, 64]. CNT, which has high mechanical and electrical properties, is representative nanomaterial for wide measuring strain sensor [65, 66].

In this dissertation, aerodynamically focused nanomaterial (AFN) printing system which is a direct printing technique for inorganic nanomaterial onto flexible and stretchable substrate in low vacuum and room temperature condition is presented [67]. As it is a direct printing process, it is capable of printing desired pattern onto desired position in regardless of the geometry of pattern. Furthermore, since it does not require any solvent or heat treatment, highly sensitive property using electrical connection between nanomaterials is available.

This dissertation covers the fabrication and evaluation of high performance sensor composed of NPs and CNTs capable of strain and vibration measurement fabricated by AFN printing process, analysis of strain and vibration sensing mechanism of developed

sensor, using statistical regression analysis and Monte Carlo based simulation method respectively, and applications to manufacturing process monitoring including forming process, milling process, and wireless communication monitoring.

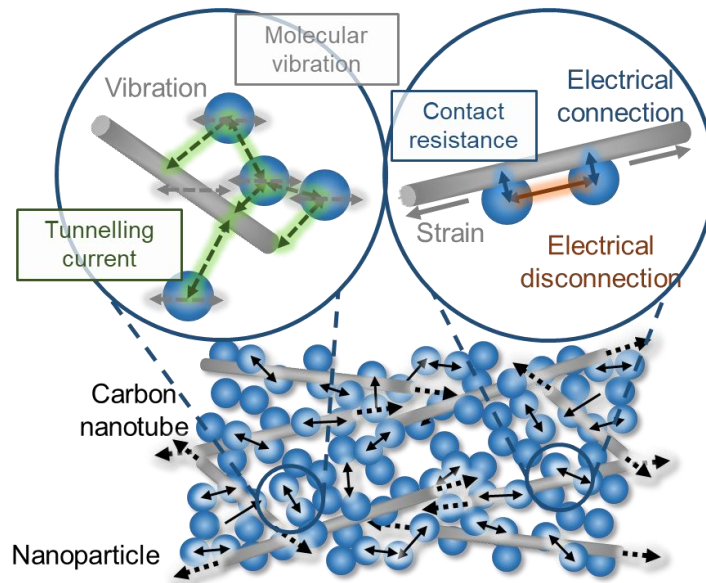


Figure 1.6. Technological approach for this dissertation

Chapter 2. Background

2.1. Aerodynamically focused nanomaterial printing

The aerosol based solvent-free and low temperature process is beneficial to fabricate not only the pattern with high degree-of-freedom design but also the highly sensitive conductive pattern. It does not occur the sintering between nanomaterials and only detect the electrical resistance changes of nanomaterial as shown in **figure 2.1** [68].

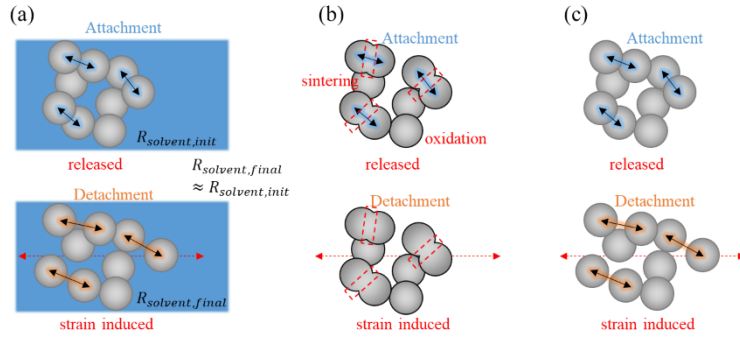


Figure 2.1. The schematic diagram of sensing mechanism for piezoresistive type sensor fabricated by (a) solvent required, (b) high temperature, and (c) AFN printing process

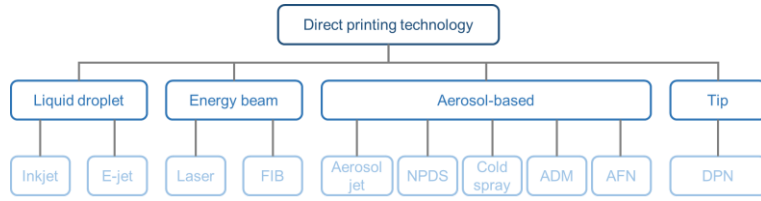


Figure 2.2. Categorisation of direct printing technology for sensor fabrication by printing source

Figure 2.2. shows the categorisation of direct printing technology for sensor fabrication by printing source [69]. The printing source was divided by liquid droplet, energy beam, aerosol-based, and tip based printing. In general, energy beam based direct printing requires the high temperature which causes the sintering or annealing between nanomaterials. Furthermore, tip based direct printing technique requires the huge amount of time for the sensor fabrication. Hence, this dissertation has focused on liquid droplet based and aerosol-based direct printing to compare the printing technology.

Table 2.1 shows the evaluation of direct printing technology which was discussed in figure 2.2. The printing technology was evaluated by several indicators including printing materials, kinetic energy source, heat treatment, particle or droplet speed, particle or droplet diameter, feature scale, and thickness of pattern. NPDS (Nanoparticle deposition system), ADM (aerosol deposition method), CS (Cold spray), and AFN (Aerodynamically focused nanomaterial printing) used solid nanomaterial rather than liquid ink without heat treatment which could generate less agglomerated pattern for highly sensitive sensor fabrication.

Table 2.1. Evaluation of direct printing technology for sensor fabrication

| Indicator | Ink-jet | E-jet | Aero sol-jet | NPDS | ADM | CS | AFN |
|--------------------|-------------|-------------|--------------|---------------------|---------------------|---------------------|-----------|
| Printing materials | liquid ink | liquid ink | liquid ink | solid | solid | solid | solid |
| Energy source | liquid flow | liquid flow | gas | gas | gas | gas | gas |
| Heat treatment | O | O | O | X | X | X | X |
| Speed (m/s) | < 50 | < 50 | ~100 | 300–1,000 | 100–500 | 400–1,200 | 300–1,000 |
| Diameter (μm) | 10–150 | 0.5–100 | 1–5 | 0.1–1 | 0.1–1 | 10–120 | 0.1–1 |
| Feature scale (μm) | 10–100 | <10 | ~10 | 500–10 ⁴ | 500–10 ⁴ | 500–10 ⁴ | 10–50 |
| Thickness (μm) | <1 | 0.1–1 | <1 | 1–500 | 1–500 | <1,000 | <10 |

Table 2.2 shows the capabilities of low temperature nanomaterial printing process including ADM, CS, NPDS, and AFN printing in more detail to compare resolution, temperature, vacuum state, and feed rate. In comparison to ADM, CS, and NPDS, AFN printing is capable of microscale pattern fabrication with pattern width of several tens of micrometers which is suitable for fabrication of piezoresistive sensor for actual usage [70–72].

Table 2.2. Review of low temperature nanomaterial printing process

| | ADM | CS | NPDS | AFN |
|--------------------|----------|------------|------------|-----------|
| Resolution (mm) | 0.5 – 10 | 0.5 – 10 | 0.5 – 1000 | 0.03 – 10 |
| Temperature (K) | 300 | 300 – 1000 | 300 | 300 |
| Vacuum (atm) | 1 | 1 | 0.8 | 0.8 |
| Feed rate (mm/min) | 1 | 2 | 0.05 | 0.02 |

Table 2.3 shows the description of AFN process according to various properties. Since it is a solvent-free dry process in room temperature and low vacuum condition, it is available to fabricate pattern with separated nanomaterial. Furthermore, it uses metal and ceramic nanomaterial as a printing materials which can achieve high contact resistance changes in suitable scale.

Table 2.3. Description of AFN process and effect to fabricated sensor

| Property | AFN description | Effect |
|--------------------|---------------------------------|----------------------------------|
| Printing mechanism | Solvent-free dry process | Limited agglomeration |
| Process condition | Room temperature and low vacuum | No sintering and annealing |
| Printing materials | Metal and ceramic nanomaterial | High contact resistance |
| Printing scale | Several tens of micrometers | Suitable for pattern fabrication |

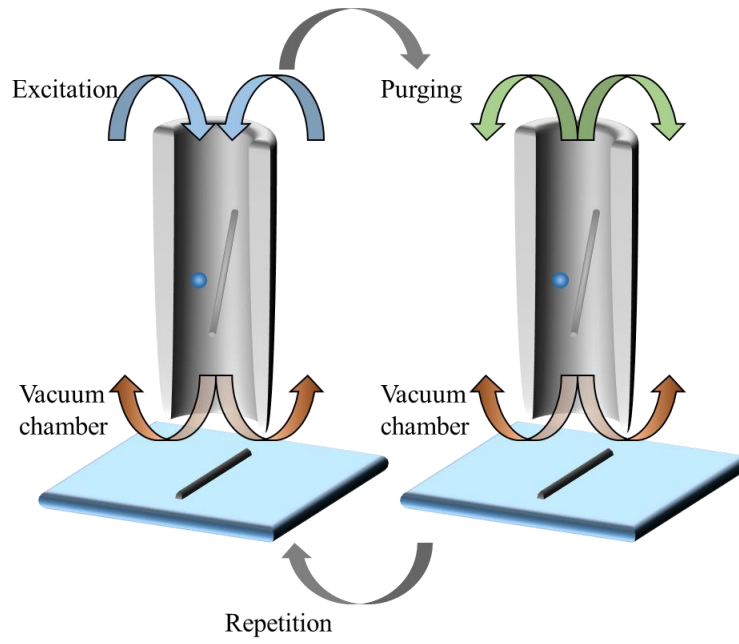


Figure 2.3. The principle of AFN printing process by successive repetition of excitation and purging

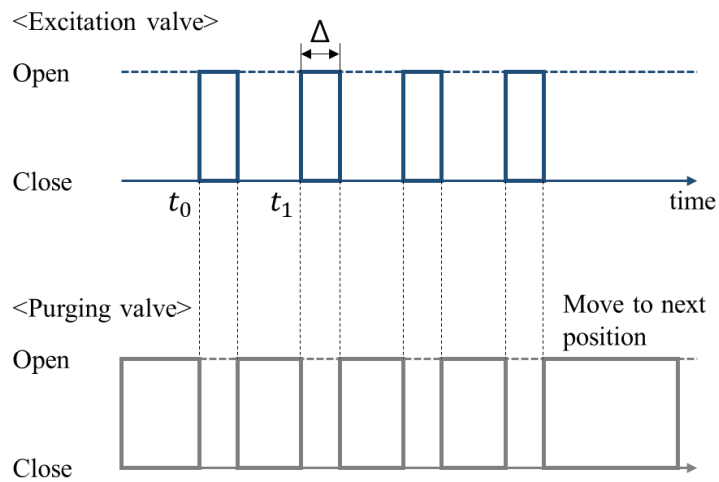


Figure 2.4. Time sequence of excitation and purging of aerosol control in AFN printing process

The time sequence control of excitation and purging of aerosol composed of nanomaterials plays a major role in fabrication of small features. AFN printing process is capable of printing the pattern of one tenth in comparison to the inner diameter of the nozzle.

It was demonstrated that the drag force, Saffman's lift force, and centrifugal force predominantly influence on the dynamic behaviour of aerodynamic focusing for AFN printing process. For further analyses, it is necessary to divide the AFN printing process by upstream of the nozzle and downstream of the nozzle which governed by drag force and Saffman's lift force, and drag force and centrifugal force, respectively as shown in **equations 2.1, 2.2, and 2.3.**

$$F_D = \frac{m_m}{\tau} (u_g - u_m) \quad \text{Equation 2.1}$$

$$F_S = 1.615 \sqrt{\rho_g \mu} d_m^2 (u_g - u_m) \sqrt{-\frac{du_g}{dr}} \quad \text{Equation 2.2}$$

$$F_R = \frac{m_m u_m^2}{R} \quad \text{Equation 2.3}$$

The u_g and u_m represent the velocity of gas flow and materials, respectively and m_m and d_m represent the mass and diameter of materials, respectively. Stokes' drag law with small Reynolds number was used to determine the drag force F_D on the material. In the upstream region, Saffman's lift force F_S acts as an inertial effect pushing the material to where the gas velocity is higher, usually in the direction of the flow axis. Thus, the material' radial position shifts to the axis separated from the streamline as shown in **figure 2.5.**

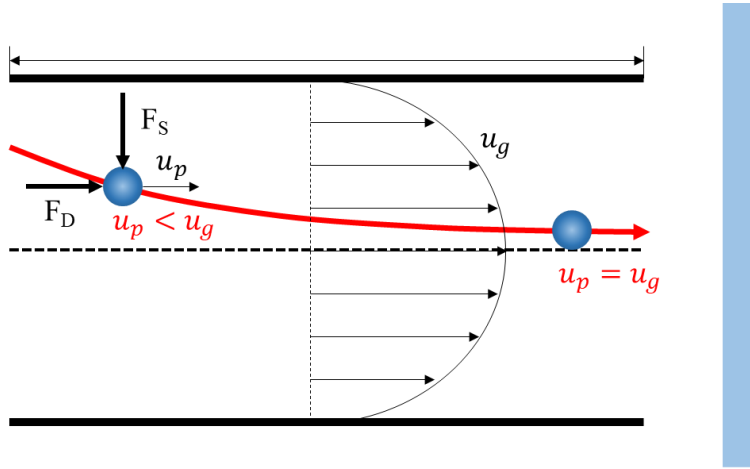


Figure 2.5. The free body diagram of drag and Saffman's lift forces in the upstream of the nozzle

By using analytical expression of F_S and F_D from **equations 2.1** and **2.2**, the ratio of two forces was derived as shown in **equation 2.4**. Then, by combining geometrical expression of two forces as shown in **equation 2.5**, the source pressure was optimised as shown in **equation 2.6**.

$$\frac{F_S}{F_D} = \frac{1.615 \frac{\sqrt{\mu} d_m^2}{\sqrt{RT}} (u_g - u_m) \sqrt{-\frac{du_g}{dr}} \sqrt{P_s}}{\frac{3\pi\mu d_p}{c_c} (u_g - u_m)} = 0.127 \frac{k_B \sqrt{T}}{\sqrt{\mu} d_m^2 \sqrt{R}} \sqrt{-\frac{du_g}{dr}} \sqrt{\frac{1}{P_s}} \text{Equation 2.4}$$

$$\frac{F_S}{F_D} = \frac{D}{L} \text{Equation 2.5}$$

$$P_s = -1.09 \times 10^{-5} \left(\frac{du_g}{dr} \right) \left(\frac{L}{D} \right)^2 \text{Equation 2.6}$$

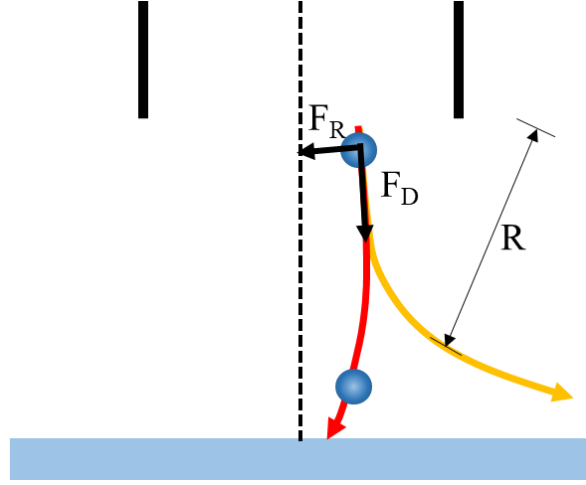


Figure 2.6. The free body diagram of drag and centrifugal forces in the downstream of the nozzle

In the downstream region, the curvilinear motion of the streamline, due to the substrate, creates a centrifugal force F_R as an inertial effect as shown in **figure 2.6**. By using the acceleration formula and geometrical properties of drag force F_D and centrifugal force F_R , **equation 2.7** was derived to optimise the excitation time of AFN printing process.

$$\frac{F_R}{F_D} = \frac{\frac{m_m u_m^2}{R}}{\frac{m_p}{\tau}(u_g - u_m)} = \tau \frac{u_m^2}{R(u_g - u_m)} \geq \frac{4(\sqrt{2}-1)}{\pi} \quad \text{Equation 2.7}$$

The materials with a certain velocity cause a plastic deformation or an erosion of the substrate, and they either adhere to the substrate or bounce back. Adhesion does not occur until a critical material velocity has been exceeded which depends on the material and the temperature at the time of impact. For more simplified analysis, it is

advantageous to consider the gas flow to be ideal, isentropic, and one-dimensional. In general, the changes of state are merely functions of the local Mach number and the isentropic coefficient where Mach number is defined in **equation 2.8**.

$$\text{Ma} = \frac{v}{\sqrt{\kappa RT}} \quad \text{Equation 2.8}$$

The gravitational force and materials-materials interaction can be neglected due to the short resident time of the materials in the flow and low materials concentration in the gas flow. A drag coefficient constant of the material acceleration is proportional to the gas density and to the square of the relative velocity, and inversely proportional to the material density and materials diameter. The relative velocity between gas and material can be greater than the local sound velocity, thus a shock will form in front of the material. It is necessary to introduce a drag coefficient, which is also a function of the Mach number, because the shock in front of the material has a considerable influence on the material acceleration. In general, the drag coefficient is therefore a function of the Reynolds number and the materials' Mach number as shown in **equation 2.9** where each number is defined as shown in **equations 2.10 and 2.11** [73].

$$C_D = f(Ma_m, Re_m) \quad \text{Equation 2.9}$$

$$Re_m = \frac{\rho |v_g - v_m| d_m}{\mu_g} \quad \text{Equation 2.10}$$

$$Ma_m = \frac{|v_g - v_m|}{\sqrt{\kappa R T_g}} \quad \text{Equation 2.11}$$

The heat transfer between gas and material as a result of the high Mach number flow which is more than 0.24 is obtained by introducing a modified Nusselt number as shown in **equation 2.12**.

$$Nu = 2 + 0.44 Re_m^{0.5} Pr^{0.33} \exp(0.1 + 0.872 Ma_m) \quad \text{Equation 2.12}$$

Because of the high heat conduction coefficient of a NP and CNT, it is assumed that the nanomaterial has a uniform temperature inside at any time when the Biot number is less than 0.1 as shown in **equation 2.13** where h is the gas heat transfer coefficient and k_p is the heat conductivity of the spray material, respectively.

$$Bi = \frac{h d_m}{k_p} < 0.1 \quad \text{Equation 2.13}$$

In this dissertation, compressed air with heat transfer coefficient of $\sim 10^1$ W/m²K and nanomaterial with heat conductivity of $\sim 10^{-2}$ W/mK and diameter of $\sim 10^{-7}$ m was used for sensor fabrication which satisfy above condition.

2.2. Printing system envelope

AFN printing system consists of a nanomaterial feeder, vacuum chamber, and nozzle to create aerosolised nanomaterial beam as shown in **figure 2.7**. Following shock-induced aerosol generation via control of excitation and purging time, aerosolised nanomaterials blow up to the aerodynamic filter which occurs laminar aerosol flow. The transported aerosolised nanomaterials are aerodynamically focused when they spurt out from the nozzle and directly deposited onto a substrate.

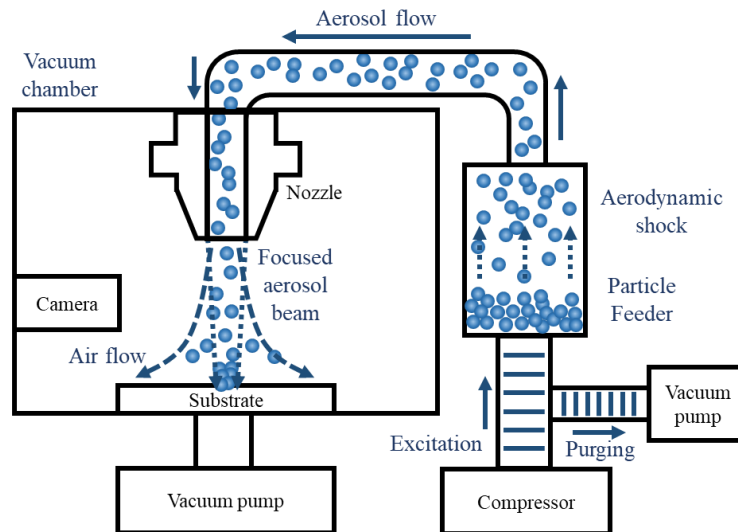


Figure 2.7. Schematic diagram of AFN printing system

As nanomaterial are deposited by high speed impact with a substrate, AFN printing system is suitable for direct printing of various inorganic materials without chemical bonding or heat treatment. Direct printing is a particularly efficient technique for the fabrication of microscale patterns such as strain sensors. Microscale porous pattern composed of nanomaterial could be printed as desired regardless of geometry. Furthermore, patterns could be repaired or reconfigured when necessary, which overcomes the limitations of conventional processes such as laser ablation or photolithography.

AFN printing system was designed and integrated as shown in **figure 2.8**. To develop mass production system of high performance sensor, multi-nozzle system was configured with high stroke stage and large-scale vacuum chamber. All the system components were controlled in real-time using embedded programmable logic controllers (PLCs) in system.

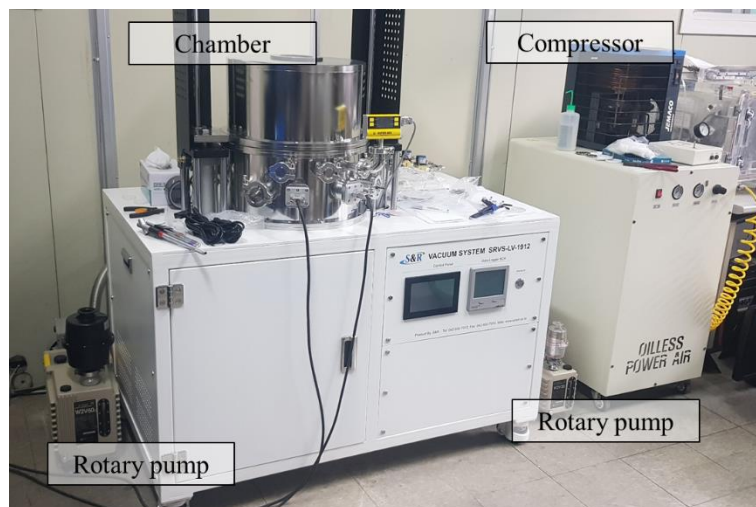


Figure 2.8. The photograph of AFN printing system

Table 2.4. Process parameters of AFN printing process

| Parameters | Values |
|--|--------|
| Source pressure (Pa) | 1000 |
| Chamber pressure (Pa) | 400 |
| Excitation time (msec) | 10 |
| Purging time (msec) | 90 |
| Feed rate (mms^{-1}) | 0.2 |
| Distance between the substrate and nozzle (mm) | 1 |
| Carrier gas | Air |

To print continuous line pattern, feed rate of printing and density of aerosolised nanocomposite must be remained at specific level. As density of aerosol is controlled by time–scaling of excitation and purging of compressed air, optimising process parameters is important to fabricate patterns as desired.

Table 2.4 shows the process parameters used in AFN printing process for this dissertation. Nanomaterials were carried by air driven by pressure difference between source and chamber controlled by excitation time and purging time. Source pressure and chamber pressure were remained at 1000 Pa and 400 Pa, respectively. Excitation time is the time to blow air into the feeder and purging time refers to the time taken for the air to escape from the feeder. Sequential repetition of excitation for 10 ms and purging for 90 ms remained for process. A metal nozzle with inner diameter of 150 μm (Taeha Co., Republic of Korea) with a feed rate of 0.2 mms^{-1} was used for printing at the 1 mm above from the substrate.

The incident opening of the excitation valve dispersed the nanomaterials into induced gas stream and created an instant pressure increase inside the chamber. The increase source pressure resulted in a decrease of materials' time-scales which resulted in their rapid adjustment to the induced gas flow.

After the termination of the excitation, purging was initiated by decreasing the source pressure. The next excitation and purging cycle was initiated again after the source pressure was reset to low pressure. **Figure 2.9** shows the measured pressure during AFN printing process which denotes the fluctuation of pressure of feeder according to excitation and purging of aerosol while the pressure of chamber was remained.

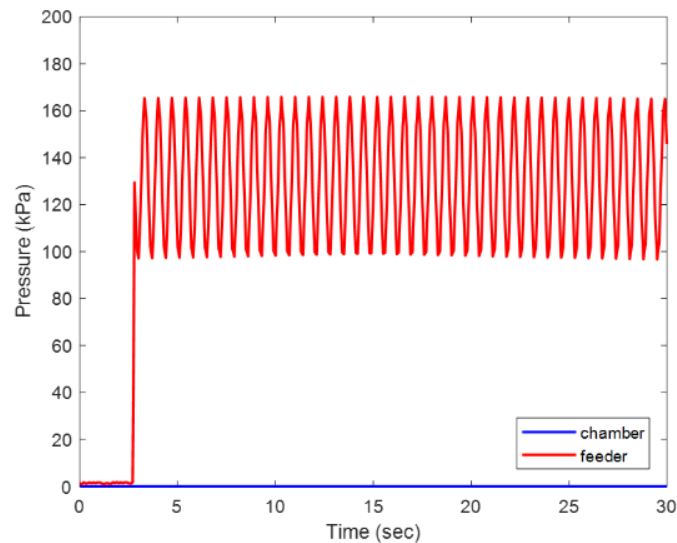


Figure 2.9. The measurement results of pressure of chamber and feeder during AFN printing process

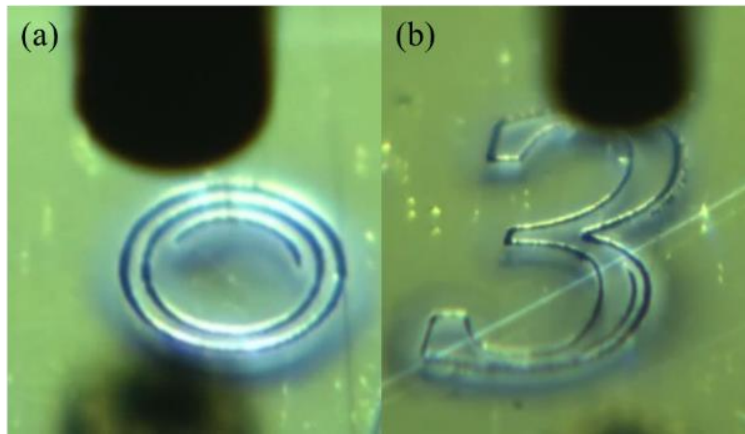


Figure 2.10. The optical microscopic image of AFN printed pattern with (a) concentric shape, and (b) number “3” shapes

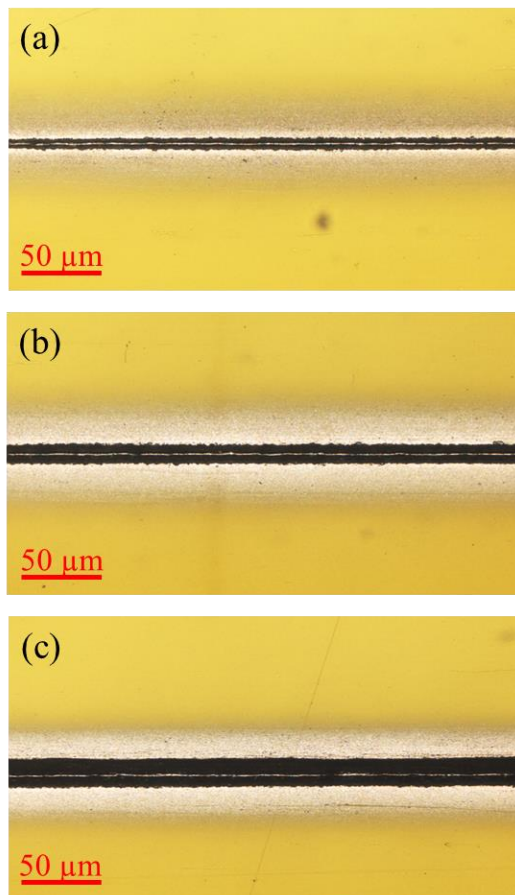


Figure 2.11. The optical microscopic image of AFN printed line pattern with pattern width of (a) 16.31, (b) 27.8, and (c) 49.29 μm .

Figure 2.10 shows the AFN printed example with concentric and number “3” shapes. It was demonstrated that pattern printing with high degree-of-freedom of design was achieved by AFN printing process [74].

Figure 2.11 shows AFN printed line pattern example with various pattern width according to different process times. Using charge-coupled device (CCD) cameras (EO-0813C, Edmond Optics, USA), the pattern width was measured during AFN printing process as shown.

It was demonstrated that packing ratio of the pattern γ which defined as the volume ratio of printed nanocomposite to the surface boundary of the pattern could be controlled by the process parameter of AFN printing system. The process parameter used for this dissertation was the scan velocity which is similar to the feed rate in conventional machining process defined as the printed pattern length by process time. By measuring the difference between mass of the substrate before and after AFN printing by a precise microbalance (Sartorius AG, Germany) and surface profile by laser confocal microscope (OLS 4100, Olympus, Japan), packing ratio was calculated as shown in **equation 2.14**.

$$\gamma = \frac{m_{pattern}}{\rho_{pattern}V} \quad \text{Equation 2.14}$$

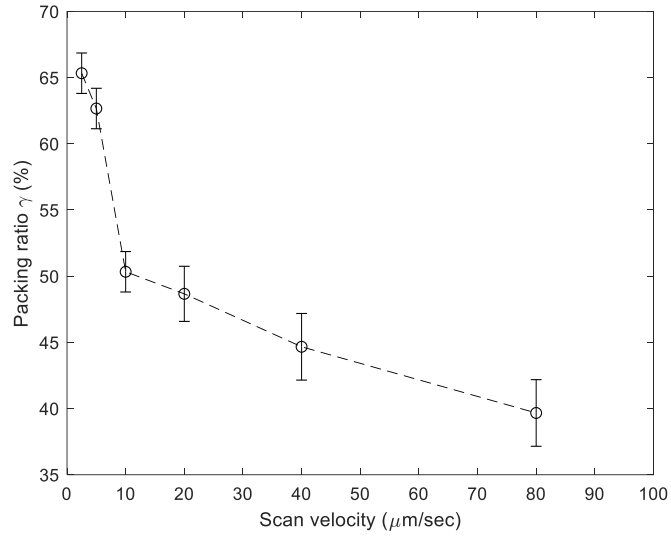


Figure 2.12. The measurement results of packing ratio of AFN printed pattern with respect to the scan velocity

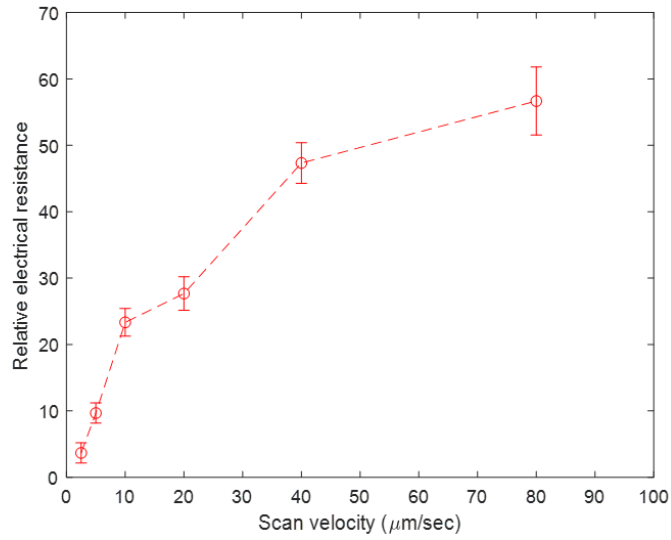


Figure 2.13. The measurement results of relative electrical resistance of AFN printed pattern with respect to the scan velocity

It was demonstrated that scan velocity dominantly influences on not only the geometry of the printed pattern but also the packing ratio. By varying scan velocity from 2 to 80 $\mu\text{m/s}$, the packing ratio decreased from 65% to 40% as shown in **figure 2.12**.

Furthermore, the decrease of packing ratio occurred the increase of relative electrical resistance as shown in **figure 2.13**. Since the high packing ratio decreased the distance among nanomaterials, electrical resistance increased as the number of electrical floating increased in the printed pattern. Hence, the scan velocity was maintained as 80 $\mu\text{m/s}$ during AFN printing process for highly sensitive sensor fabrication.

2.3. Highly sensitive sensor printing

Figure 2.14 shows the fabrication process of highly sensitive sensor using silver NP (AgNP) (<100 nm particle size, 576832, Sigma–Aldrich, USA) on a glass fibre reinforced plastic (GFRP) film with polyimide (PI) film as an adherent backing layer. After AgNP printing, ultraviolet (UV) curable resin was covered for stabilising the pattern.

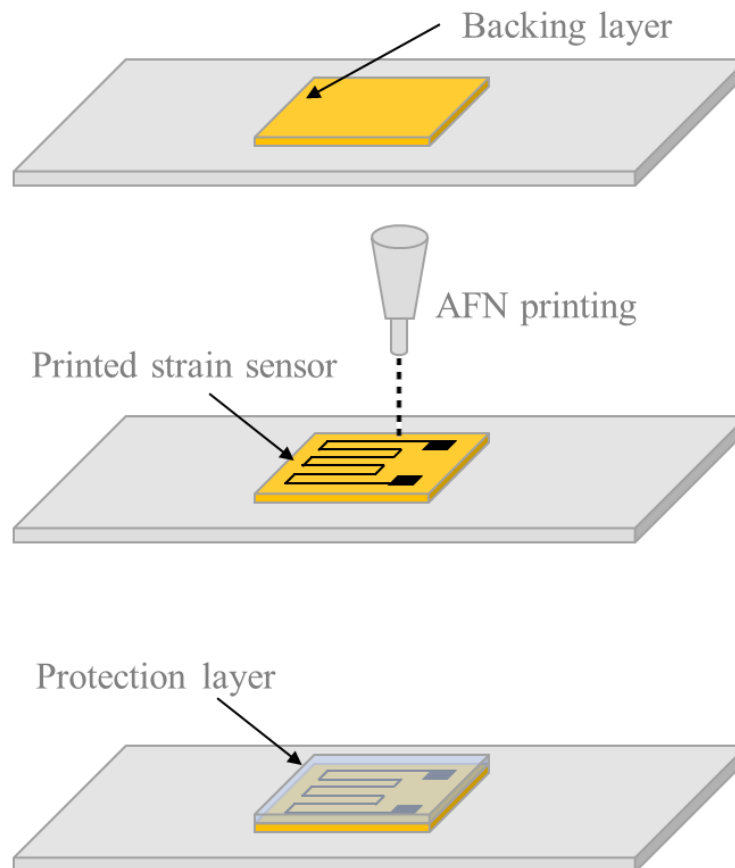


Figure 2.14. The schematic diagram of fabrication process of highly sensitive sensor

Since the AFN printing system produces highly reproducible complex patterns with well-defined 10 μm resolution, sensor was fabricated with similar design to commercial strain gauge. The printed AgNPs were mechanically attached well each other which made conductive line patterns capable to serve as strain sensor.

Figure 2.15 shows the photograph of highly sensitive sensor with the length of 7 mm. After soldering process using silver paste (conductive paste, 735825, Sigma–Aldrich, USA) for electrical connection with external data acquisition equipment, the electrical resistance of printed sensor was measured.

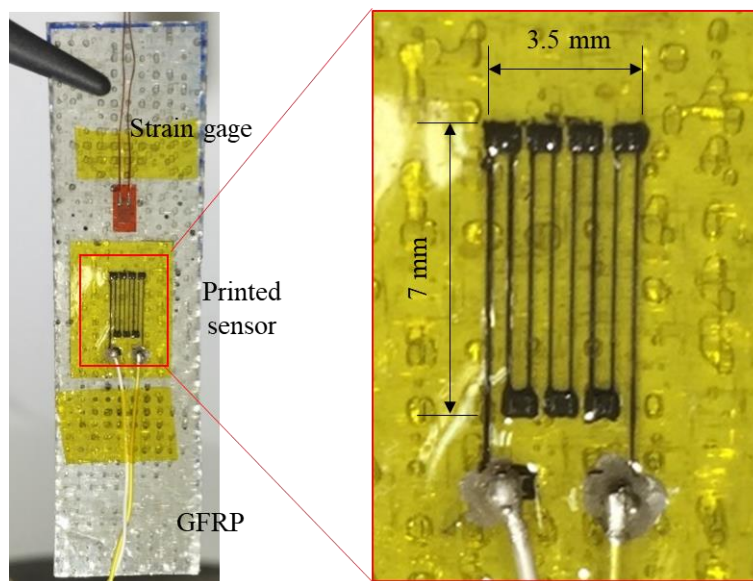


Figure 2.15. The photograph of fabricated highly sensitive sensor.

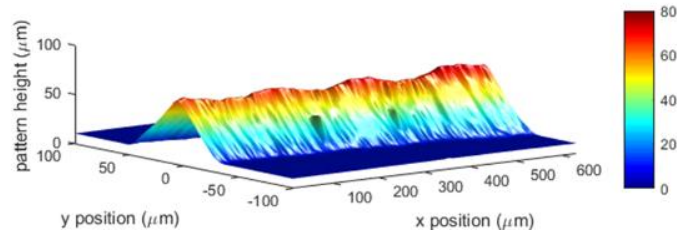


Figure 2.16. The confocal microscopic image of highly sensitive sensor

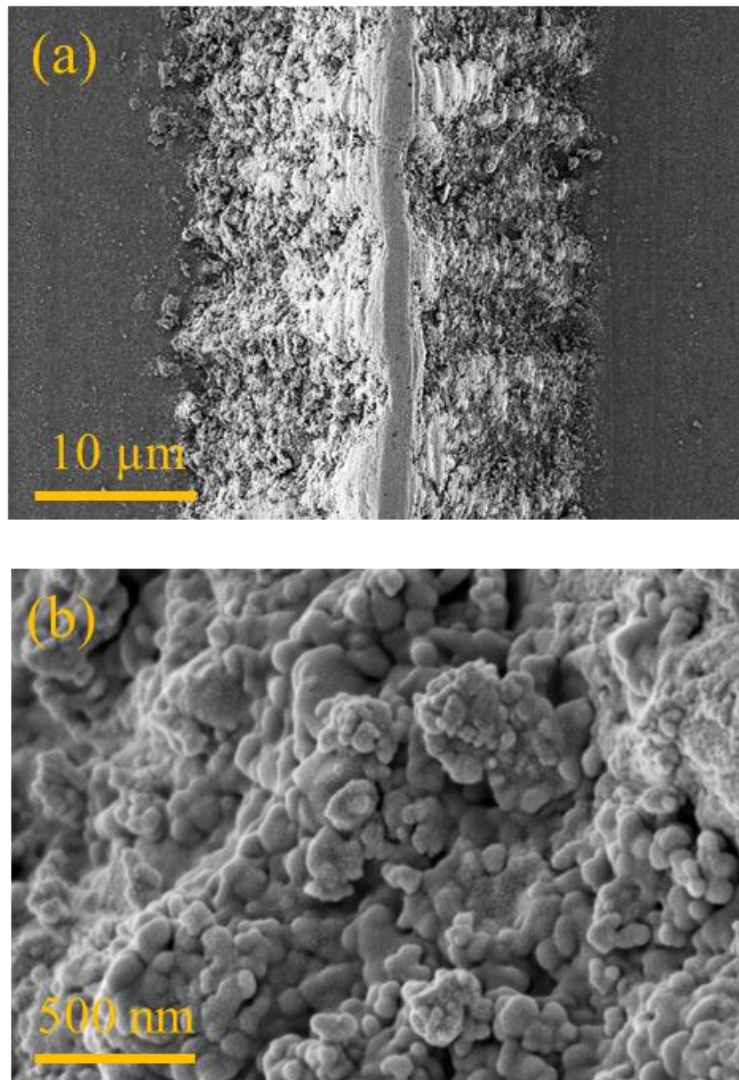


Figure 2.17. (a) SEM image of highly sensitive sensor and (b) its magnified view

Figure 2.16 shows the confocal microscopic image of fabricated sensor. The pattern width was varied from 10 to 100 μm according to the measurement conducted at a magnification of 432X with a field of view of 640 μm with resolutions of 0.625 μm in the x-y coordinates and 10 nm in the z-coordinate.

Figure 2.17 shows the SEM image of nanostructures of the pattern and its magnified view, respectively, as revealed by field-emission scanning electron microscopy (FE-SEM) (AURIGA60, Carl Zeiss).

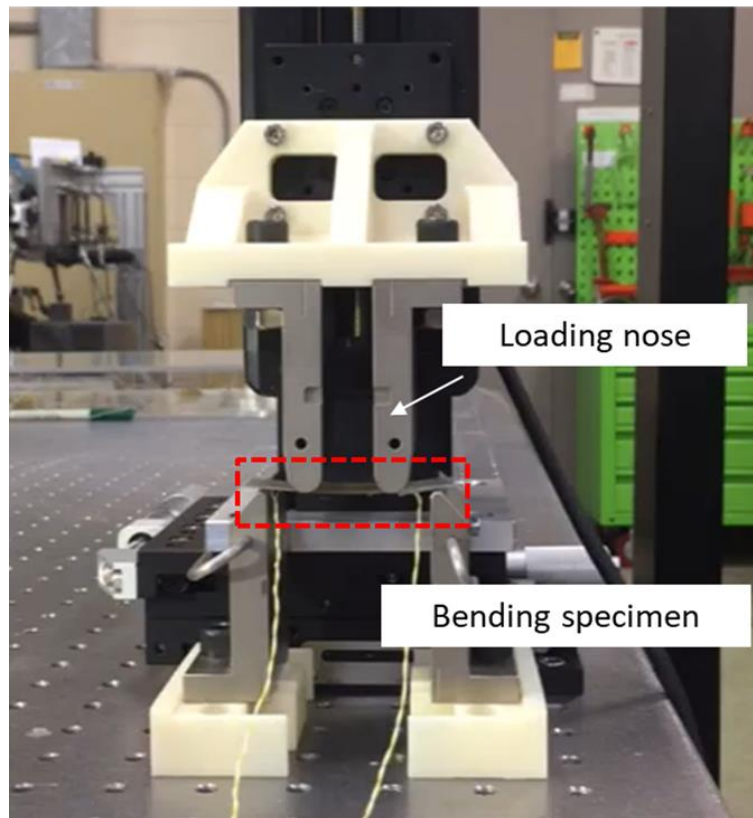


Figure 2.18. The photograph of experimental setup for sensing performance evaluation based on standardised 4-points bending method

Figure 2.18 shows the photograph of experimental setup for sensing performance evaluation based on standardised 4-points bending method. Both ends of the sensor were fixed to the mechanical jig and the centre of the sensor was translated by a motorised stage (SGSP 20–85, Simga Koki, Japan), and the images were captured by a CCD camera (UI–2240SE, IDS Imaging Development Systems). The printed sensor and commercial strain gauge were both subjected to 4-point bending test to compare the performance of each sensor. The experiments were conducted for over 5000 operation cycles to verify the mechanical reliability.

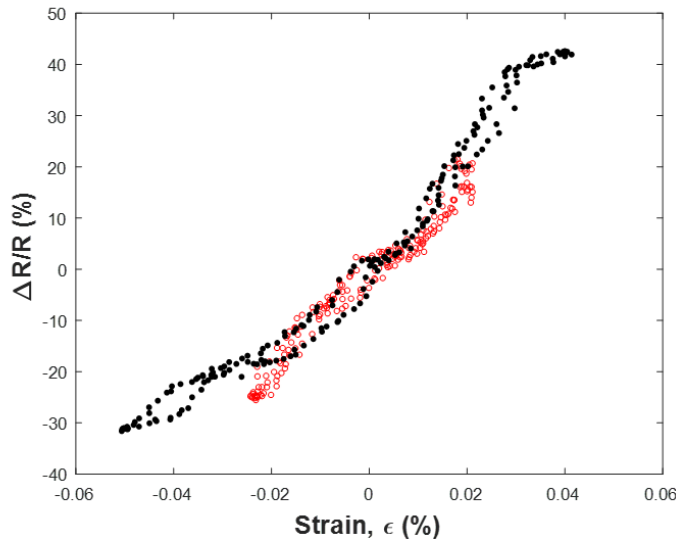


Figure 2.19. The evaluation results of sensing performance of highly sensitive sensor

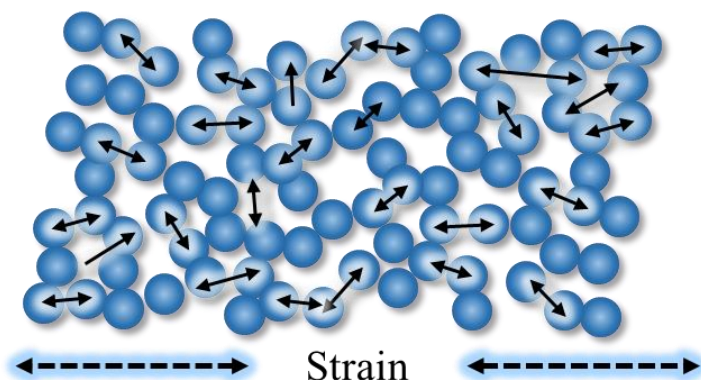


Figure 2.20. The schematic diagram of sensing mechanism for highly sensitive sensor

Figure 2.19 shows the plots of the resistive response by the applied strain. The response of a sensor exhibited that the sensitivity was tunable from 18.60 to 290.62 by varying the process parameter of AFN printing. In an instant, sensitivity of 1,056 was exhibited at an applied strain with narrow strain range.

Figure 2.20 shows the schematic diagram of sensing mechanism for NPs based strain sensor to explain the highly sensitive properties of fabricated sensor. A simplified electron-tunneling model has often been used to explore the resistive responses of the NP strain sensor, represents that the relative resistance change is due to mechanical detachment between NPs. Mechanical separation between NPs enables drastic change of relative resistance but also electrical disconnection above specific level of applied strain.

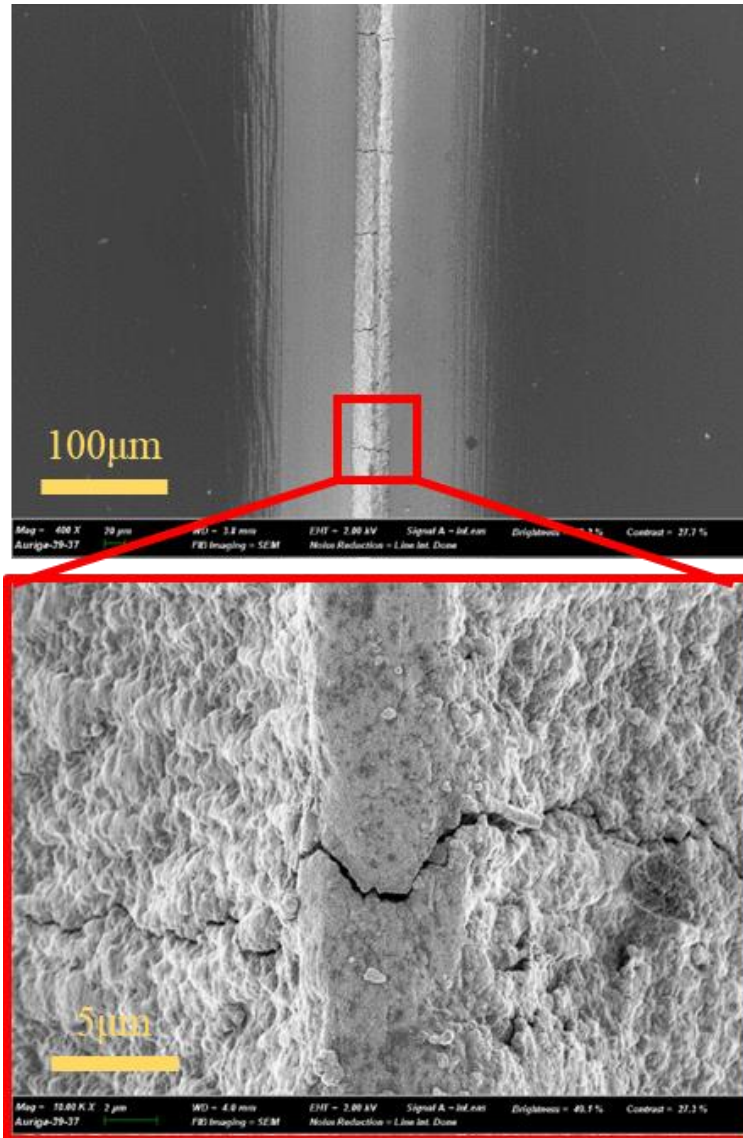


Figure 2.21. SEM image of mechanical crack in highly sensitive sensor

Figure 2.21 shows the SEM image of mechanical cracks developed after 4% strain was applied. Since mechanical crack mechanically detached NPs each other, it was difficult to apply NPs based strain sensor with wide measurable range applications.

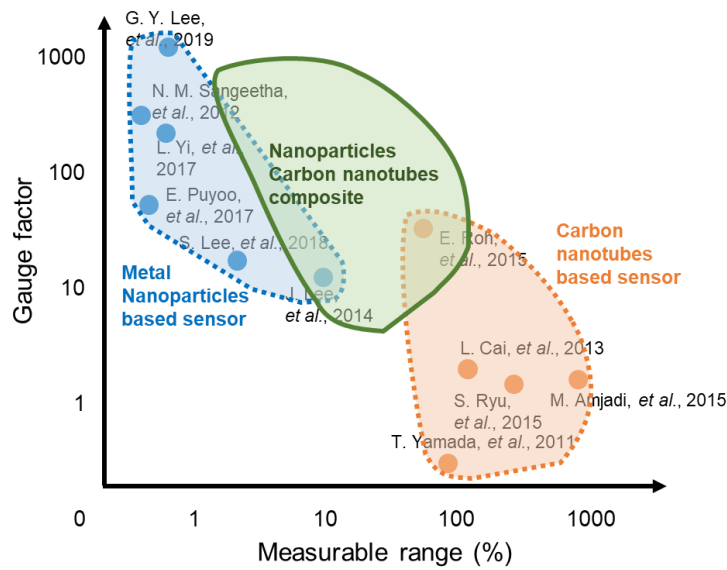


Figure 2.22. State-of-the-art and research objective according to GF and maximum strain limit

Figure 2.22 shows the sensitivity or GF and stretchability for printed highly sensitive sensor. Fabricated sensor composed of AgNPs shows high sensitivity but narrow measurable range due to their mechanical crack.

In general, CNTs based strain sensors show low sensitivity but wide measurable range. CNT, which is electrically conductive and also highly stretchable, enables wide measurable range for strain sensor. By printing nanocomposite sensor composed of AgNPs and CNTs at once, this dissertation has aimed to achieve high performance in both sensitivity and measurable range.

Chapter 3. Sensor fabrication and evaluation

3.1. Highly sensitive and wide measuring sensor printing

A compatibility of nanomaterial and substrate plays a major role in printing quality of AFN printed pattern. **Table 3.1** shows the combination table of nanomaterial and substrate in perspective of printing quality [75]. Results were judged by various images including optical images and surface profile results measured by confocal microscope.

Table 3.1. Material–substrate compatibility of AFN printing process (Results added from [75])

| | C F R P | G F R P | PI | P D M S | P C B | P E | P P | P M M A | P E T | Al S l | C u | Al | Ni | Ni Ti | Si | Si O ₂ |
|--------------------------------|------------------|------------------|----|------------------|-------------|--------|--------|------------------|-------------|--------------|--------|----|----|----------|----|----------------------|
| TiO ₂ | X | | | | | ∠ | ∠ | □ | □ | □ | □ | □ | □ | | □ | □ |
| Al ₂ O ₃ | | | | | | | | | | □ | □ | □ | | | □ | □ |
| BTO | | | | | | | | | | | | | | | O | |
| CNT | ∠ | ∠ | X | O | | | | | X | | | | | | X | |
| Sn | | | | | O | | | O | O | | O | O | O | O | O | O |
| Ni | | | | | ∠ | ∠ | | ∠ | ∠ | ∠ | | | | | O | |
| Al | | | | | | | □ | | | | ∠ | | | | | |
| Cu | X | | | | X | | | | | | | | | | | |
| AlN | | | | | | | | | | | □ | □ | | | | |
| Ag | O | O | O | X | | | | | O | | | | | | O | |
| Ag/ CNT | ∠ | ∠ | X | O | | | | | X | | | | | | X | |

Printing quality was evaluated with four different level where X, \angle , \square , and O denote not deposited, scattered, deposited, and patterned, respectively. This dissertation has focused on AgNPs, multi-walled CNTs (MWCNTs), and AgNPs/MWCNTs nanocomposite with various substrates including PET, polyimide, silicon wafer, CFRP, GFRP, and PDMS for applications to strain sensors as shown in **table 3.2**.

Table 3.2. Material–substrate compatibility of AFN printing process focused on AgNP, MWCNT, and AgNP/MWCNT composite

| Substrates | | Materials | | |
|------------|--------------|-----------|----------|-----------------------|
| | | AgNP | MWCNT | AgNP/MWCNT Composites |
| PET | | O | X | X |
| Polyimide | | O | X | X |
| Silicon | | O | X | X |
| CFRP | | O | \angle | \angle |
| GFRP | | O | \angle | \angle |
| PDMS | Sylgard 184 | X | O | O |
| | EcoFlex 0030 | X | O | O |

AgNP was well deposited onto relatively hard substrates such as commercial PET, Kapton polyimide film (DuPont, USA), and commercial silicon wafer treated by hydrogen fluoride (HF) while MWCNTs showed poor printing quality.

Since MWCNT is more brittle than AgNP, it was mechanically broken when it bumped into hard substrates. Hence, AgNPs/MWCNTs composite was also not printed well onto hard substrates and only AgNPs were remained.

In terms of carbon fibre reinforced plastic (CFRP) and glass fibre reinforced plastic (GFRP), AgNPs showed similar printing quality to deposition onto hard materials while MWCNTs were selectively attached. Since FRP usually has directional properties, MWCNT was printed onto saddle between each fibre structure. However, major obstacle of using CFRP or GFRP as a substrate of strain sensor is their electrical conductivity which disturbs measuring electrical resistance of printed conductive nanomaterial pattern separately.

However, soft substrates such as polydimethylsiloxane (PDMS) showed completely different results. Specifically, Sylgard 184 (Dow Corning, Inc., Midland, MI) and EcoFlex 0030 (Smooth-on, Inc., Macungie, PA) were used which are types of PDMS with low elastic modulus of 1.84 MPa and 0.07 MPa, respectively. AgNP bounced back when it collided with soft substrates, but MWCNT was brittle enough to broke and printed onto substrates.

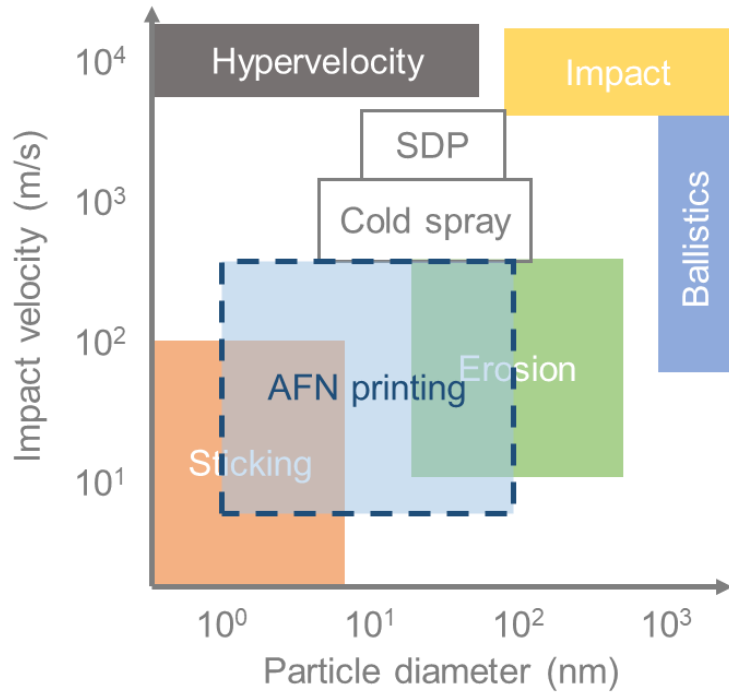


Figure 3.1. The printing principle according to impact velocity and particle diameter

Previous research demonstrated that the printing or deposition principle could be varied according to impact velocity and material diameter as shown in **figure 3.1** [76]. In consideration of AFN printing condition, it was expected that combination of sticking and erosion is occurred during AFN printing process and achieve the material deposition.

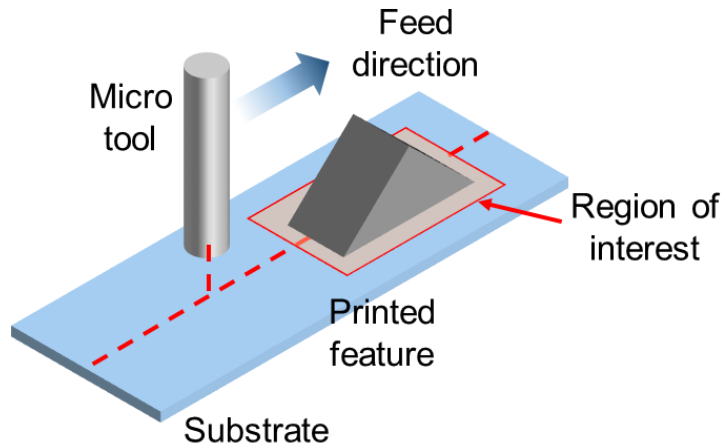


Figure 3.2. The schematic diagram for the observation of interfacial layer

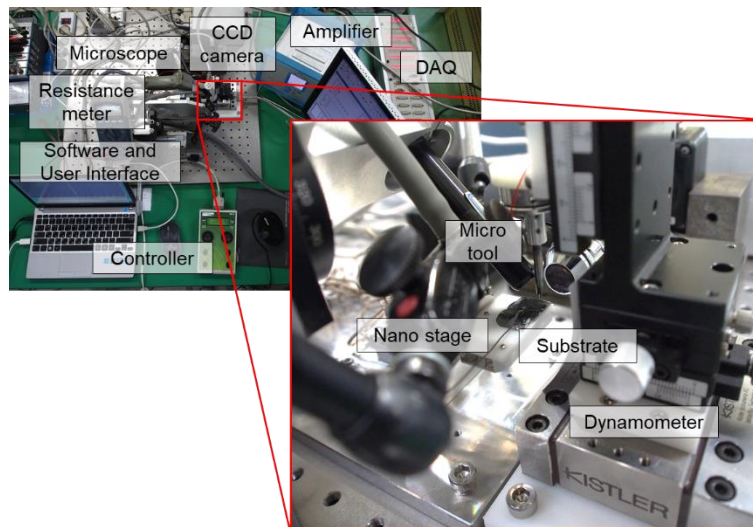


Figure 3.3. The photograph of experimental setup for micro-machining for detaching printed pattern

To investigate the printing mechanism empirically, experimental setup for micro-machining was configured as shown in **figures 3.2** and **3.3**. Using the mechanical force during micro-machining process, printed pattern was detached from the substrate.

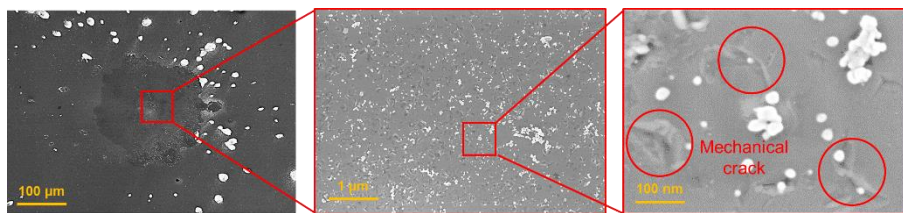


Figure 3.4. SEM image of mechanical crack in interfacial layer

As shown in **figure 3.4**, interfacial layer between material and substrate was observed by SEM image. The debris of NPs and mechanical crack were measured which demonstrate that the mechanical crack was generated by during AFN printing.

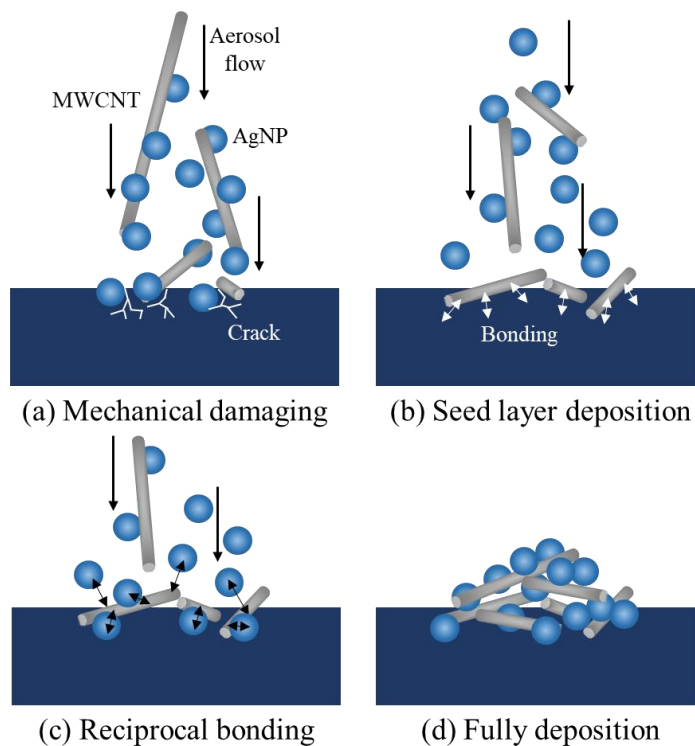


Figure 3.5. The schematic diagram of printing mechanism of nanocomposite composed of AgNPs and MWCNTs on flexible substrate

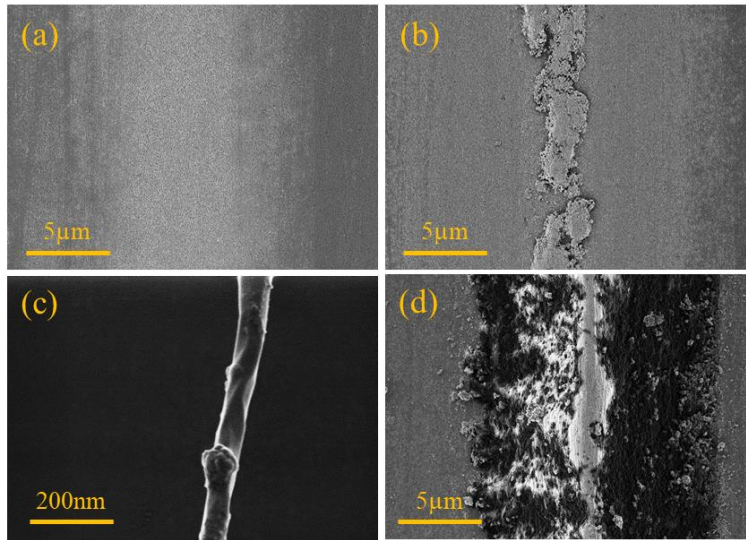


Figure 3.6. SEM image of nanocomposite printing by printing steps

Understanding deposition mechanism of nanomaterial at room temperature is important for improving the printing quality and finding proper applications. **Figure 3.5** shows deposition mechanism of AgNPs/MWCNTs nanocomposite onto soft and flexible polymer substrate and **figure 3.6** shows SEM images for each steps of printing in order of mechanical damaging, seed layer deposition, reciprocal bonding, and fully deposition.

Impact velocity of nanocomposite was assumed to be around 200 ms^{-1} following the gas velocity from CFD analysis in previous studies [77]. It was enough to generate cracks on the top surface of substrate, and mechanical locking between nanomaterials and substrate through cracks was occurred. Then, mechanically locked MWCNTs on EcoFlex 0030 behaved as a seed layer for followed nanomaterial.

After seed layer deposition, AgNPs and MWCNTs were reciprocally bonded each other. Using reciprocal bonding, partial aggregations were followed that aerosolised AgNPs were collided with embedded MWCNTs seed layer. As partial aggregation of nanocomposite grew bigger, conductive line pattern was fully printed onto substrate.

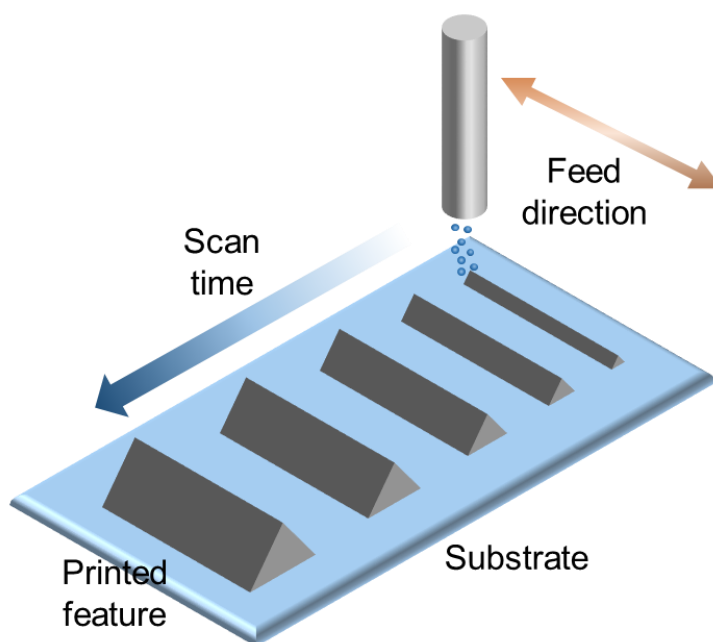


Figure 3.7. The schematic diagram of AFN printed pattern by printing steps to investigate printing mechanism

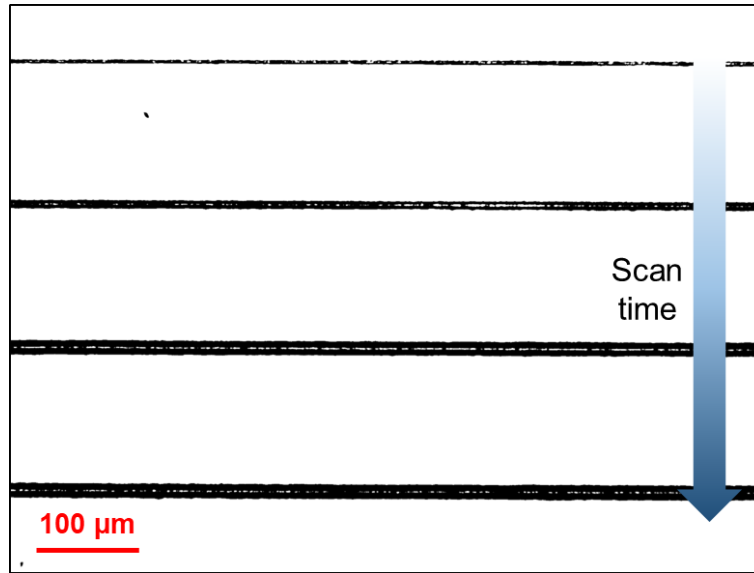


Figure 3.8. The optical microscopic image of AFN printed pattern by printing steps to investigate printing mechanism

To investigate the printing mechanism, SEM images of single line patterns were measured at each printing step as shown in **figure 3.7**. The patterns printed onto identical substrate exhibited various pattern width according to printing step as shown in **figure 3.8** for not only nanocomposite composed of AgNPs and MWCNTs but also only AgNPs.

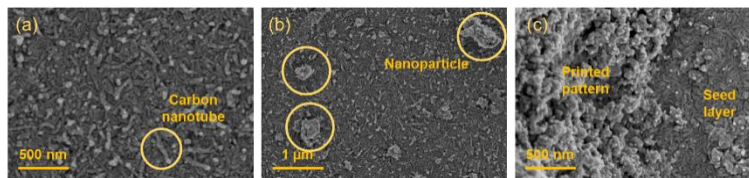


Figure 3.9. SEM image of nanocomposite printing in order of (a) seed layer deposition, (b) partial aggregation, and (c) fully deposition

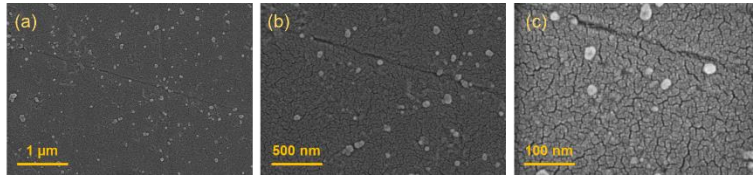


Figure 3.10. SEM image of nanoparticle printing in order of (a), (b), and (c).

Figure 3.9 shows the SEM image of nanocomposite composed of AgNPs and MWCNTs. It was well demonstrated that MWCNT was deposited as a seed layer at the beginning of printing step followed by AgNP deposition. However, only AgNP was not printed well onto PDMS substrate but just generated mechanical crack on the top of the surface as shown in **figure 3.10**.

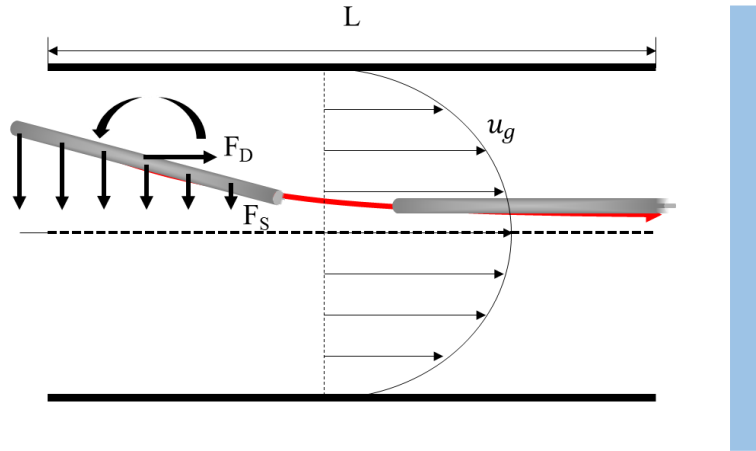


Figure 3.11. The free body diagram of drag and Saffman's lift forces for CNT in the upstream of the nozzle

Figure 3.11 shows the free body diagram of CNT in the upstream of the nozzle. Since Saffman's lift force occurs when the velocities of material and aerosol are different each other, CNT that was not parallel to the aerosol streamline received the different magnitude Saffman's lift force at each position of the CNT. The forces with different magnitude according to the position of the CNT created a rotational force on CNT, causing them to move parallel to the streamline during their transportation as shown in **equations 3.1** and **3.2** where m_t and L_t represent the mass and length of nanotube, respectively while θ represents the tilted angle between CNT and aerosol flow.

$$\int_0^{L_t} F_S \cos \theta \cdot dL = \frac{1}{3} m_t L_t^2 \frac{d\theta}{dt} \quad \text{Equation 3.1}$$

$$F_S(L) = 1.615 \sqrt{\rho_g \mu} d_m^2 \left\{ u_{max} \left(1 - \frac{L^2 \sin^2 \theta}{R^2} \right) - u_m \right\} \sqrt{-\frac{du_g}{dr}} \quad \text{Equation 3.2}$$

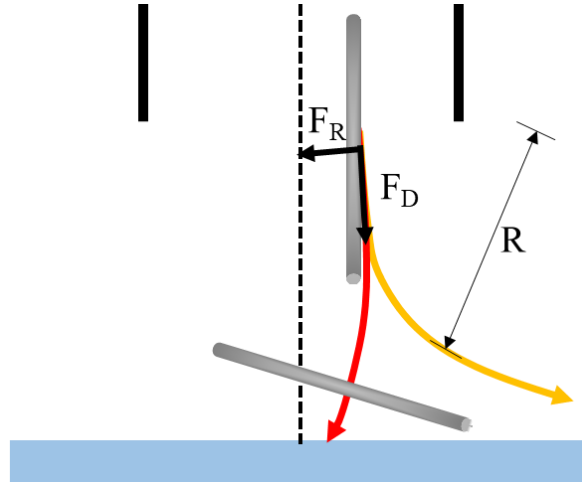


Figure 3.12. The free body diagram of drag and centrifugal forces for CNT in the downstream of the nozzle

Figure 3.12 shows the free body diagram of CNT in the downstream of the nozzle. Since the radius of the centrifugal force varies depending on the position of the CNT, the magnitude of the centrifugal force varies according to the position of the CNT which also generated the rotation of CNT as shown in and **equation 3.3**.

$$\int_0^{L_t} F_R \cos\theta \cdot dL = \frac{1}{3} m_t L_t^2 \frac{d\theta}{dt} \quad \text{Equation 3.3}$$

Figure 3.13 shows the optical microscopic image of nanocomposite printing by printing steps. At the first time of printing, it was not enough to generate seed layer on the surface of substrate. As printing process continues more than specific time for same pattern, seed layer deposition were occurred.

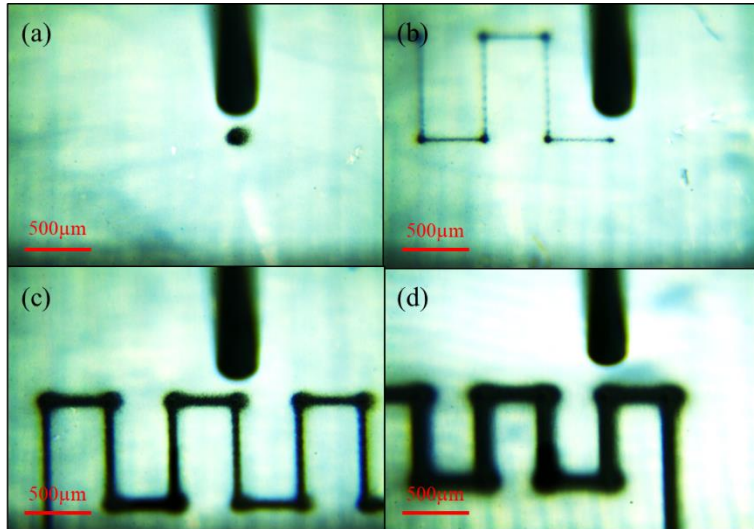


Figure 3.13. The optical microscopic image of nanocomposite printing by printing steps

Figure 3.14 shows surface profile of AFN printed line on each printing step, which explains deposition mechanism well. The increase of pattern width caused not only the change of mechanical properties of AFN printed pattern but also the packing ratio. Since packing ratio indicates that how porous of the pattern, the control of packing ratio influenced the electrical properties of pattern. It was discussed above that more porous pattern showed high electrical resistivity and high GF.

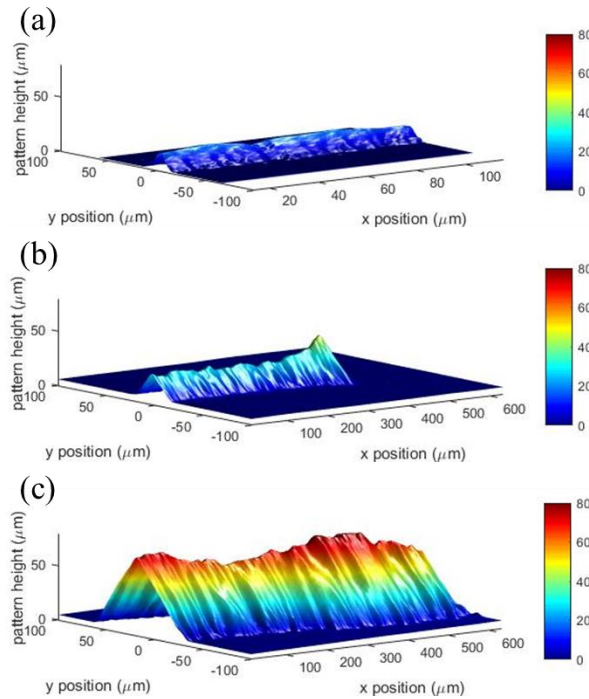


Figure 3.14. The confocal microscopic image of nanocomposite printing by printing steps

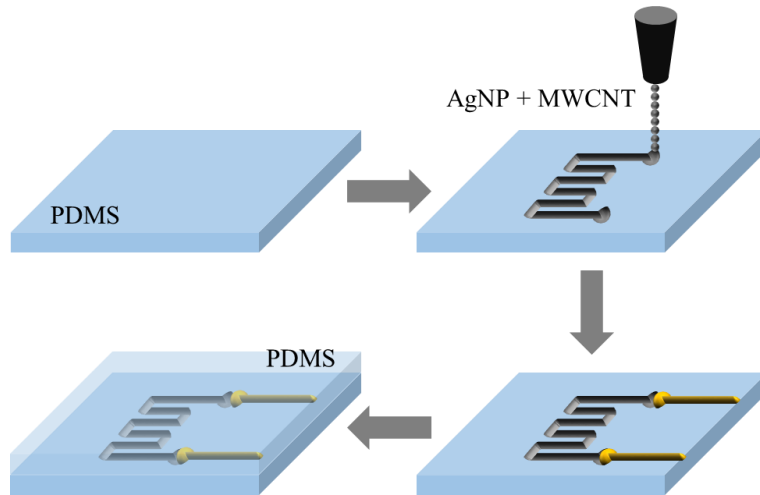


Figure 3.15. The schematic diagram of fabrication process of highly sensitive and wide measuring sensor

Figure 3.15 shows fabrication process for nanocomposite sensor. EcoFlex 0030 was used as a substrate of nanocomposite sensor for soft–continuous deformation. AFN printing process of AgNPs/MWCNTs composite was followed on desired position of substrate to fabricate shape similar design to commercial strain gauge. After soldering and wiring for measurement, another flexible polymer layer was attached as a cover layer for electrical insulation and mechanical protection. Silver paste was used to connect the tip of printed sensor and electrical wire for data acquisition.

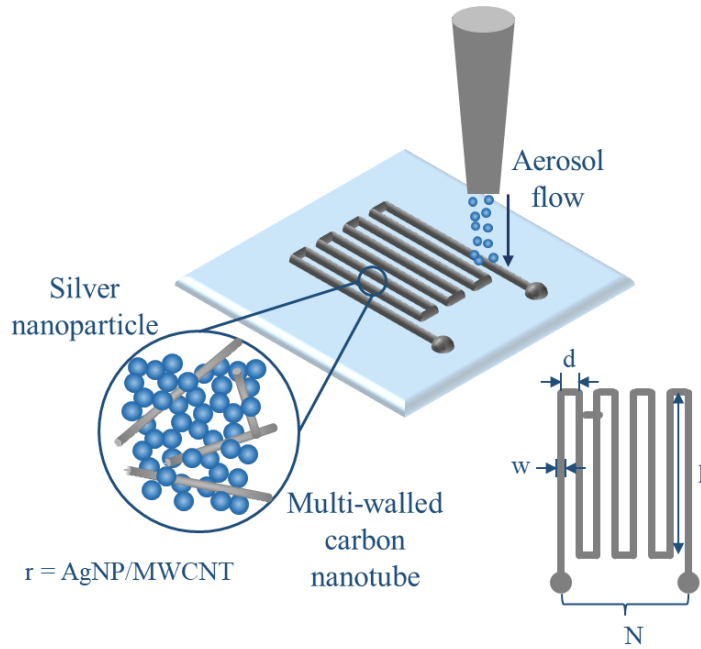


Figure 3.16. Design variables for the fabrication of highly sensitive and wide measuring sensor

Table 3.3. Optimised design variables for the fabrication of highly sensitive and wide measuring sensor

| Nomenclature | Description | Control | Value |
|--------------|-------------------------|-----------------------|-----------------------|
| d | Distance between finger | Design parameter | 0.5 mm |
| l | Finger length | Design parameter | 7 mm |
| w | Finger width | AFN process parameter | 16 – 51 μm |
| N | Number of finger | Design parameter | 4 |
| r | Mass ratio of composite | Material preparation | 2.5 – 20 |

Figure 3.16 and **table 3.3** show the design variables and optimised design variables for the fabrication of highly sensitive and wide measuring sensor. Based on the design of commercial strain gauge, distance between finger, finger length, finger width, number of finger, and mass ratio of composite were controlled to achieve highest performance in terms of sensitivity and measurable range.

Figures 3.17 and **3.18** show the photograph and optical microscopic (BX53M, Olympus, Japan) image of printed sensor, respectively. Printed sensor had width of 3.5 mm and length of 7 mm with distance between line patterns of 0.5 mm.

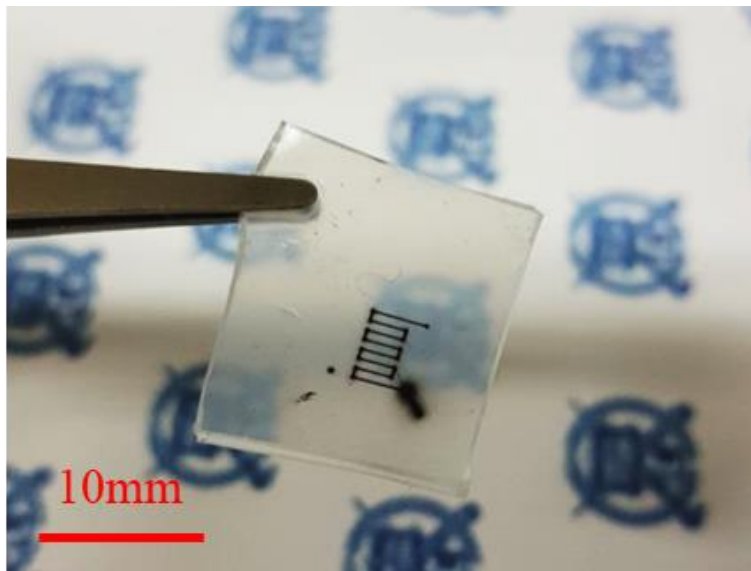


Figure 3.17. The photograph of fabricated highly sensitive and wide measuring sensor

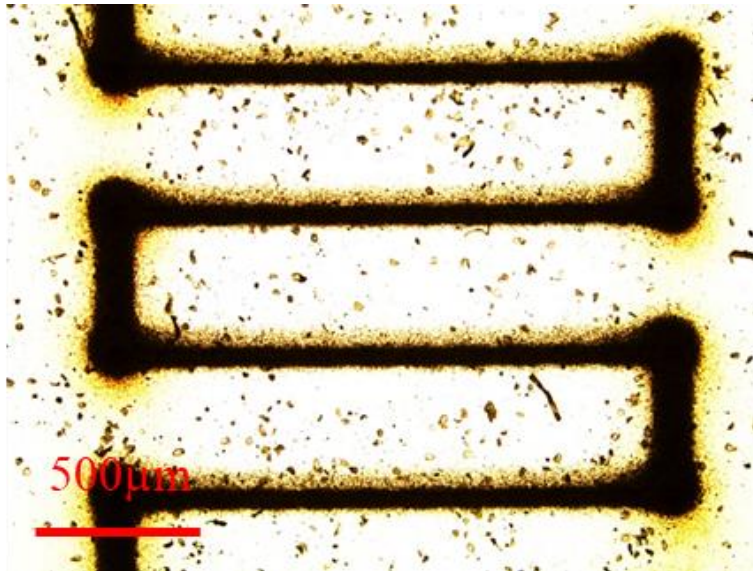


Figure 3.18. The optical microscopic image of fabricated highly sensitive and wide measuring sensor

3.2. Sensing performance evaluation

Figure 3.19 shows schematic diagram of sensing mechanism of nanocomposite sensor composed of AgNPs and MWCNTs. A change of contact resistance among AgNPs were dominant factor of sensitivity for resistive type NPs sensor. It showed high sensitivity due to drastic relative resistance change by detachment among NPs which was generated by mechanical elongation. However, it showed narrow measurable range because they were electrically disconnected after their mechanical detachment [78].

In comparison to strain sensor composed of only metal NPs, CNTs widened measurable range of strain sensor. In terms of nanocomposite, electrical connection between nanomaterials could be remained at identical mechanical elongation because NPs were still attached to CNT.

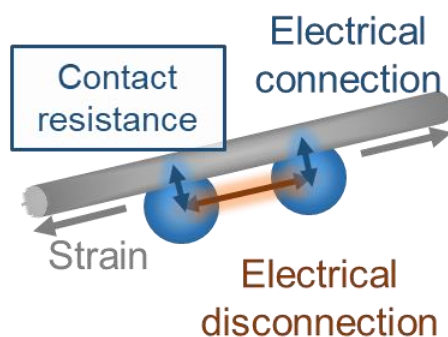


Figure 3.19. The schematic diagram of sensing mechanism of nanocomposite sensor

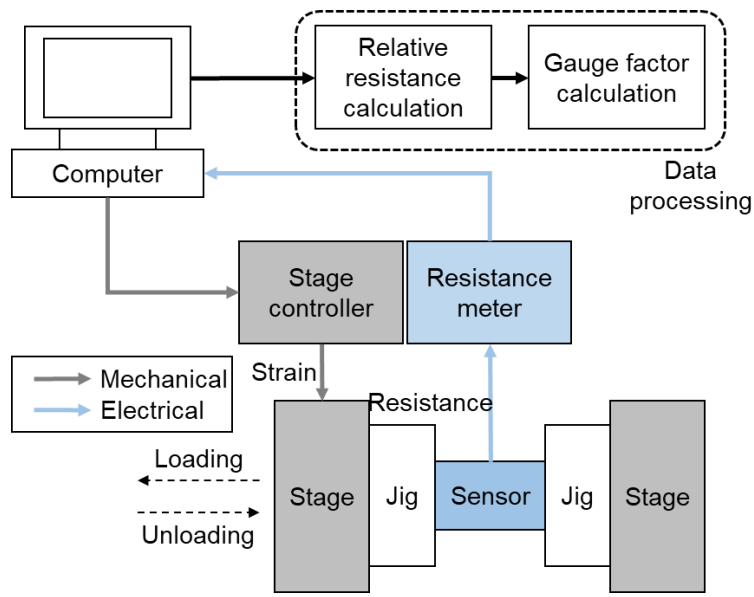


Figure 3.20. The schematic diagram of sensing mechanism of nanocomposite sensor

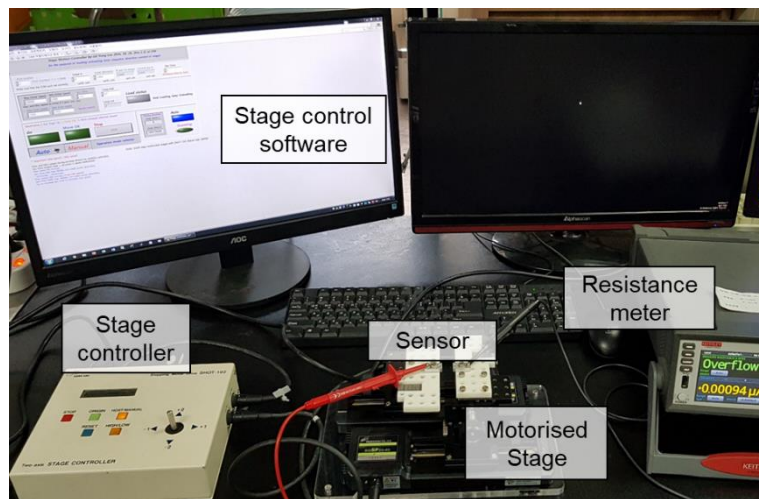


Figure 3.21. The photograph of sensing mechanism of nanocomposite sensor

Table 3.4. The resistance and resolution of electrical components for experimental setup

| Component | Resistance (Ω) | Resolution (Ω) |
|-------------------|-------------------------|-------------------------|
| Fabricated sensor | 10 – 30 | 0.15 |
| Solder | 10^{-3} | — |
| Lead wire | 10^{-6} | — |
| Resistance meter | — | 10^{-14} |
| Adapter | — | 10^{-14} |

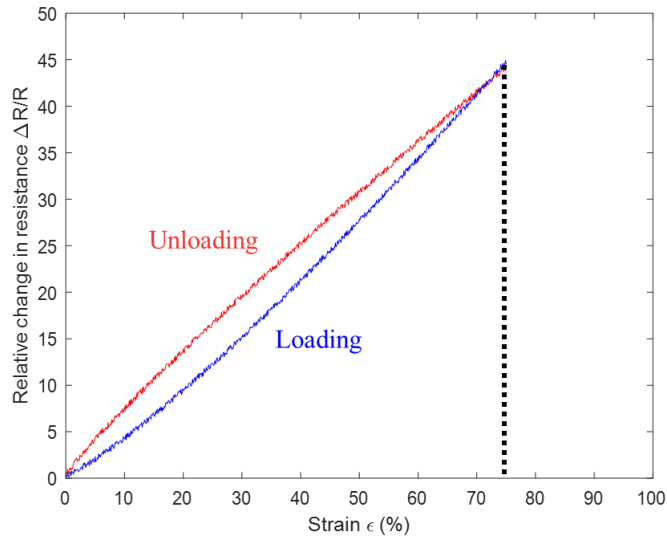


Figure 3.15. The evaluation results of sensing performance of highly sensitive and wide measuring sensor

To evaluate the sensor performance, in-situ mechanical and electrical setup was configured to measure the sensitivity and measurable range simultaneously as shown in **figures 3.20** and **3.21**. Printed sensor was stretched using multi-axis stage controlled by stage controller and relative resistance change was measured using data acquisition device. Pre-processing of raw resistance data was conducted using connected computer software programmed by LabVIEW (National Instruments, USA). **Figure 3.22** shows sensitivity and measurable range of the printed strain sensor. The maximum strain limit of fabricated strain sensor was reached up to 74%. Besides, it possessed GF of 58.7 at same condition.

Mechanical stability is also an important factor for performance of strain sensor. **Figure 3.23** shows life cycle evaluation test results for printed sensor. Life cycle evaluation test was conducted by 1,000 times of loading and unloading cycles. After first 10 – 20 cycles to stabilised, printed sensor remained stable and the variance in peak resistance was under 5%. Most of single resistance variance showed similar behaviour by followed elongation test.

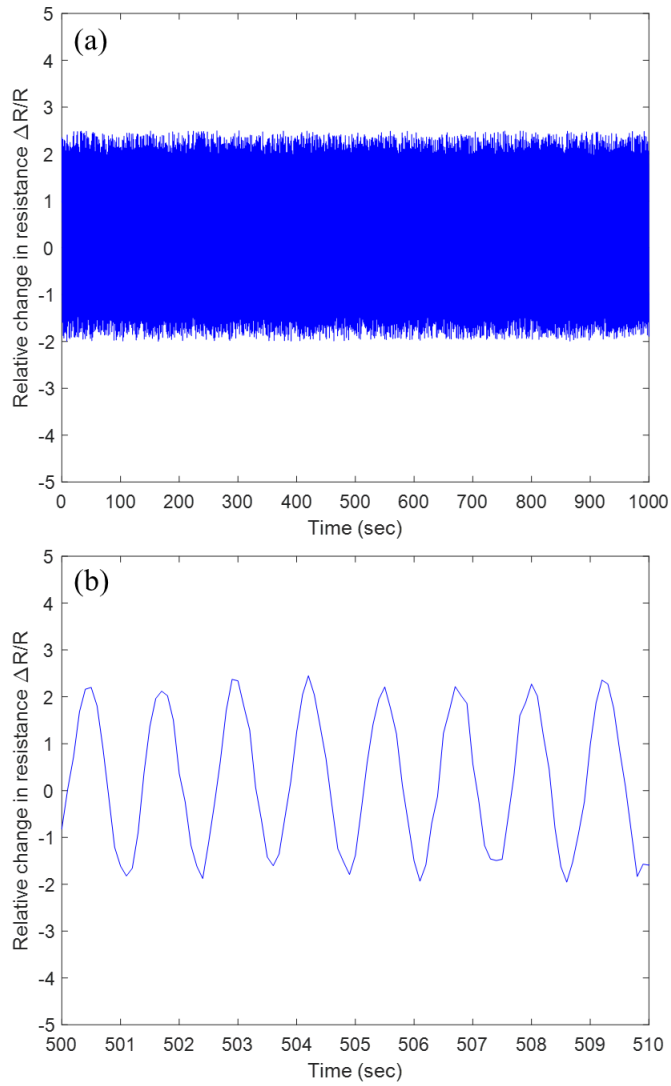


Figure 3.23. (a) The evaluation results of life-cycle test for highly sensitive and wide measuring sensor and (b) its magnified view

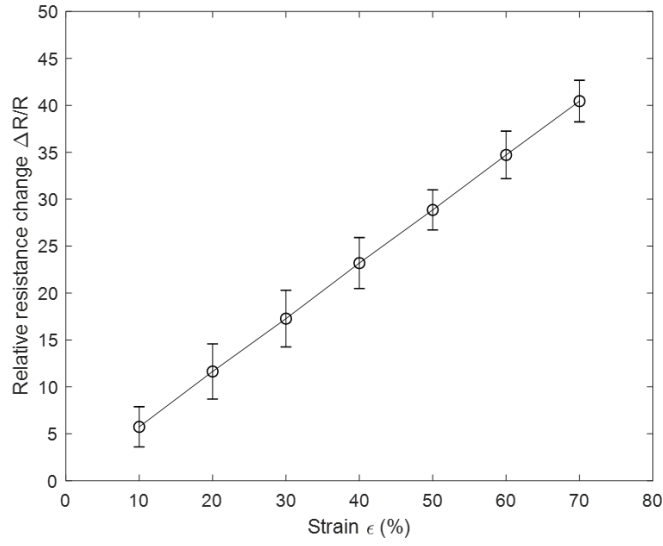


Figure 3.24. The evaluation results for average and standard deviation value during life-cycle test according to strain

Table 3.5. The reliability evaluation results during life-cycle test

| Strain (%) | Average ($\Delta R/R$) | Deviation ($\Delta R/R$) | Maximum ($\Delta R/R$) | Minimum ($\Delta R/R$) |
|------------|-----------------------------|-------------------------------|-----------------------------|-----------------------------|
| 10 | 5.7385 | 2.1414 | 12.7294 | 1.4192 |
| 20 | 11.6409 | 2.9426 | 20.4861 | 2.4814 |
| 30 | 17.2723 | 3.0199 | 26.7932 | 4.5136 |
| 40 | 23.1935 | 2.7135 | 33.3897 | 16.0486 |
| 50 | 28.8607 | 2.1338 | 36.3416 | 22.7063 |
| 60 | 34.7181 | 2.5350 | 42.5107 | 25.8174 |
| 70 | 40.4522 | 2.2173 | 47.4247 | 33.7434 |

For 1,000 times of loading and unloading cycles, average value and standard deviation value were calculated in strain from 10 to 70 % by 10% steps. **Figure 3.24** and **table 3.5** show the evaluation results during life-cycle tests for reliability evaluation of printed sensor.

Figures 3.25 and **3.26** show parametrisation of nanocomposite sensors. The relative mass of AgNPs to MWCNNTs, and scan time of AFN printing process were used as parameters for this dissertation. A composition ratio of nanocomposite was a primary indicator for properties of nanocomposite sensor, which controlled both sensitivity and measurable range. GF increased as the portion of AgNPs increased while maximum strain limit decreased. As discussed above, since sensitivity was usually governed by detachment between AgNPs and stretchability was governed by MWCNTs, GF and maximum strain limit showed opposite behaviour by relative mass of AgNPs to MWCNTs.

In terms of scan time, it was verified that large scan time resulted high packing ratio for nanocomposite in conductive line pattern. Since the close distance between AgNPs prevented them from falling apart, high packing ratio decreased sensitivity of nanocomposite patterns. Hence, GF decreased as scan time increased due to the change of packing ratio. However, maximum strain limit was almost remained by the change of scan time. According to the results, it was demonstrated that GFs and maximum strain limit could be controlled independently.

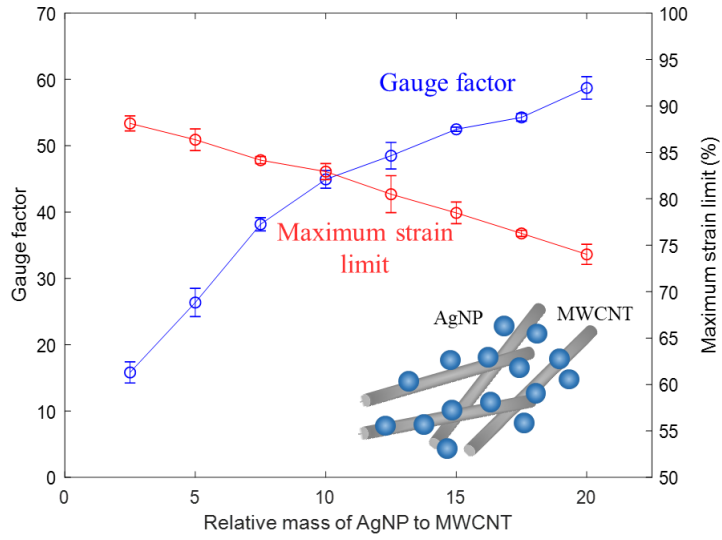


Figure 3.25. The experimental results of sensitivity and measurable range according to composition ratio

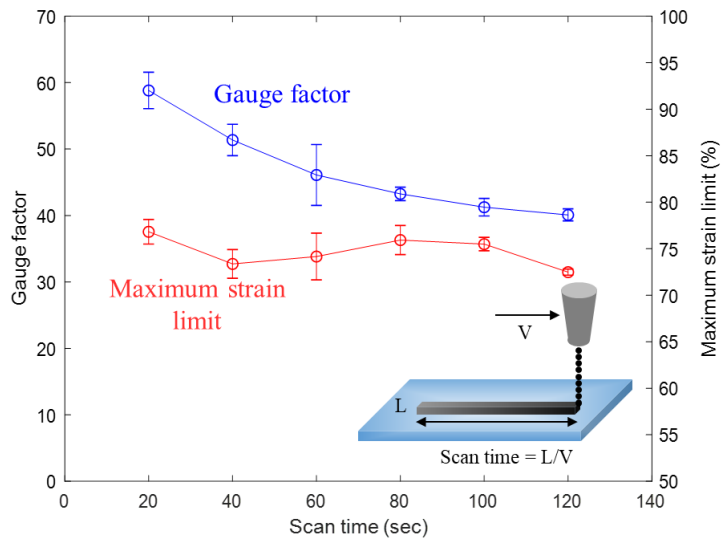


Figure 3.26. The experimental results of sensitivity and measurable range according to scan time

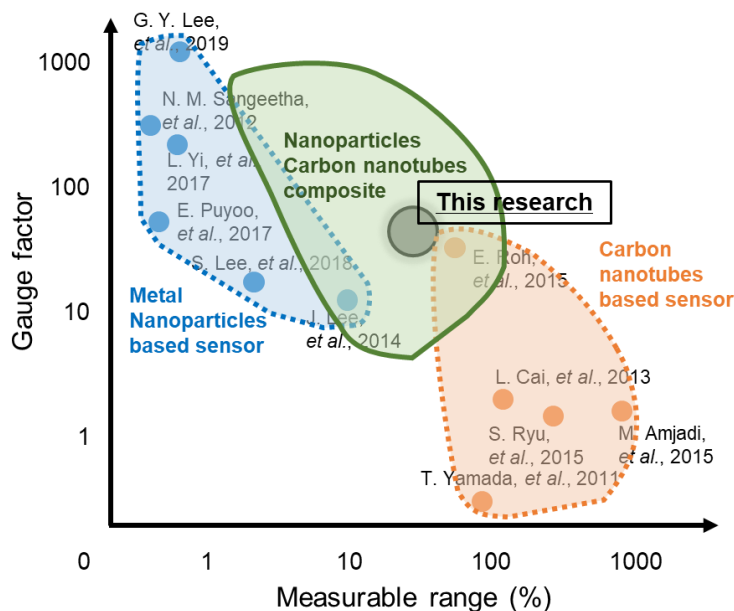


Figure 3.27. The results of this research according to GF and maximum strain limit in comparison to state-of-the-art

Figure 3.27 shows sensitivity (GF) and maximum strain limit graph for fabricated highly sensitive and wide measuring sensor. Metal NPs based sensors showed high sensitivity but low stretchability due to their sensing mechanism. Mechanical separation between NPs enabled drastic change of relative resistance but also electrically disconnected above specific level of strain. However, CNTs based strain sensors showed low sensitivity but wide measurable range. CNTs, which are electrically conductive and also highly stretchable enabled wide measurable range for strain sensor. Developed nanocomposite sensor used high sensitivity of AgNPs and wide measurable range of MWCNTs at once.

The vibration sensing mechanism of sensor could be explained by electron tunnelling effect between nanomaterials. The distance between nanomaterials varied according to applied vibration occurred the change of electrical conductance due to the change of tunnelling current as shown in **figure 3.28**.

To evaluate not only strain sensing performance but also vibration sensing performance, sensing performance evaluation test for vibration was also conducted. The printed sensor was directly attached to a vibration shaker (Vibration testing shaker, TIRA GmbH, Germany) and relative resistance change was measured during a various type of continuous vibration as shown in **figure 3.29**.

First, experiments were conducted by applying a vibration with the amplitude of 8 μm at different frequencies of 100, 200, and 400 Hz, respectively. According to frequency analysis results by fast Fourier transform (FFT), it was confirmed that amplitude spectrum of similar magnitude was obtained at each vibration frequency as shown in **figures 3.30–3.32**.

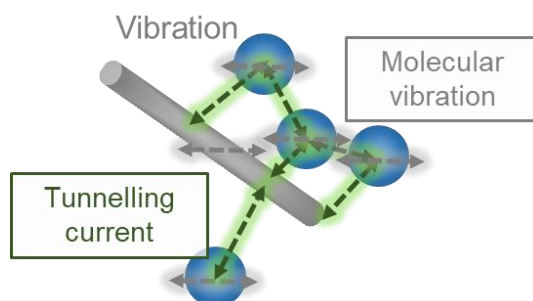


Figure 3.28. The schematic diagram of vibration sensing mechanism of nanocomposite sensor

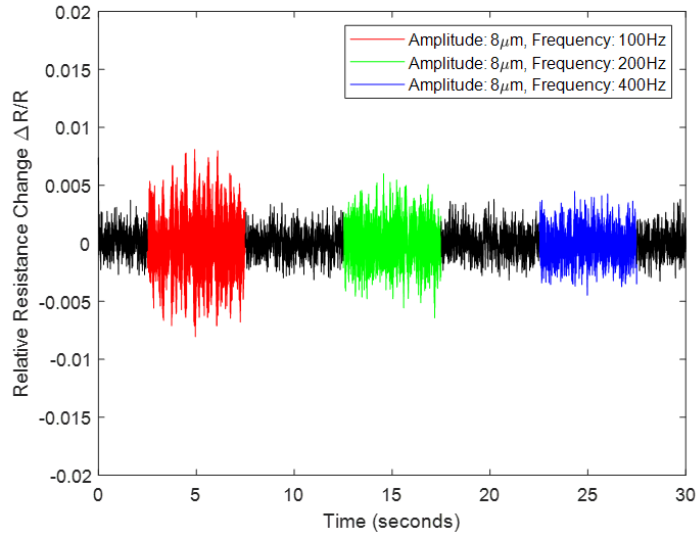


Figure 3.29. The experimental results of relative resistance change of printed sensor by various vibrations with amplitude of 8 μm

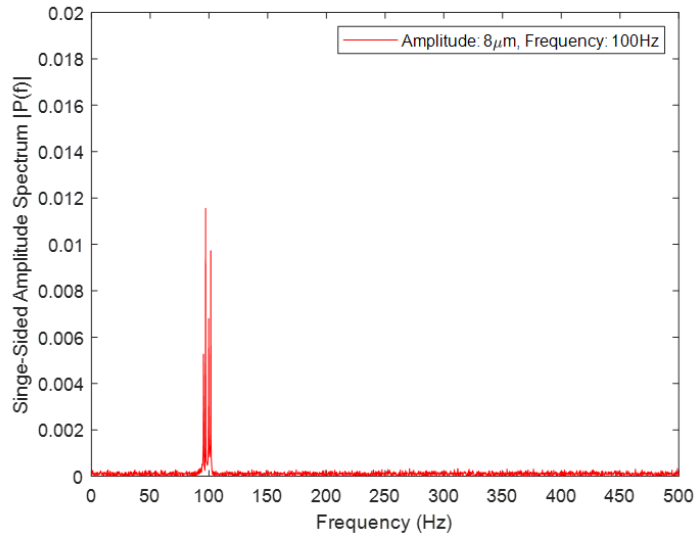


Figure 3.30. FFT results of relative resistance change of printed sensor by vibration amplitude of 8 μm and frequency of 100 Hz

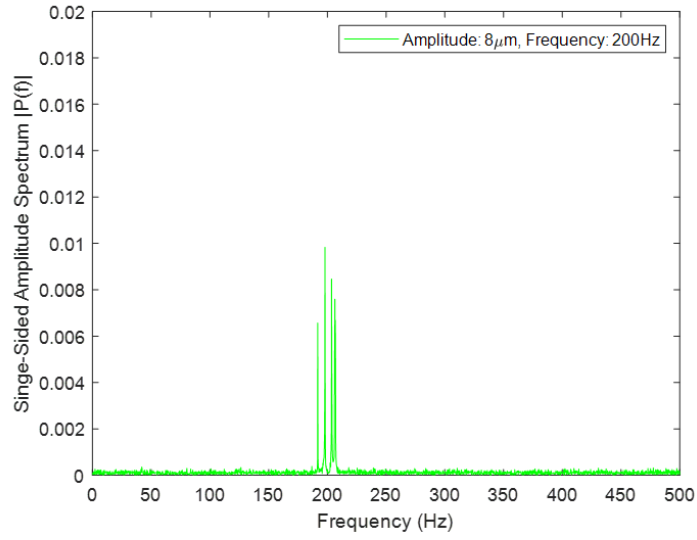


Figure 3.31. FFT results of relative resistance change of printed sensor by vibration amplitude of 8 μ m and frequency of 200 Hz

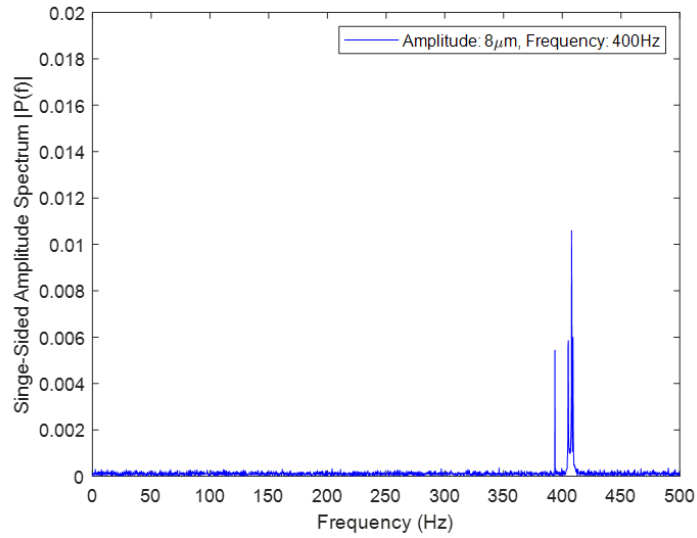


Figure 3.32. FFT results of relative resistance change of printed sensor by vibration amplitude of 8 μ m and frequency of 400 Hz

Likewise, it was demonstrated that amplitude spectrum was proportional to the actual vibration amplitude in the experiment with different vibrations with various amplitudes of 4, 8, and 12 μm at frequency of 200 Hz as shown in **figures 3.33–3.36**. Hence, it was validated that the printed vibration sensor was capable of vibration measurement in several hundreds of Hz with several μm amplitude which is appropriate to be utilised in mechanical manufacturing process including conventional machining process.

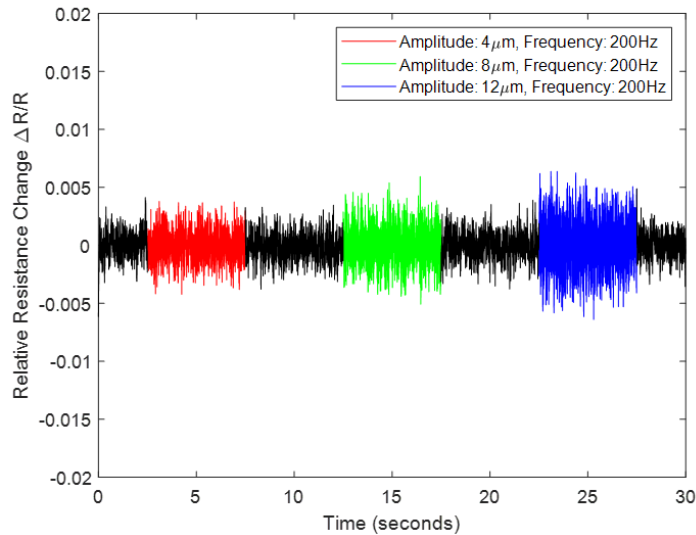


Figure 3.33. The experimental results of relative resistance change of printed sensor by various vibrations with frequency of 200 Hz

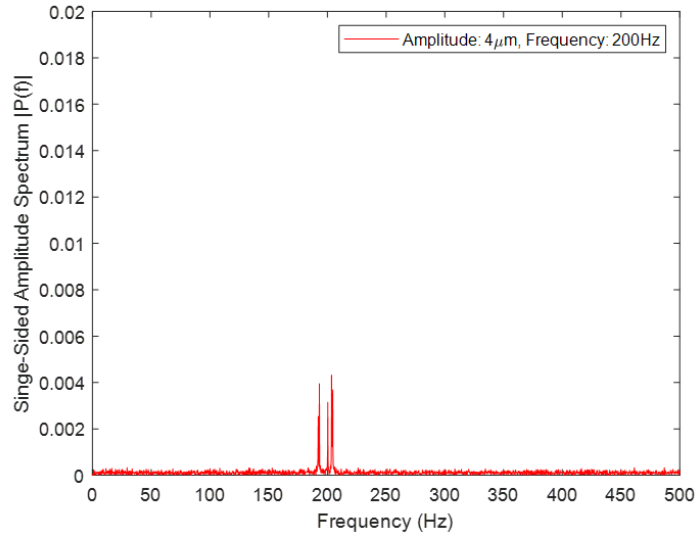


Figure 3.34. FFT results of relative resistance change of printed sensor by vibration amplitude of 4 μm and frequency of 200 Hz

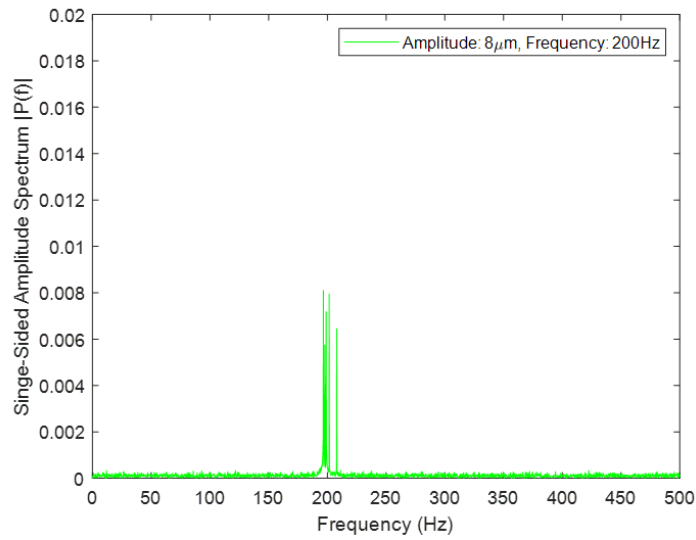


Figure 3.35. FFT results of relative resistance change of printed sensor by vibration amplitude of 8 μm and frequency of 200 Hz

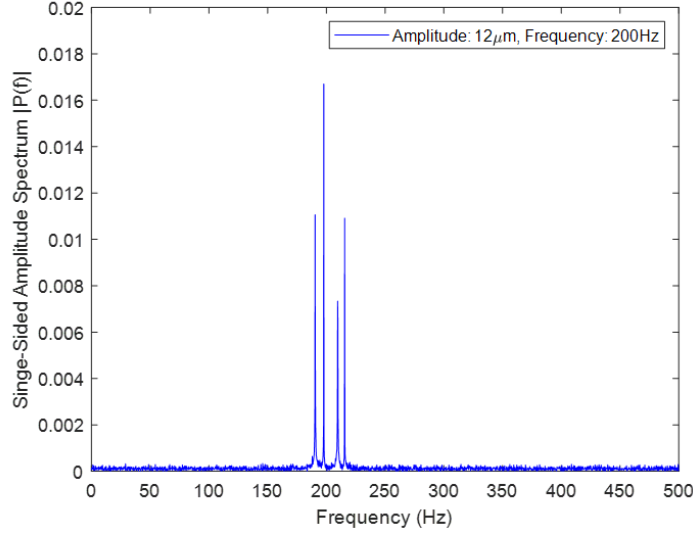


Figure 3.36. FFT results of relative resistance change of printed sensor by vibration amplitude of 12 μm and frequency of 200 Hz

To verify the reliability of vibration sensing performance of printed sensor, evaluation of sensor frequency according to induced frequency was conducted using quality factor (Q-factor) [79]. **Figure 3.37** shows the bandwidth of single-sided amplitude spectrum of sensor data according to vibration frequency of 100 Hz at Q-factor equals to 70.7%. The average and standard deviation value of spectrum was calculated with Q-factor level at 70.7%.

Figures 3.38, 3.39 and **table 3.6** show the results of frequency response according to induced frequency with Q-factor at 70.7% and its normalised results, respectively. It was demonstrated that printed sensor was capable of not only strain sensing but also vibration sensing.

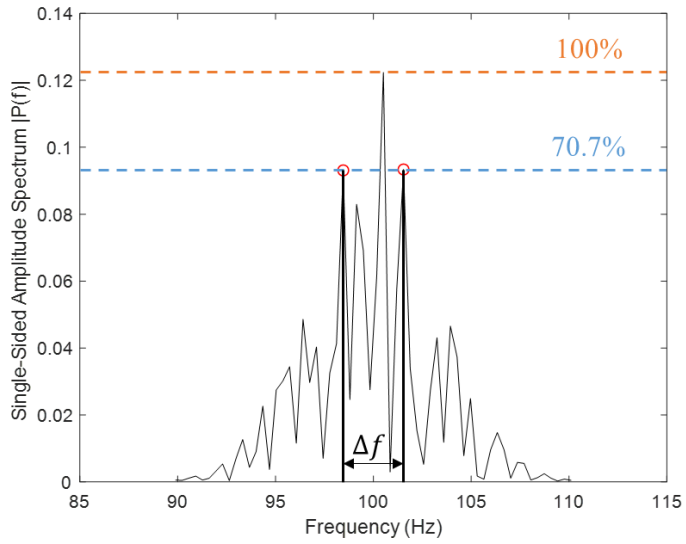


Figure 3.37. The bandwidth of amplitude power spectrum of 100 Hz vibration at Q-factor at 70.7%

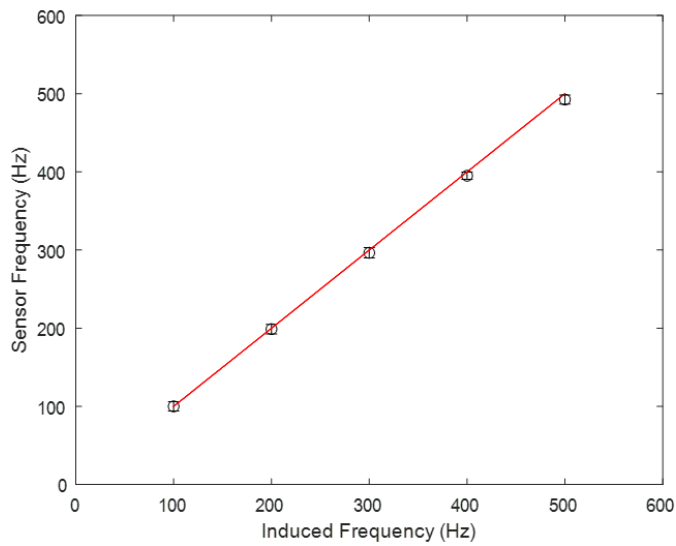


Figure 3.38. The evaluation results of frequency response of printed sensor according to induced frequency with Q-factor at 70.7%

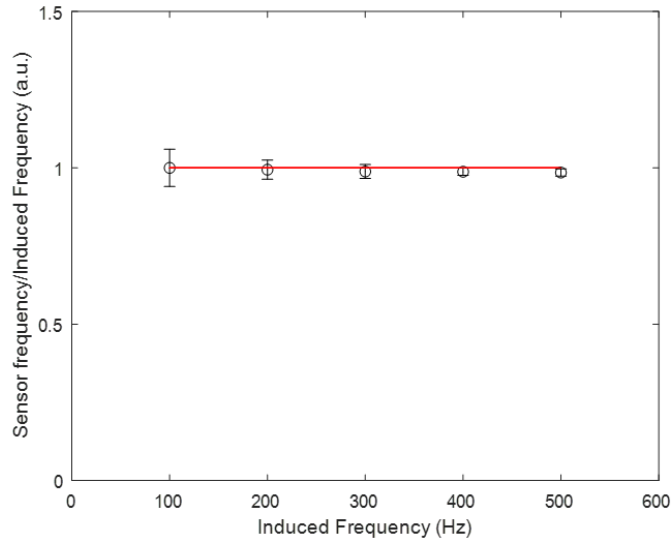


Figure 3.39. The normalised evaluation results of frequency response of printed sensor according to induced frequency with Q-factor at 70.7%

Table 3.6. The results of frequency response of printed sensor according to induced frequency with Q-factor at 70.7%

| Frequency (Hz) | Average (Hz) | Deviation (Hz) | Maximum (Hz) | Minimum (Hz) |
|-------------------|-----------------|-------------------|-----------------|-----------------|
| 100 | 99.829 | 1.9865 | 102.23 | 97.432 |
| 200 | 198.91 | 1.6966 | 201.13 | 196.57 |
| 300 | 295.99 | 1.4819 | 298.22 | 294.39 |
| 400 | 395.30 | 1.5278 | 397.53 | 393.11 |
| 500 | 493.04 | 0.7562 | 493.97 | 492.01 |

In order to verify that the strain and vibration could be separated each other, a statistical verification was conducted. First, sensor data was divided by strain, vibration and random noise component for further analysis as shown in **equation 3.4** where X_t is sensor signal, S_t is strain component, V_t is vibration component, E_t is normal random noise component.

$$X_t = S_t + V_t + E_t \quad \text{Equation 3.4}$$

As shown in **equation 3.5**, the null hypothesis H_0 which denotes that the resistance change of sensor was only influenced by strain component was set. Otherwise, the alternative hypothesis H_1 assumed that the resistance change of the sensor was influenced by both independent strain and vibration component as shown in **equation 3.6**.

$$H_0: X_t = S_t + E_t \quad \text{Equation 3.5}$$

$$H_1: X_t = S_t + A\cos(2\pi f_c t) + B\sin(2\pi f_c t) + E_t \quad \text{Equation 3.6}$$

To test the probability of hypothesis, analysis of variance (ANOVA) based on F-distribution was conducted. In consideration of the statistical degree-of-freedom of sensor data, variable was defined to follow the F-distribution without scaling as shown in **equation 3.7** [80].

$$\frac{(\sum_i DF_i - DF_t - 1)SS_t/DF_t}{\sum_i SS_i - I(0) - SS_t} \sim F(DF_t, \sum_i DF_i - DF_t - 1) \quad \text{Equation 3.7}$$

Tables 3.7–3.9 show the statistical results of printed sensor according to vibration with frequency of 200, 400, and 600 Hz, respectively. The degree of freedom and sum of squares were calculated respectively with frequency source from 0 to 600 Hz in 100 Hz steps for further analysis.

Table 3.7. The statistical results of printed sensor according to induced frequency with 200 Hz

| Source | Degree of freedom | Sum of squares |
|-------------|-------------------|----------------|
| $f_0 = 0$ | 1 | 3.78 |
| $f_0 = 100$ | 2 | 9.19 |
| $f_0 = 200$ | 2 | 50.72 |
| $f_0 = 300$ | 2 | 9.74 |
| $f_0 = 400$ | 2 | 4.75 |
| $f_0 = 500$ | 2 | 4.69 |
| $f_0 = 600$ | 2 | 4.57 |
| total | 13 | 87.44 |

Table 3.8. The statistical results of printed sensor according to induced frequency with 400 Hz

| Source | Degree of freedom | Sum of squares |
|-------------|-------------------|----------------|
| $f_0 = 0$ | 1 | 1.59 |
| $f_0 = 100$ | 2 | 5.6 |
| $f_0 = 200$ | 2 | 5.02 |
| $f_0 = 300$ | 2 | 3.96 |
| $f_0 = 400$ | 2 | 48.04 |
| $f_0 = 500$ | 2 | 12.32 |
| $f_0 = 600$ | 2 | 1.83 |
| total | 13 | 78.36 |

Table 3.9. The statistical results of printed sensor according to induced frequency with 600 Hz

| Source | Degree of freedom | Sum of squares |
|-------------|-------------------|----------------|
| $f_0 = 0$ | 1 | 7.65 |
| $f_0 = 100$ | 2 | 1.19 |
| $f_0 = 200$ | 2 | 5.73 |
| $f_0 = 300$ | 2 | 5.4 |
| $f_0 = 400$ | 2 | 8.78 |
| $f_0 = 500$ | 2 | 8.54 |
| $f_0 = 600$ | 2 | 48.63 |
| total | 13 | 85.92 |

By calculating probability value (p-value) which is the probability of obtaining test results at least as extreme as the results actually observed during the test by assuming that the null hypothesis is correct, it was decided to whether reject or accept null hypothesis [81]. In significance level of 0.05, null hypothesis was rejected and alternative hypothesis was accepted which means measurement independency of strain and vibration was validated as shown in **table 3.10**.

Furthermore, to estimate the reliability of test, Cronbach's alpha was also calculated as shown in **equation 3.8** [82]. It has been proposed that Cronbach's alpha could be viewed as the expected correlation of two tests that measure the same construct. By using above definition it was possible to accurately estimate the average correlation of a certain construct.

$$\alpha = \frac{k}{k-1} \left(1 - \frac{\text{var}(S) + \text{var}(V) + \text{var}(E)}{\text{var}(X)} \right) \quad \text{Equation 3.8}$$

Table 3.10. The results of p-value and Cronbach's alpha according to induced frequency

| Source | p-value | Cronbach's alpha |
|--------|---------|------------------|
| 200 Hz | 0.032 | 0.941 |
| 400 Hz | 0.018 | 0.966 |
| 600 Hz | 0.011 | 0.973 |

To evaluate the dynamic performance of printed sensor, power amplitude spectrum was measured according to vibration frequency as shown in **figure 3.40**. The amplitude spectrum of printed sensor was increased until 600 Hz then decreased until 1,000 Hz while the amplitude spectrum of commercial accelerometer was almost remained.

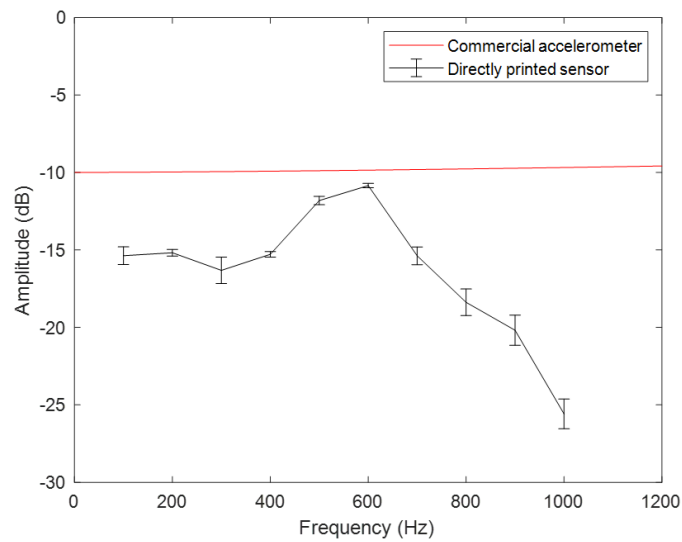


Figure 3.40. The comparison of amplitude by frequency of printed sensor to commercial accelerometer

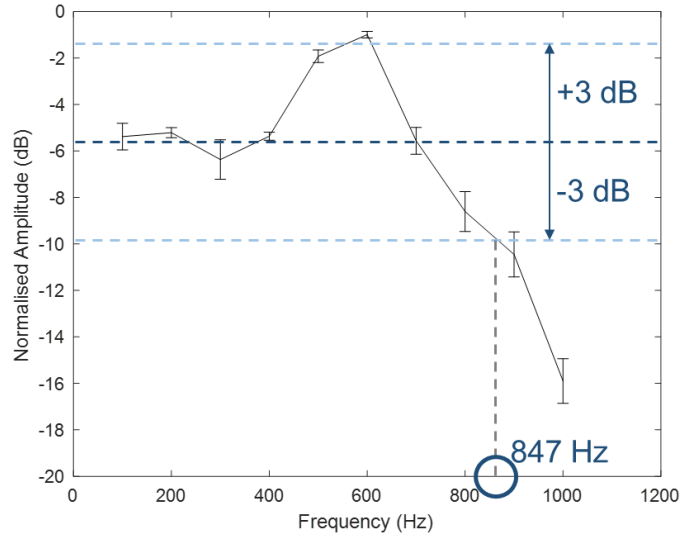


Figure 3.41. The 3dB test of printed sensor for evaluation of dynamic performance

The expected measurable range of printed sensor was evaluated by 3dB test. The normalised spectrum was calculated by amplitude spectrum of printed sensor divided by that of commercial accelerometer. According to amplitude spectrum at stagnated state, 3dB point was matched to 847 Hz which means the maximum value of measurable frequency of fabricated sensor without loss of reliability.

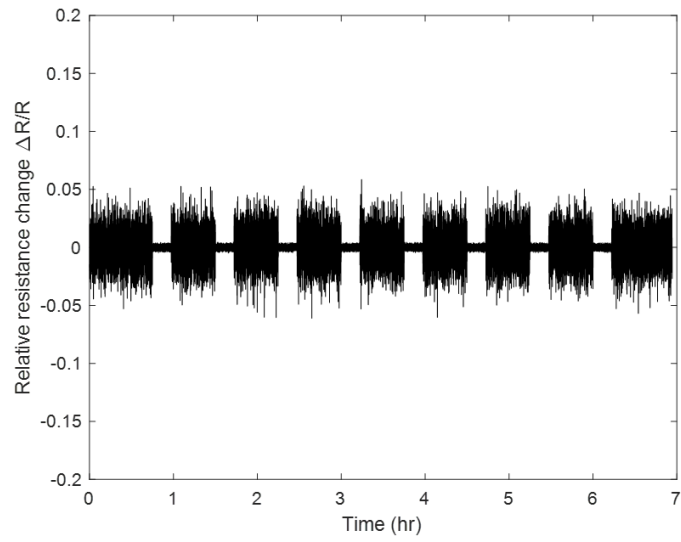


Figure 3.42. The life cycle evaluation test of vibration sensing

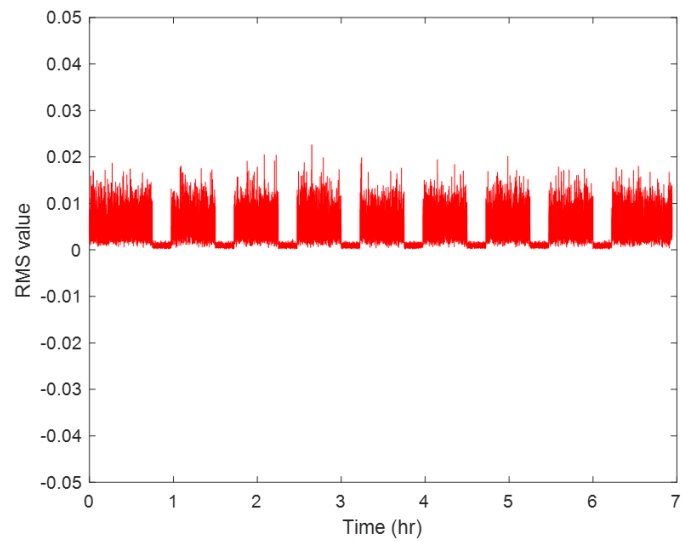


Figure 3.43. The RMS value of life cycle evaluation test of vibration sensing

Life cycle evaluation test for vibration sensing was also conducted similar to it of strain sensing. **Figures 3.42** and **3.43** show the relative resistance change and its RMS value of sensor signal during seven hours. According to **table 3.11**, the RMS value during life cycle evaluation test remains with small deviation value which demonstrates the robustness of printed sensor.

Table 3.11. The statistical analysis of RMS value of life cycle evaluation test

| Average | Deviation | Maximum | Minimum |
|---------|-----------|---------|---------|
| 0.0078 | 0.0024 | 0.0208 | 0.0050 |

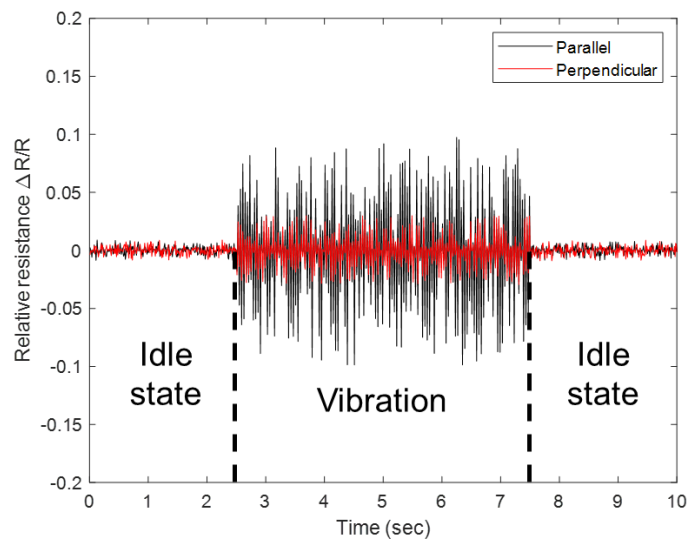


Figure 3.44. The relative resistance change by time according to vibration direction

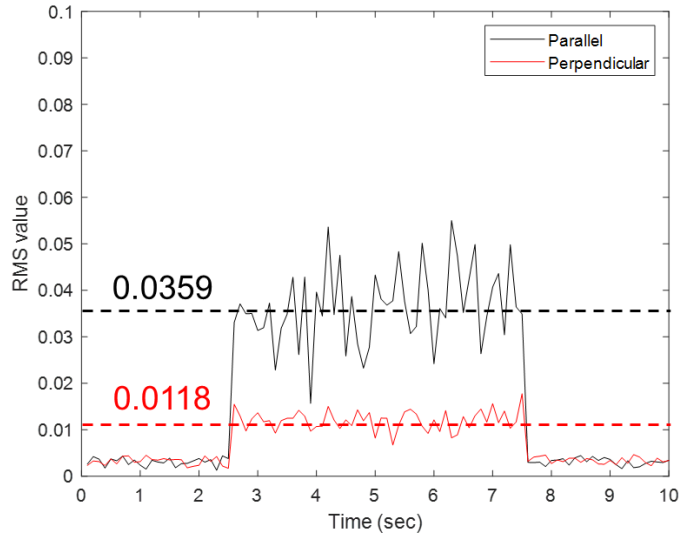


Figure 3.45. The RMS value of relative resistance change by time according to vibration direction

Figures 3.44 and **3.45** show the relative resistance and its RMS value of printed sensor according to vibration with parallel and perpendicular directions. The two relative resistance data with orthogonal direction exhibited similar trends without vibration while they showed the difference of peak value while vibration applied. According to the RMS value, sensor with parallel direction to applied vibration exhibited more than three times in comparison to sensor with perpendicular direction to applied vibration.

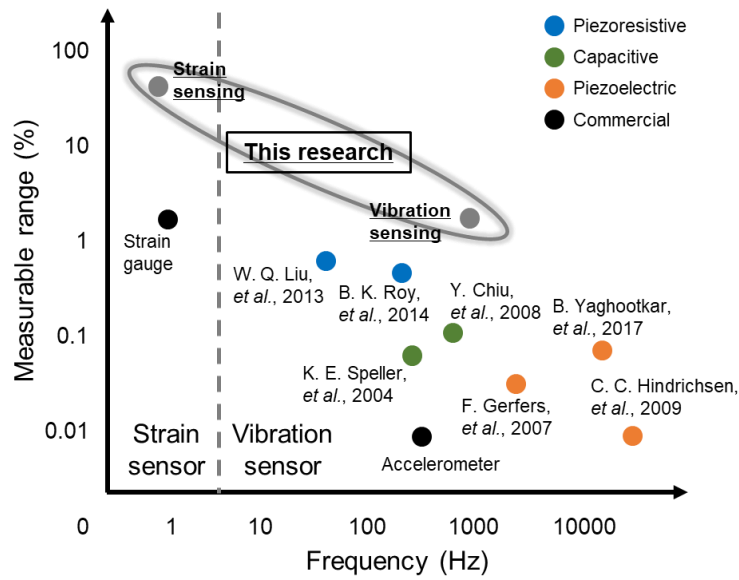


Figure 3.46. The results of this research according to frequency and measurable range in comparison to state-of-the-art

Figure 3.46 shows frequency and measurable range graph for fabricated sensor [83–88]. Electron tunnelling current between nanomaterials have enabled the vibration sensing with several hundreds of frequency which overcomes the technological limitations of piezoresistive sensor. Hence, it was verified that multivariate measurement of fabricated sensor was possible.

Furthermore, fabricated sensor exhibited the wide range in terms of gauge factor and maximum measurable frequency in comparison to previous interoperable sensor as shown in figure 3.47.

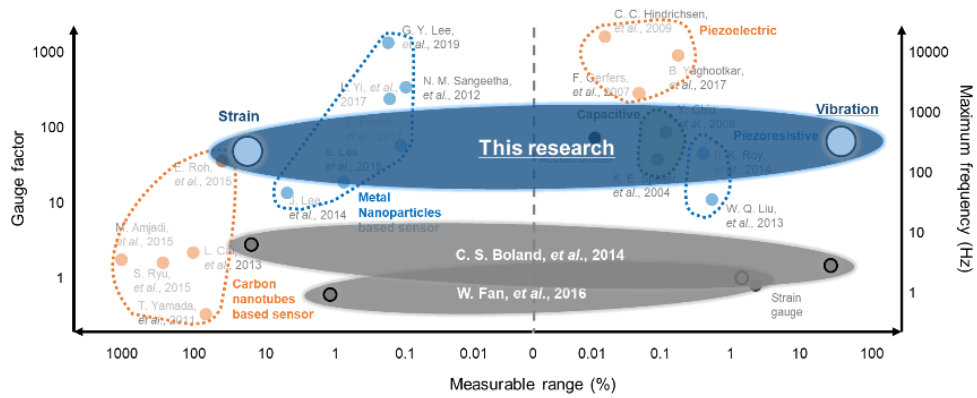


Figure 3.47. The results of this research in comparison to interoperable sensor

The results presented in this dissertation is expected to facilitate highly sensitive, wide measuring, and reliable measurements of structural dynamic behaviour and manufacturing process monitoring based on a cost-effective method that can leverage the future development of related technologies which will be discussed below.

3.3. Environmental and industrial evaluation

Figure 3.48 shows the XRD (X-ray diffraction) results for AgNPs based highly sensitive sensor. XRD measurement was conducted by powder X-ray diffractometry (D8 Advance, Bruker, Germany) with 435 mm circle diameter and angular range from -100° to 168° . XRD is the representative characterisation method for determining the atomic and molecular structure by using that structure causes a beam of incident X-rays to diffract into many specific directions [89]. Measurement showed the peaks of AgNPs which means that AgNPs were well directly printed onto substrate.

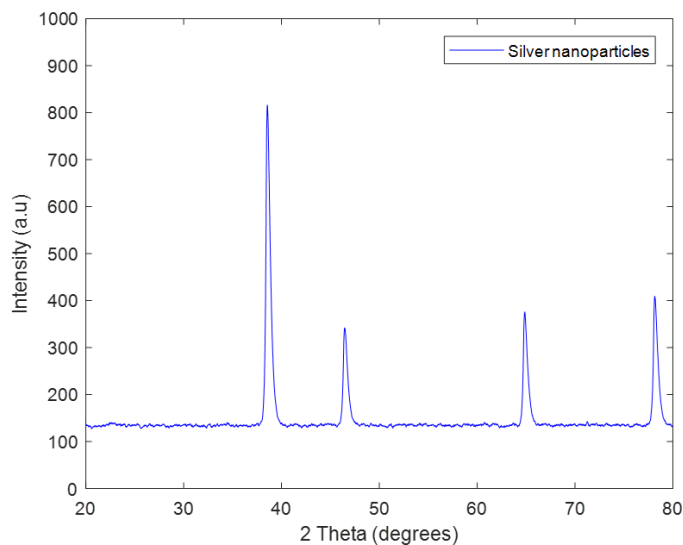


Figure 3.48. The XRD measurement results of highly sensitive sensor

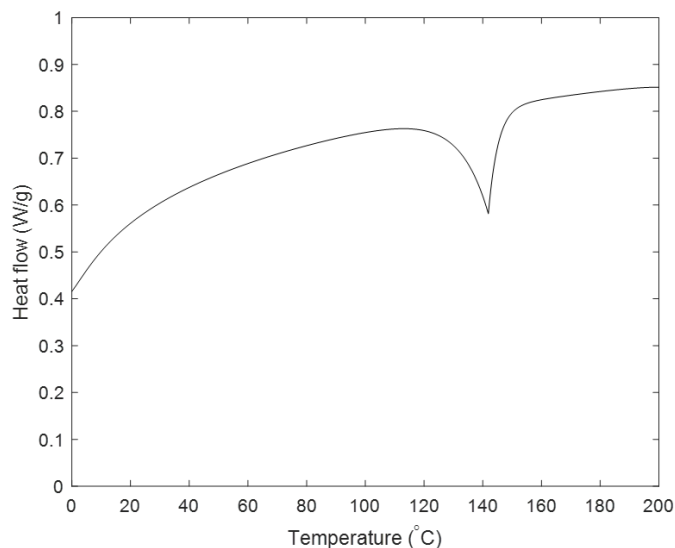


Figure 3.49. The DSC measurement results of highly sensitive sensor

Figure 3.49 shows the differential scanning calorimetry (DSC) results of highly sensitive sensor which was conducted by differential scanning calorimetry (Discovery DSC, TA Instrument, United States) with the temperature range from -80°C to 400°C . Since DSC measurement is a representative technique in which measures the difference in the amount of heat required to increase the temperature of a sample and reference, phase transition and structural change of sample materials could be configured [90]. According to measurement results, it was demonstrated that the sintering between AgNPs was occurred around 140°C which means that printed sensor could be utilised and showed reversible performance until sintering temperature.

Figure 3.50 shows the XRD results of highly sensitive and wide measuring sensor composed of AgNPs and MWCNTs. In comparison to AgNPs based sensor, peaks of CNTs were also exhibited in XRD results which represented that both AgNPs and MWCNTs were printed well onto PDMS substrate.

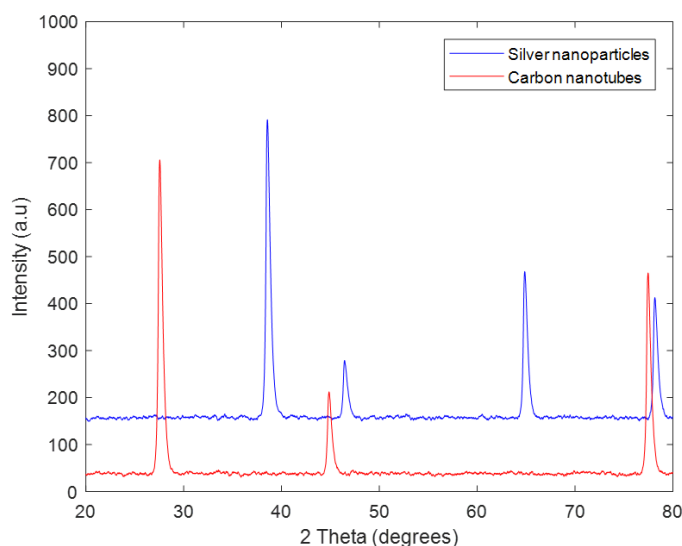


Figure 3.50. The XRD measurement results of highly sensitive and wide measuring sensor

The DSC results of highly sensitive and wide measuring sensor exhibited similar peaks to AgNPs sensor in the temperature range under 200 °C. This is due to the sintering effect was only occurred by AgNPs in given temperature range which means that printed sensor is expected to operable under sintering temperature. The sintering effect of CNTs occurred in much higher temperature that does not influence to operable range of printed sensor.

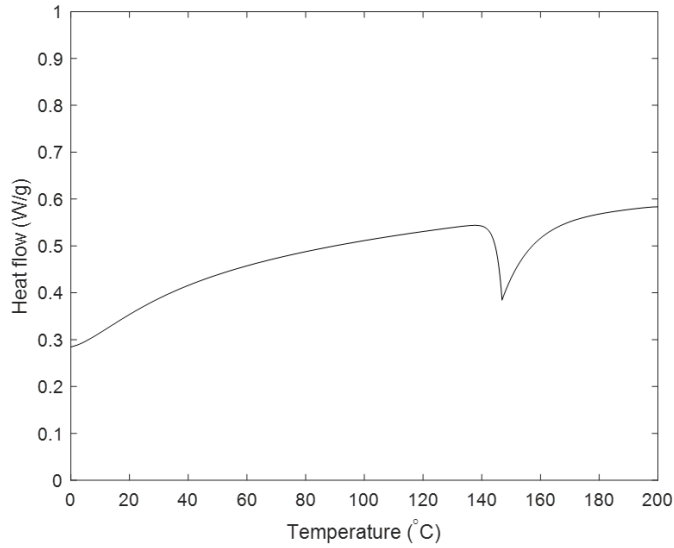


Figure 3.51. The DSC measurement results of highly sensitive and wide measuring sensor

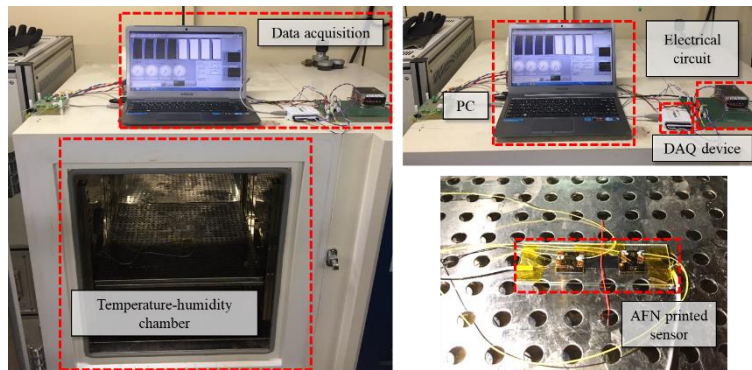


Figure 3.52. The photograph of experimental setup for temperature and humidity characterisation of AFN printed sensor

To analyse the change of resistance of AFN printed sensor according to temperature and humidity, respectively, experimental setup was constructed as shown in **figure 3.52**. The temperature – humidity chamber was utilised with data acquisition device (LabVIEW

2015 and NI USB 6009 modules, National Instruments, USA). The relative resistance change decreased until around 50 °C and increased after. The decrease of relative resistance could be explained by electron tunnelling effect which will be discussed below. The increase of relative resistance after 50 °C was well followed the original properties of AgNPs and MWCNTs in terms of thermal coefficient in both heating and cooling process. Hence, the reversibility of AFN printed sensor until sintering temperature was well verified.

Relative resistance also decreased by relative humidity of chamber. This was due to the increase of potential barrier between nanomaterials by water molecules in nanogaps which behaved as a huddle to the motion of electrons.

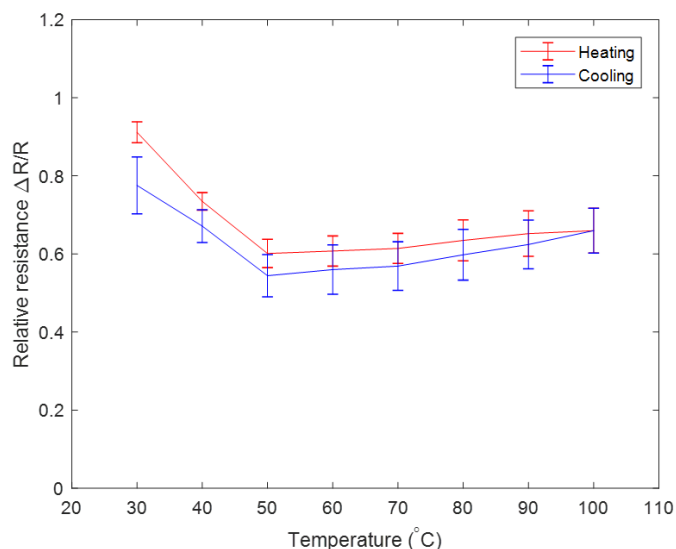


Figure 3.53. The measurement results of relative resistance of highly sensitive sensor according to temperature

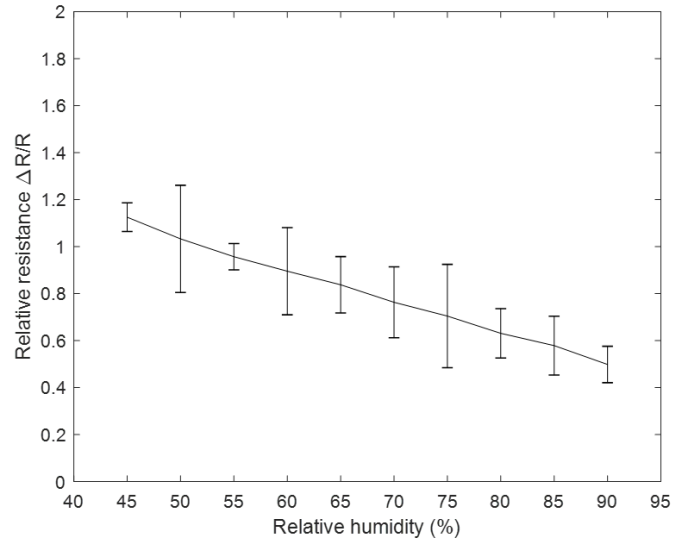


Figure 3.54. The measurement results of relative resistance of highly sensitive sensor according to relative humidity

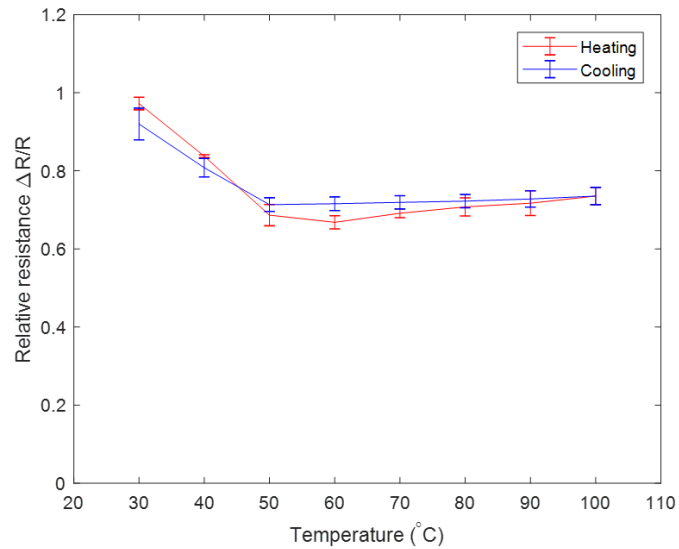


Figure 3.55. The measurement results of relative resistance of highly sensitive and wide measuring sensor according to temperature

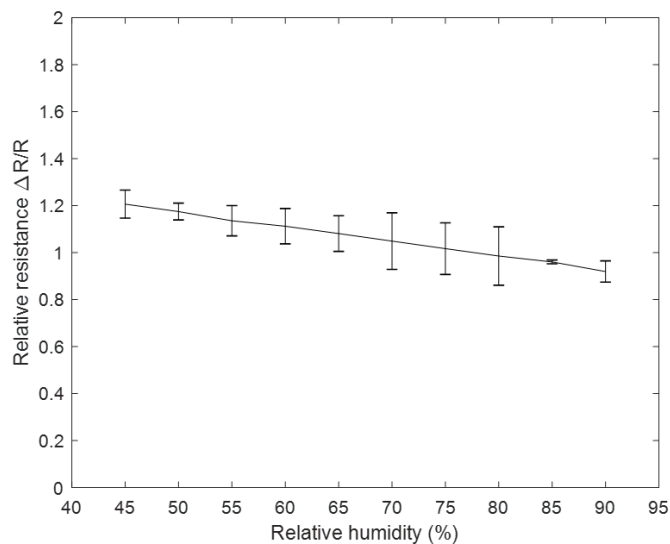


Figure 3.56. The measurement results of relative resistance of highly sensitive and wide measuring sensor according to relative humidity

However, the measurement results for temperature and humidity characterisation of highly sensitive and wide measuring sensor exhibited the less volatile behaviour in comparison to that of highly sensitive sensor as shown in **figures 3.55** and **3.56**. The relative resistance decreased less with respect to the temperature under 50 °C and increased less after 50 °C than AgNP based sensor. Furthermore, the relative resistance decreased less with respect to relative humidity than AgNP based sensor.

It was assumed that CNTs prevented sensitive properties of electron tunnel between NPs. Hence, it was demonstrated that highly sensitive and wide measuring sensor showed higher qualities than highly sensitive sensor also in environmental evaluation.

Table 3.12. The datasheet of fabricated sensor in comparison to commercial sensor

| Characteristics | Symbol | Units | Commercial sensor | Developed sensor |
|-------------------------|-------------|---------------|---------------------|--------------------|
| Supply voltage | V_s | V_{DC} | 5 | 5 |
| Supply current | I_o | mA_{DC} | 6 | 10 |
| Full scale span | R_{FSS} | Ω | 35 | 150 |
| Offset | R_{OFF} | Ω | 2 | 0.5 |
| Sensitivity | GF | — | 2.13 | 4.69 |
| Measurable range | — | % | 5 | 74 |
| Resolution | — | % | ± 0.1 | ± 0.5 |
| Hysteresis | — | % Ω | ± 0.1 | ± 1.1 |
| Temperature coefficient | TCR_{FSS} | % Ω /K | 11×10^{-6} | 7×10^{-5} |
| Input resistance | R_{in} | Ω | 120 ± 0.5 | 14 ± 0.1 |
| Response time | t_R | ms | 1.0 | 0.25 |
| Warm-up time | — | ms | 20 | 35 |
| Offset stability | — | % Ω | ± 0.5 | ± 0.5 |

Table 3.12 shows the datasheet of fabricated sensor in comparison to commercial sensor (Tokyo Sokki Kenkyujo Co., Japan). Fabricated sensor had advantages of sensitivity and measurable range with negligible difference of temperature coefficient in comparison to commercial sensor. Furthermore, in terms of the offset stability and response time, fabricated sensor showed the better performance than commercial sensor.

To evaluate the cost of fabricated sensor, cost-based pricing method was utilised. Cost-based pricing is the practice of setting prices based on the cost of the goods or services being sold. A profit percentage or fixed profit figure is added to the cost of an item, which results in the price at which it will be sold [91].

For accurate analysis, various accounts including materials cost, labour cost, equipment maintenance cost, equipment depreciation, promotion cost, and expected tax have been considered as shown in **table 3.13**. Materials costs of nanomaterial were only considered because no other materials was needed during AFN printing process, while legal productivity and minimum wage were calculated in the case of labour cost by taking into account the productivity of the sensor.

Table 3.13. Evaluation of cost of fabricated sensor according to cost-based pricing method

| Account | Estimated cost |
|------------------------|---|
| Materials cost | 5 USD per gram |
| Labour cost | 2,500 USD per capita (960 units per month) |
| Maintenance cost | 8,500 USD per month |
| Equipment depreciation | 2,800 USD per month |
| Promotion cost | 8,500 USD |
| Expected tax | + 20% |
| Total cost estimation | 2 USD per unit |

Based on the requirements of sensor for smart manufacturing with respect to SMEs as discussed above, fabricated sensor was evaluated as shown in **table 3.14**. The printed sensor was capable of strain and vibration measurement with low cost of two dollars per unit. Furthermore, since it was printed onto flexible and adhesive tape, it could be utilised by direct attachment on manufacturing equipment. Finally, the design or shape could be easily modified according to the desired applications by regulation of process parameters of AFN printing process.

Table 3.14. Evaluation of sensor based on low-cost smart sensor indicator for SMEs

| Sensor indicator | Evaluation |
|------------------|------------------------------|
| Essential | Strain, vibration measurable |
| Affordable | Two dollars per unit |
| Simple | Simply attachable |
| Interoperable | Easily design changeable |

Chapter 4. Sensing mechanism analysis

4.1. Theoretical background

Figure 4.1 shows schematic diagram of electron tunnelling effect between NPs. Electron tunnelling effects describe the current flow between the two electrodes if two electrodes are separated by a thin insulator. When two metallic electrodes are separated by an insulator, the equilibrium conditions require that the top of the energy gap of the insulator be positioned above Fermi level of the electrodes. Thus, the action of the insulator is to introduce a potential barrier between the electrodes which impedes the flow of electrons [92, 93].

The electronic current can flow through the insulation region between the two electrodes if the electrons in the electrodes have enough thermal energy to surmount the potential barrier and flow in the conduction band or the barrier is thin enough to permit its penetration by the electric tunnel effect.

The probability $D(E_x)$ that an electron can penetrate a potential barrier of height $V(x)$ is given by the well-known Wentzel-Kramers-Brillouin (WKB) approximation where $E_x = mv_x^2/2$, and is the energy component of the incident electron as shown in **equation 4.1**. The number of N_1 of electrons tunnelling through the barrier from electrode to other electrode is given by **equation 4.2** where E_m is the maximum energy of the electrons in the electrode, and $n(v_x)dv_x$ is the number of electrons per unit volume, respectively.

$$D(E_x) = \exp\left\{-\frac{4\pi}{h} \int_{s_1}^{s_2} [2m(V(x) - E_x)]^{1/2} dx\right\} \quad \text{Equation 4.1}$$

$$N_1 = \int_0^{v_m} v_x n(v_x) D(E_x) dv_x = \frac{1}{m} \int_0^{E_m} n(v_x) D(E_x) dE_x \quad \text{Equation 4.2}$$

By calculating N_2 in a similar manner, the net flow of electrons N through the barrier and the current density were calculated as below.

$$N = \int_0^{E_m} D(E_x) dE_x \left\{ \frac{4\pi m^2}{h^3} \int_0^\infty [f(E) - f(E + eV)] dE_r \right\} \quad \text{Equation 4.3}$$

$$J \cong \exp(-\beta(s_2 - s_1)) \quad \text{Equation 4.4}$$

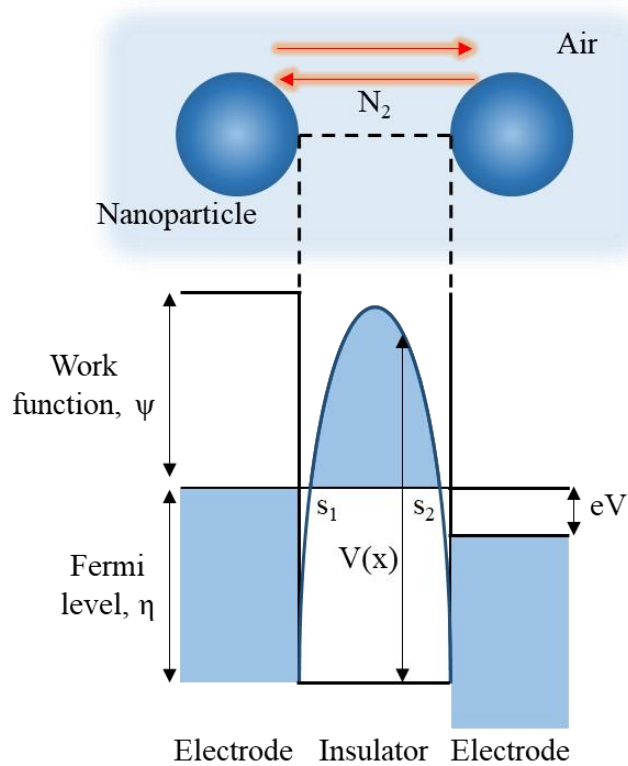


Figure 4.1. The schematic diagram of electron tunnelling effect between NPs

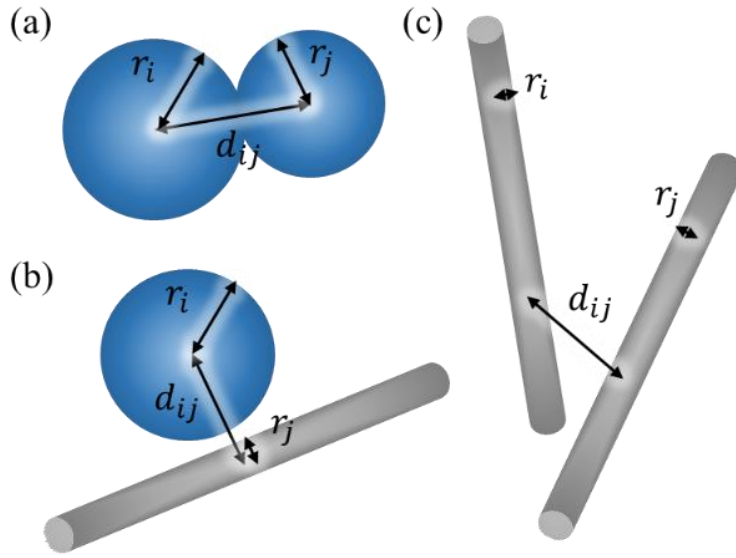


Figure 4.2. The schematic diagram of mechanical attachment between (a) NPs, (b) NP and CNT, and (c) CNTs

The distance between nanomaterials d_{ij} for nanomaterial i and j could be calculated by the distance between the centres of two NPs, perpendicular distance between the centres of the NP and the CNT, and the minimum distance between two CNTs as shown in **figure 4.2** for further study.

For molecular vibration, induced vibration generate the electron voltage according to frequency in perspective of quantum mechanics as shown in **equation 4.5**. Hence, total change of electrical conductance of fabricated sensor could be calculated as total sum of change of each nanomaterial.

$$eV = hf$$

Equation 4.5

$$V = Nn_e hf$$

Equation 4.6

However, the number of nanomaterials in sensor was assumed as $N \sim 10^7$, and the number of electrons in each nanomaterial was assumed as $n_e \sim 10^3$, which means that molecular vibration could be negligible in this dissertation.

4.2. Statistical regression analysis

Since the net flow of electrons are exponentially and inversely proportional to the distance between electrodes as shown in **equation 4.4**, it was possible to assume that the electron tunnelling effect is only occurred when electrodes are mechanically attached each other in large strain condition [94]. In this perspective, the electrical conductivity between nanomaterials could be calculated as shown in **equations 4.5 and 4.6**.

$$\sigma_{ij} = \delta_{ij}\sigma \quad \text{Equation 4.7}$$

$$\delta_{ij} = \begin{cases} 1 & \text{if } d_{ij} \leq r_i + r_j \\ 0 & \text{if } d_{ij} > r_i + r_j \end{cases} \quad \text{Equation 4.8}$$

In other words, electrical conduction is only existed when nanomaterials are attached each other. As shown in **equations 4.7 and 4.8**, an attachment indicator δ_{ij} was defined where d_{ij} , r_i , and r_j represent the distance between nanomaterials, radius of nanomaterials i and j, respectively.

To analyse the strain sensing performance, understanding detachment between AgNPs and MWCNTs by strain increase is important. Here, models were derived for highly sensitive and wide measuring sensor using probit model. Probit model is a conventional regression model for independent variable with binary value, usually zero or one [95, 96]. Here, nanomaterial could have one of two states,

one is attached each other and the other is detached, which represents electrical connection and disconnection, respectively. In this dissertation, bivariate probit model was used for analysis of AgNP/MWCNT nanocomposite, each variable represents one substance where σ_{pp} is a variable for electrical conductivity among AgNPs by their electrical state and σ_{pt} is electrical conductivity between AgNPs and MWCNTs as shown in **equations 4.9** and **4.10**.

$$\sigma_{pp} = \sigma_{NP} \begin{cases} 1, & \text{if } NPs \text{ attached } (\sigma'_{pp} < 0) \\ 0, & \text{if } NPs \text{ detached } (\sigma'_{pp} > 0) \end{cases} \quad \text{Equation 4.9}$$

$$\sigma_{pt} = \sigma_{NPCNT} \begin{cases} 1, & \text{if } NP/CNT \text{ attached } (\sigma'_{pt} < 0) \\ 0, & \text{if } NP/CNT \text{ detached } (\sigma'_{pt} > 0) \end{cases} \quad \text{Equation 4.10}$$

Nanomaterials were detached when induced strain exceeded a specific strain value. For analyses, the latent variables σ'_{pp} and σ'_{pt} were also denoted for convenience. They were dependent variable for induced strain ε and materials properties which represented as shown in **equations 4.11** and **4.12** where e_1 and e_2 are standard error.

$$\sigma'_{pp} = \beta_{pp1} + \beta_{pp2}\varepsilon + e_1 \quad \text{Equation 4.11}$$

$$\sigma'_{pt} = \beta_{pt1} + \beta_{pt2}\varepsilon + e_2 \quad \text{Equation 4.12}$$

Fitting the bivariate probit model involves estimating the values of β_{pp1} , β_{pp2} , β_{pt1} , and β_{pt2} . Using experimental values, certain beta

values β_{pp1} , β_{pp2} , β_{pt1} , and β_{pt2} could be found which maximise the likelihood of the model given by experimental value. Likelihood of this model L is represented as shown in **equation 4.13**.

$$L = \prod P(\sigma_{pp} = 1, \sigma_{pt} = 1)^{\sigma_{pp}\sigma_{pt}} P(\sigma_{pp} = 0, \sigma_{pt} = 1)^{(1-\sigma_{pp})\sigma_{pt}} P(\sigma_{pp} = 1, \sigma_{pt} = 0)^{\sigma_{pp}(1-\sigma_{pt})} P(\sigma_{pp} = 0, \sigma_{pt} = 0)^{(1-\sigma_{pp})(1-\sigma_{pt})}$$

Equation 4.13

By minimising mean squared error for above likelihood, β_{pp1} , β_{pp2} , β_{pt1} , and β_{pt2} could be calculated. **Figure 4.3** shows that introduced model with probit regression well explained strain sensing performance. Single beta value could explained all behaviours of empirical values with respect to composition ratio of nanocomposite.

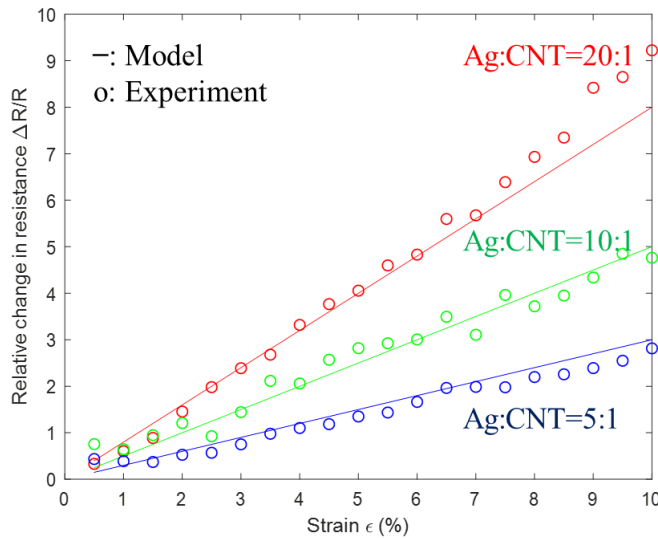


Figure 4.3. The validation of model by comparison of model value to experimental value with respect to composition ratio of AgNPs and MWCNTs

4.3. Monte Carlo simulation

The performance of sensors is largely influenced by the geometrical properties of nanomaterial which is varied according to the synthesis method of nanomaterial. The geometrical properties include not only the diameter and length of each NP and CNT, but also how homogeneous they are. Therefore, there have been several efforts to numerically simulate the behaviour of NPs in dynamic condition. Several simulation methods for metal NPs based strain sensor have been introduced using Monte Carlo method [97–102]. They have been usually for analysis of highly sensitive properties of NPs based strain sensor or physical explanation of electron behaviour in gaps between NPs. Otherwise, several simulation methods for nanocomposite have also been introduced. These contributions have mostly dealt with analysis of behaviour of NPs decorated CNTs or explanation of nanocomposite fabrication methods. However, simulation methods of electrical properties changed by strain for nanocomposite have not been achieved using existing simulation methods [103–107]. This is mainly due to a high simulation cost and inaccuracies of the result for electrical conductivity calculation of nanocomposite using above methods.

In this dissertation, simple simulation method for estimation of the electrical properties change of nanocomposite according to mechanical strain by simply counting the electrical attachment of AgNPs and MWCNTs have been proposed. Since electrical

conductivity is directly influenced by mechanical attachment among nanomaterials, average attachment of nanomaterials by strain was calculated using the voter model which is a widely used model for analysis of particle interactions. Each NP or CNT was assumed as each agent in the voter model, which can have one of two opinions. The opinion of each nanomaterial changes to another opinion continuously with time step when it is encountered with another nanomaterial. It was assumed that each nanomaterial has one of the states, attached to or separated from each other by applying the voter model. Then, the simulation results were compared to experimental results of fabricated sensors with various composition ratio and packing ratio for validation of suggested simulation method. Using the suggested simulation method, the accurate electrical conductivity value was obtained in comparison to actual experimental results with low simulation cost.

The reliability of computational model is important factor for the accurate simulation. Since this dissertation was mainly focused on the interaction between nanomaterials which is approximately from several tens of nanometers to several hundreds of nanometers, it was appropriate to employ Lennard–Jones (LJ) potential model. LJ potential model has its advantages in terms of simulation time in comparison to density functional theory or other quantum–mechanical methods [108–111]. Furthermore, LJ potential model have widely been used to approximate the interaction between a pair of neutral atoms or molecules for substantially larger systems.

$$\Phi_{ij}(r_{ij}) = \varepsilon_{0,ij} \left[\left(\frac{r_{0,ij}}{r_{ij}} \right)^{12} - \left(\frac{r_{0,ij}}{r_{ij}} \right)^6 \right] \quad \text{Equation 4.14}$$

For each nanomaterial i and j , LJ potential Φ_{ij} is denoted in **equation 4.14** where ε_0 is the depth of potential well or equilibrium nonbond energy, r_0 is the equilibrium nonbond distance between the particles, and r_{ij} is the distance between the nanomaterial. It is usually used by only two parameters ε_0 and r_0 which are physically represent the density and the surface free energy. Hence, LJ potential model is not appropriate in high temperature condition including melting and boiling of nanomaterial. In this dissertation, it was assumed that surface and interface temperature of nanomaterial is under ambient temperature range. The density and the surface free energy were calibrated using experimental values, which were derived from above discussions. Moreover, the total energy for simulation domain was calculated by sum of each LJ potential among AgNPs, between AgNPs and CNTs, and among CNTs.

Here, it was assumed that nanomaterial can have one of two states, one is attached and the other is detached, which represent electrical connection and disconnection, respectively. Furthermore, each state of nanomaterial was stochastically distributed within boundary conditions according to external strain. Hence, the voter model was proposed to explain the behaviour of electrical conductivity of nanocomposite sensor. The voter model is a sequential dynamical system based on Markov process for interacting

particle system [112–114]. In the voter model, each node of graph is endowed with two states usually zero or one which is very similar to our conditions. First, model chose a random voter and it adopted the state of a randomly chosen neighbour. These steps were repeated until a finite system necessarily reached consensus. Here, transition rate was defined using transition probabilities \mathbf{p} and Markov process η for an irreducible random walk as shown in **equation 4.15**.

$$c(x, \eta) = \begin{cases} \sum_y p(x, y) \eta(y) & \text{for all } \eta(x) = 0 \\ \sum_y p(x, y) (1 - \eta(y)) & \text{for all } \eta(x) = 1 \end{cases} \quad \text{Equation 4.15}$$

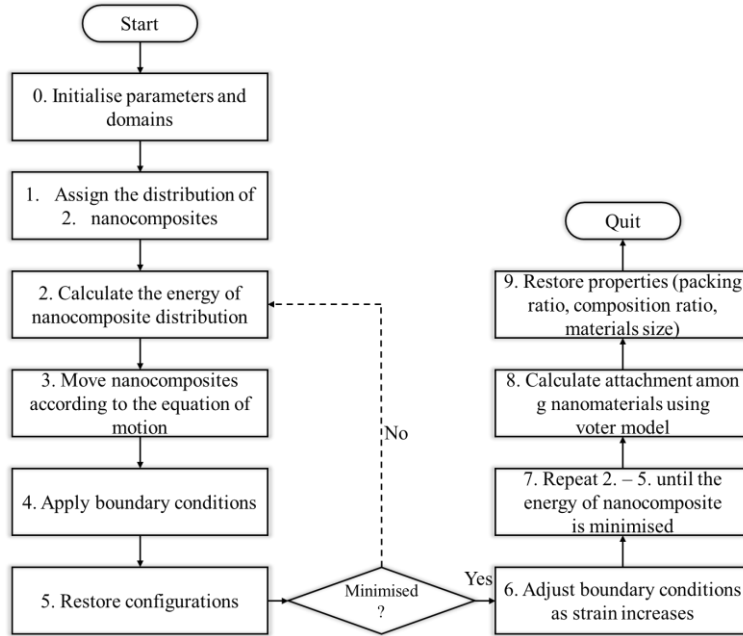


Figure 4.4. The flowchart of Monte Carlo simulation method for electrical conductivity calculation of nanocomposite

Figure 4.4 shows the overall flowchart for proposed simulation method based on Monte Carlo method. First, the simulated region and the coordinates of the physical spaces were defined and the parameters for nanomaterial and model were initialised, respectively. After initialisation, distribution of AgNPs and CNTs were randomly assigned. Then, the energy of nanocomposite distribution was calculated and nanocomposite were moved according to the equation of motion in boundary conditions until the energy was minimised. The distribution with minimised LJ potential was assumed to the distribution of printed nanocomposite sensor. Based on minimised distribution of nanocomposite sensor, process was repeated by adjustment of boundary conditions as strain increased. After the boundary condition was fixed to desired strain value, the attachment among nanomaterials was calculated using voter model. Finally, other properties including packing ratio and composition ratio were also restored. All simulations were implemented in C++ and results were displayed by MATLAB.

Table 4.1 shows simulation parameters used for this dissertation. Three parameters were used including the diameter of AgNP, the diameter of CNT, and the length of CNT to analyse the effect of nanomaterial geometry. Since homogeneity of nanomaterials was also an important factor of nanomaterials quality, not only the average value of each parameters but also the standard deviation value of each parameters were used. In general, it is difficult for all the nanomaterials to be fabricated exactly in the desired size in

nanomaterials synthesis and manufacturing process. Therefore, the homogeneity of nanomaterials is an important indicator for the quality of the nanomaterials. For each parameter value, five values were used which were spaced at equal intervals based on the actual values of the nanomaterials actually available. All parameters were determined within the valid range of models including LJ potential model and the voter model. Experimental values derived from above discussions were used as median value of each parameters. All the other variables were fixed according to normal distribution when simulation was conducted for one parameter and all simulations were repeated for three times for reliability of results as shown in **table 4.2**.

Table 4.1. The geometrical properties of nanomaterial used for Monte Carlo simulation method

| Diameter of AgNP (nm) | | Diameter of MWCNT (nm) | | Length of MWCNT (nm) | |
|-----------------------|--------------------|------------------------|--------------------|----------------------|--------------------|
| Average | Standard deviation | Average | Standard deviation | Average | Standard deviation |
| 25 | 5 | 8 | 2 | 600 | 100 |
| 50 | 10 | 10 | 3 | 800 | 150 |
| 75 | 15 | 12 | 4 | 1,000 | 200 |
| 100 | 20 | 14 | 5 | 1,200 | 250 |
| 125 | 25 | 16 | 6 | 1,400 | 300 |

Table 4.2. The simulation parameter used for Monte Carlo simulation method

| Average | Material | Units | Value | Note |
|-------------------------|---------------------|---------------------------|-------------------------|-----------|
| Electrical conductivity | Silver nanoparticle | $1/\mu\Omega\text{cm}$ | 0.628931 | At 20 ° C |
| | Carbon nanotube | | 0.005593 | |
| Density | Silver nanoparticle | $\mu\text{g}/\text{nm}^3$ | 1.049×10^{-14} | |
| | Carbon nanotube | | 2.1×10^{-15} | |
| Domain | Length | nm | 1,000 | |
| | Width | | 500 | |
| | Height | | 500 | |

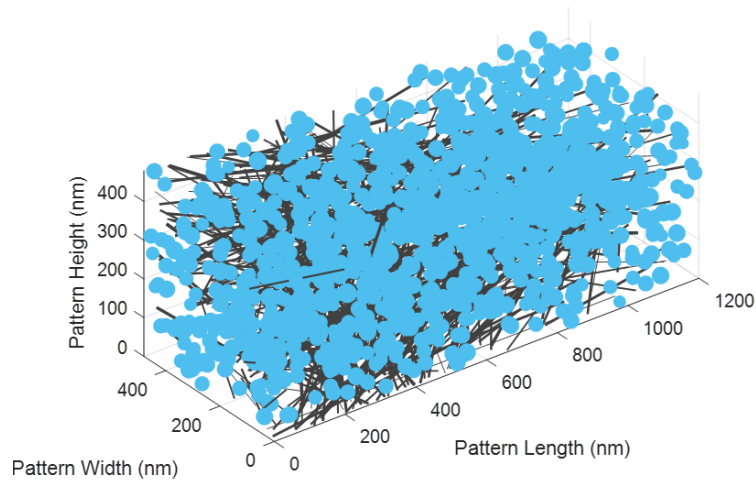


Figure 4.5. The optimised distribution of nanocomposite simulation domain with minimised energy

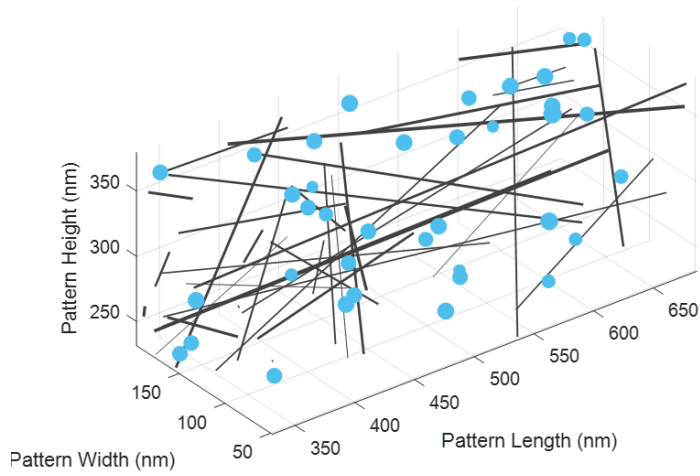


Figure 4.6. A magnified view of optimised nanocomposite distribution with minimised energy

The distribution of AgNPs and MWCNTs were optimised as shown in **figure 4.5**. The optimisation was repeated 1,000 times until the LJ potential was minimised while slightly moving the nanomaterial. It was assumed that the distribution of nanomaterials was almost similar to the actual distribution of AFN printed pattern. **Figure 4.6** shows the magnified view for nanomaterials distribution which was optimised in **figure 4.5**. It was shown that some of nanomaterial were attached to each other and some were separated from each other. For an accurate calculation, it was defined to mechanically attached each other if the distance between the centre of two nanomaterial was less than the sum of the radius of two nanomaterial.

Figure 4.7 shows the probability distribution of AgNPs according to diameter and **figures 4.8** and **4.9** show the probability distribution of MWCNTs according to diameter and length, respectively. The geometrical properties of nanomaterials including AgNPs and MWCNTs were randomly assigned within the normal distribution while maintaining the average and standard deviation values of distribution.

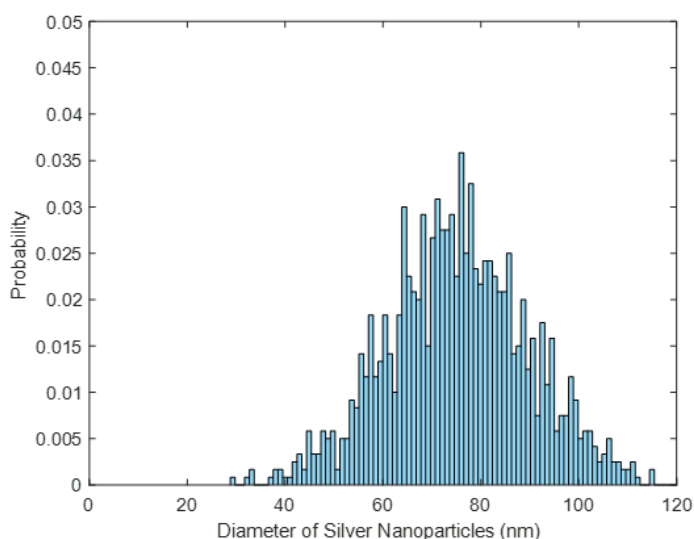


Figure 4.7. The distribution of simulated AgNPs according to diameter

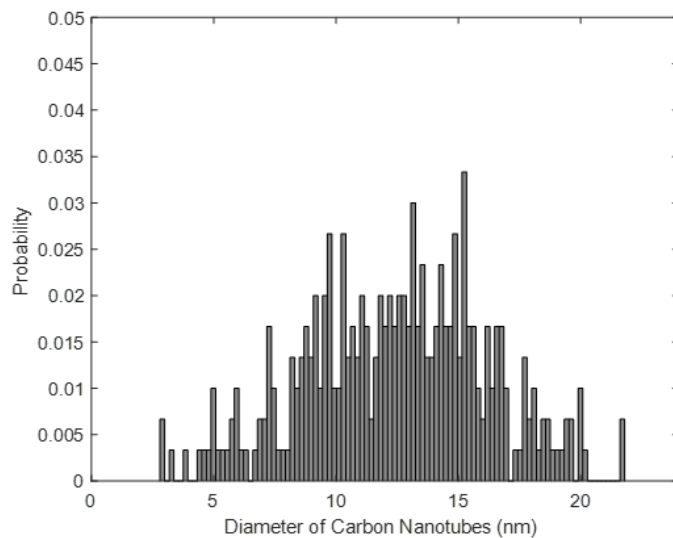


Figure 4.8. The distribution of simulated CNTs according to diameter

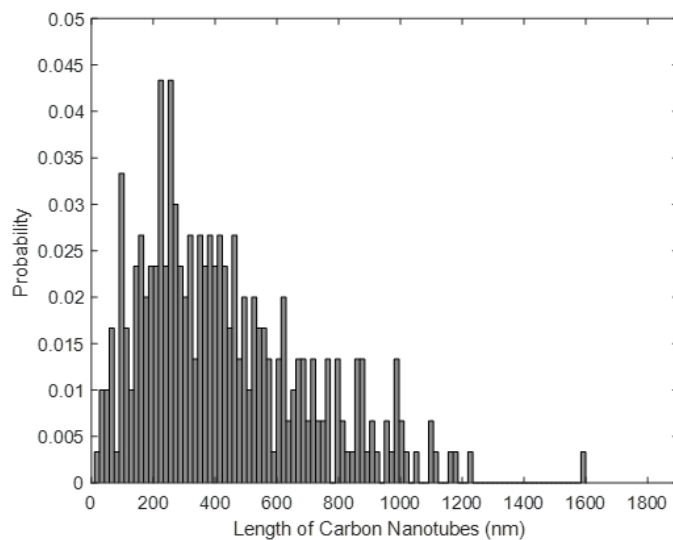


Figure 4.9. The distribution of simulated CNTs according to length

Figures 4.10 and 4.11 show the simulation results for average electrical attachment by strain for various composition ratio and packing ratio of nanocomposite, respectively. A composition ratio and packing ratio were primary indicators for properties of nanocomposite sensor, which can control sensitivity and stretchability both as discussed above. Since the number of attachment was different for each nanomaterial, the average value of nanomaterial attachment was used. In addition, the average electrical attachment \bar{A}_e was calculated as equation 4.16, because of the different effects of NPs attachment $\bar{A}_{e,NP}$ and CNTs attachment $\bar{A}_{e,CNT}$ on the electrical properties of the sensor.

$$\bar{A}_e = \sigma_{NP}\bar{A}_{e,NP} + \sigma_{NP-CNT}\bar{A}_{e,NP-CNT} + \sigma_{CNT}\bar{A}_{e,CNT} \quad \text{Equation 4.16}$$

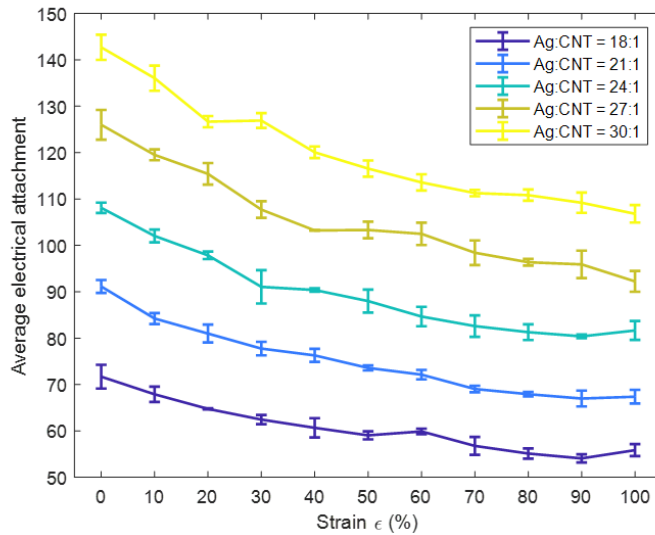


Figure 4.10. The simulation results of average electrical attachment with various composition ratio of nanocomposite according to strain

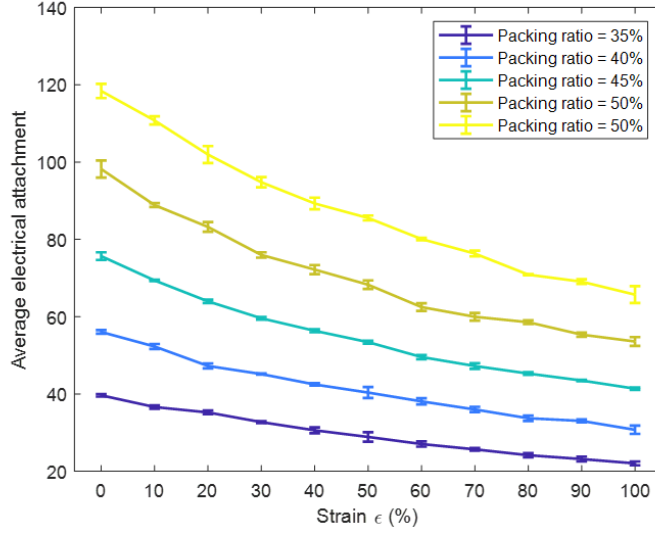


Figure 4.11. The simulation results of average electrical attachment with various packing ratio of nanocomposite according to strain

The \bar{A}_e decreased as the strain increased in all results. It was due to the increase of boundary condition in the strain direction which enabled the nanomaterials to be distributed in a larger space. Moreover, \bar{A}_e increased as the relative mass of AgNPs to MWCNTs increased because NPs were usually attached to each other as compared to CNTs. In general, $\bar{A}_{e,NP}$ was five to ten times larger than $\bar{A}_{e,CNT}$ in most simulations. In terms of packing ratio, \bar{A}_e also increased as the packing ratio increased which means that nanomaterials were more dense in the same space. However, the more important factor of sensor performance in terms of sensitivity was not the absolute value of \bar{A}_e but the change of \bar{A}_e by strain.

To compare the with change of \bar{A}_e to GF, the change of electrical conductivity $\Delta\sigma$ by strain was defined similar to the definition of GF as shown in **equation 4.17**.

$$\Delta\sigma = \frac{\bar{A}_{e,i} - \bar{A}_{e,f}}{\Delta\varepsilon\bar{A}_{e,i}} \quad \text{Equation 4.17}$$

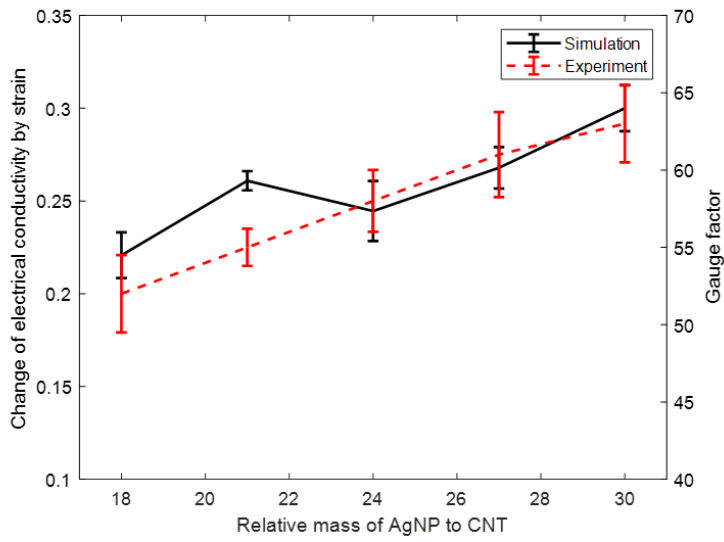


Figure 4.12. Comparison of simulation results of change of electrical conductivity by strain to experimental values of GF by composition ratio

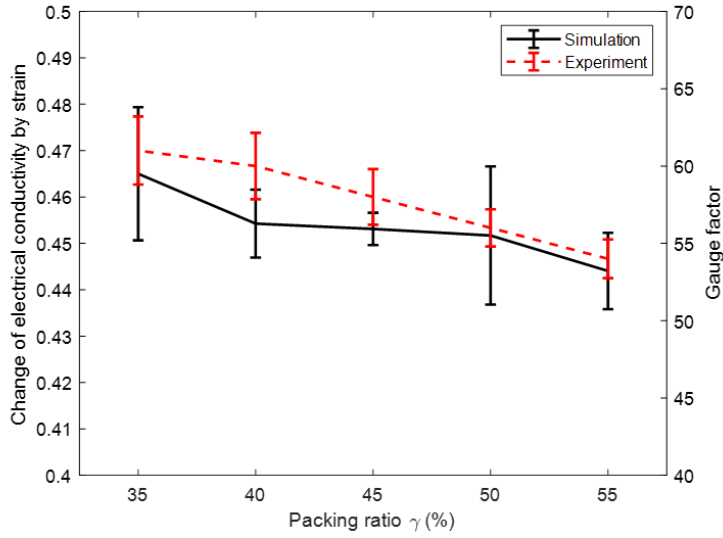


Figure 4.13. Comparison of simulation results of change of electrical conductivity by strain to experimental values of GF by packing ratio

Since it used the variation of the average electrical attachment according to the strain, the dynamical situations of nanocomposite sensor could be considered. As shown in **figure 4.12**, GF increased as the relative mass of AgNPs to MWCNTs increased. In terms of packing ratio, since the close distance between nanocomposite prevented themselves from falling apart, high packing ratio decreased GF as shown in **figure 4.13**. According to similar behaviour of simulated values and experimental values, the developed simulation method using the experimental value was experimentally validated with various composition ratio and packing ratio.

Table 4.3. Characteristics and limitations of suggested model in comparison to other simulation method

| Model | Characteristics | Limitations |
|------------------------------|---|---|
| Contact resistance | Apply classic conductivity models to single nanomaterial | Difficult to use in large deformation condition |
| Boltzmann transport equation | Consider probability distribution for the position and momentum | High simulation cost for composite structure |
| Electron tunnelling | Charge-injection current by tunnel through the barrier | Suitable for the application of single nanomaterial |
| Electrical attachment | Count mechanical attachment among nanomaterials | Need to aware the physical situation in advance |

It is difficult to obtain highly accurate results by using the contact resistance model for calculating electrical conductivity of nanomaterial. Furthermore, the simulation could only be performed within a limited range to which the classic model could be applied. Hence, several models based on quantum mechanics have been proposed for the accuracy of the simulations for nanomaterials as shown in **table 4.3**. Boltzmann transport equation is a widely used model for analysis of the change of a macroscopic quantity in terms of energy. However, it has the disadvantage of being suitable for interpreting a single kind of nanomaterial due to the need to define

momentum for each nanomaterial.

The electron tunnelling model is also a well-known model for describing the transfer of electrons between nanomaterials, but it has the disadvantage of high simulation cost if the number of nanomaterial to be analysed is large. The simulation method represented in this dissertation was appropriate for calculation of the electrical conductivity at a low simulation cost under the defined mechanical deformation conditions of the structure. In addition, the simulation cost of this method did not increase drastically according to the increase of the number of nanomaterial or the variation of geometrical distribution.

Likewise, vibration sensing analysis based on developed Monte Carlo simulation method was conducted. **Figure 4.14** shows the overall flowchart for proposed simulation for vibration sensing mechanism analysis. The simulated region and the coordinates which is assigned to minimise LJ potential were used as discussed above. Then, vibration was applied to each unfixed nanomaterial randomly according to given amplitude and frequency. Unfixed nanomaterial was defined as nanomaterial that were not attached more than two other nanomaterials. Using the behaviour that current density is inversely proportional to the distance between nanomaterials, current density for fabricated sensor was calculated by the total sum of each current density between nanomaterials.

For the analysis of simulation, electric current density between two nanomaterials was calculated as shown in **equation 4.18**. Then, the tunnelling current of sensor was estimated to the total sum of each tunnelling current as shown in **equation 4.19**. Finally, the relative resistance change was calculated by comparison of tunnelling current before and after the distance change as shown in **equation 4.20**.

$$J_{ij} = \exp(-\beta_{ij}d_{ij}) \quad \text{Equation 4.18}$$

$$J = \sum_{i>j} J_{ij} \quad \text{Equation 4.19}$$

$$\frac{\Delta R}{R} = \frac{J_{init} - J_{final}}{J_{final}} \quad \text{Equation 4.20}$$

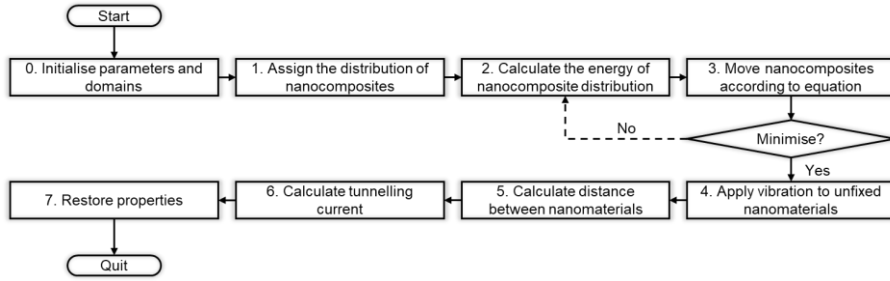


Figure 4.14. The flowchart of Monte Carlo simulation method for vibration sensing of nanocomposite

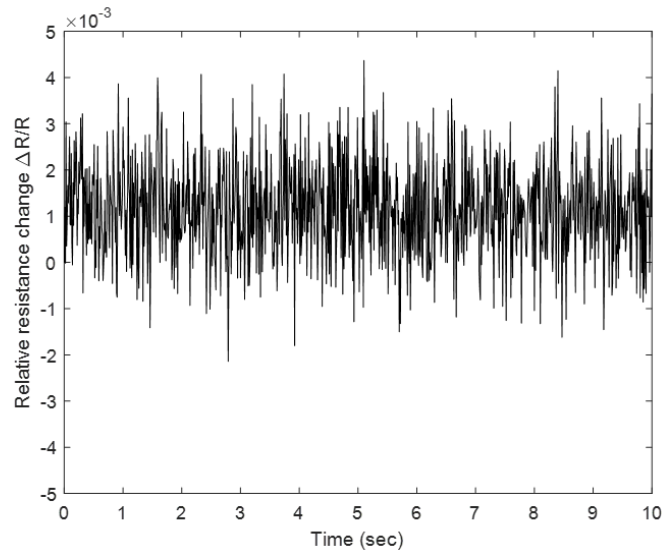


Figure 4.15. The simulation results of relative resistance change at vibration with 100 Hz

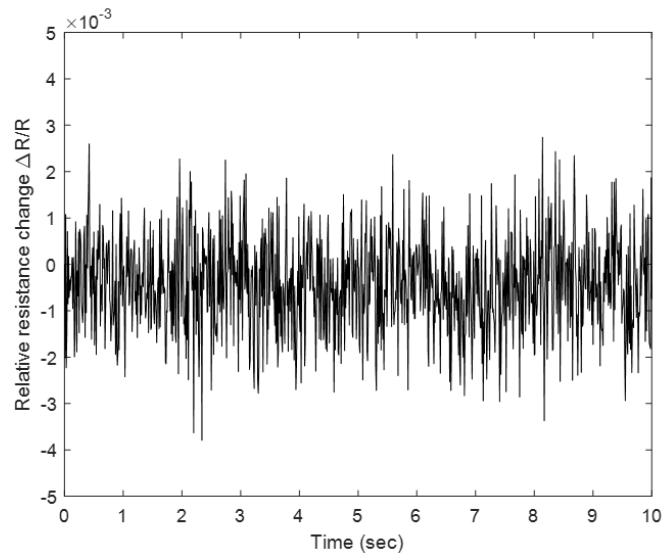


Figure 4.16. The simulation results of relative resistance change at vibration with 200 Hz

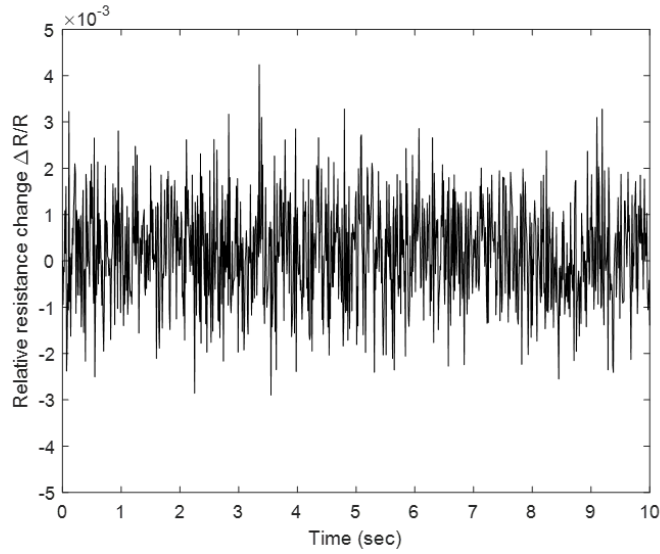


Figure 4.17. The simulation results of relative resistance change at vibration with 400 Hz

Figures 4.15–4.17 show the simulation results of relative resistance change at vibration with 100, 200, and 400 Hz, respectively. The results exhibited the periodic signal of relative resistance change according to vibration. Furthermore, the frequency of each data has increased as increase of induced vibration frequency. It was estimated that the distance between the fixed and unfixed nanomaterial rapidly changes with increasing frequency, causing a rapid change in resistance.

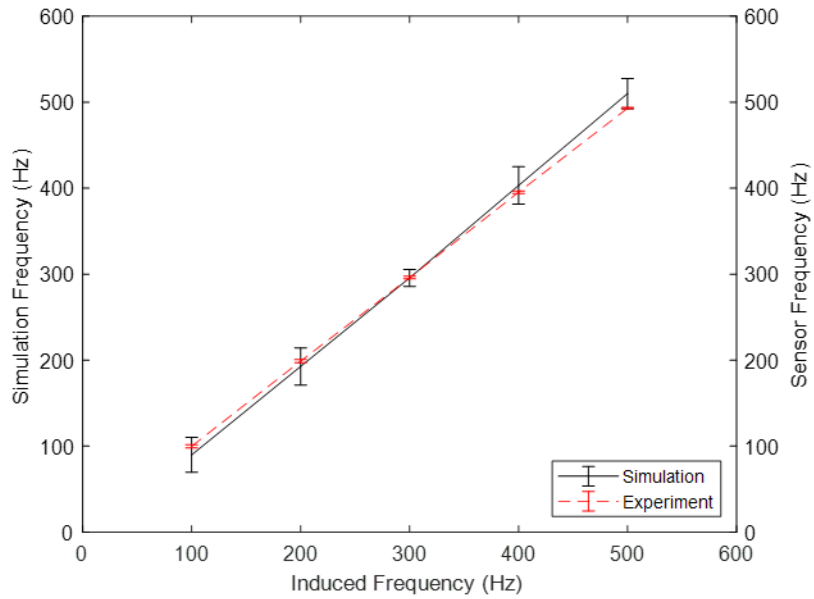


Figure 4.18. Comparison of simulation results of frequency to experimental values by induced frequency

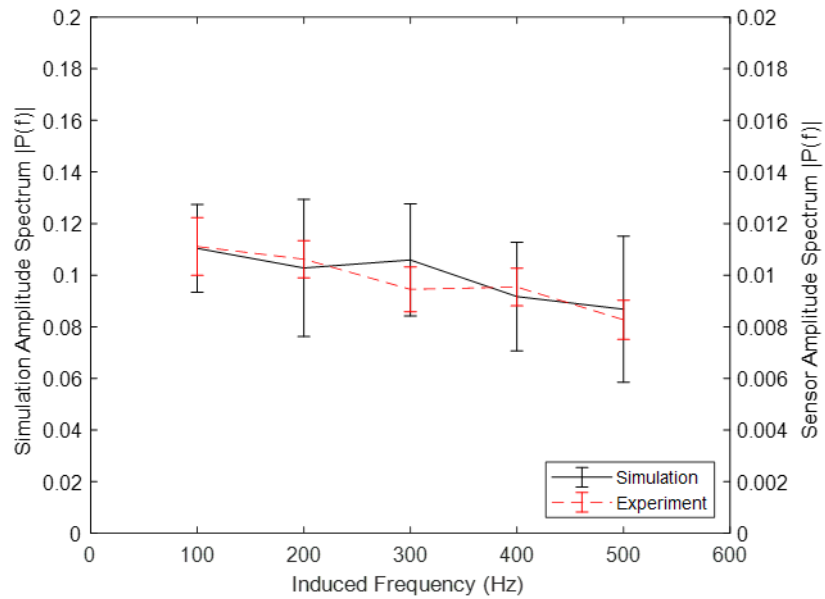


Figure 4.19. Comparison of simulation results of amplitude spectrum to experimental values by induced frequency

Figures 4.18 and 4.19 show the comparison of simulation results to experimental results in respective to induced frequency. The simulation results showed similar behaviour to experimental values while increasing with the induced frequency. The simulated amplitude spectrum and the experimental values gradually decreased with the applied frequency. It was demonstrated that the intensity of vibration itself decreased with the frequency of vibration even if with the same vibration amplitude.

The simulation and experiments were conducted with different amplitudes of the identical vibration frequency as shown in **figures 4.20 and 4.21**. Likewise, the simulation and the experimental values showed similar patterns. The frequency did not change according to induced amplitude while spectrum increased with the amplitude.

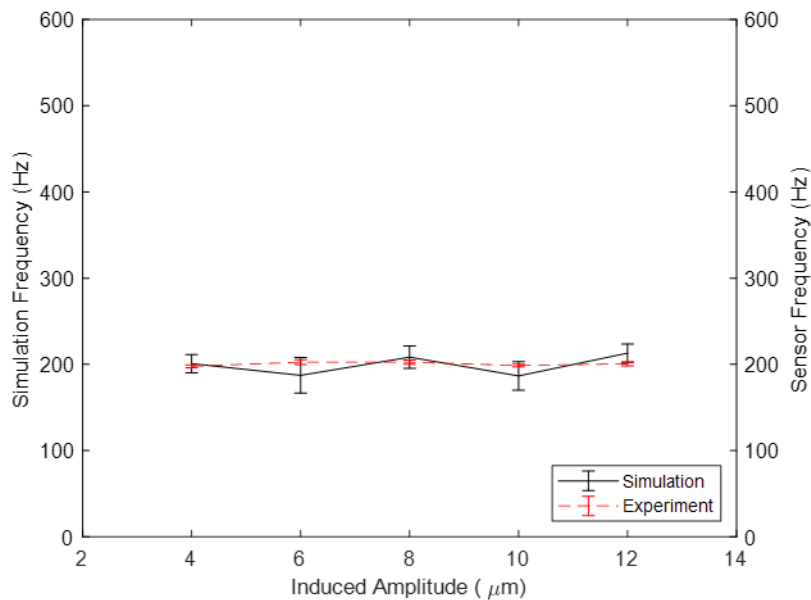


Figure 4.20. Comparison of simulation results of frequency to experimental values by induced amplitude

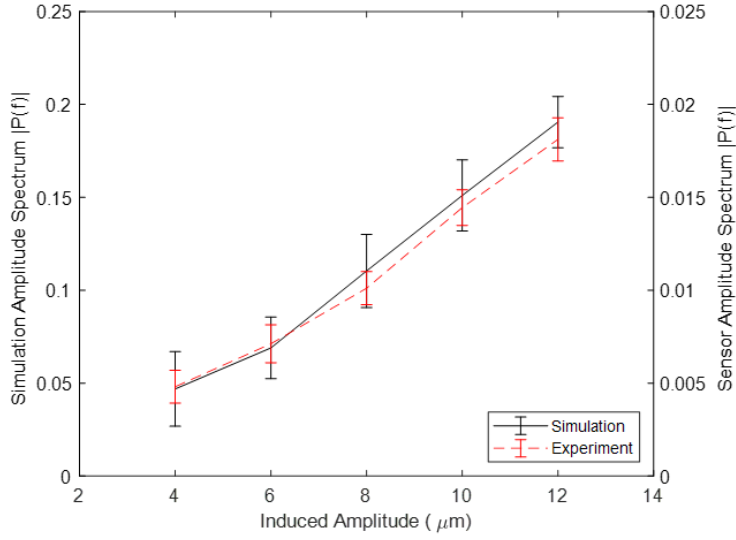


Figure 4.21. Comparison of simulation results of amplitude spectrum to experimental values by induced amplitude

The electron tunnelling effect which was not considered in the strain sensing mechanism analysis, needed to be considered in vibration sensing mechanism analysis due to the short distance change between nanomaterials. The vibration sensing mechanism analysis performed on the same simulation domain as the strain sensing mechanism analysis showed similar results to the actual experimental values. Hence, it was confirmed that the proposed simulation model based on LJ potential was capable of vibration sensing mechanism analysis as well as strain sensing mechanism analysis.

Chapter 5. Application to process monitoring

5.1. Forming process monitoring

Figure 5.1 shows a schematic diagram of the mechanical deformation of the stamp in rubber forming process. The ν which is defined as Poisson's ratio, was a measure for the phenomenon of material to expand in directions perpendicular to the direction of compression. Since stamp is also an elastic material composed of metal, not negligible deformation can occur by a large force of several hundred to several thousand newton [115–117]. The mechanical deformation of stamp in the direction perpendicular to the forming force not only leads to the error of the desired pattern but also causes the downtime of the process due to the physical sticking of the rubber die.

$$D_y = l\varepsilon_y = \frac{l\nu\sigma_x}{E} = \frac{l\nu F_x}{EA} \quad \text{Equation 5.1}$$

The mechanical deformation of stamp d_y can be calculated as shown in **equation 5.1** where l is an original length of stamp, F_x is a forming force, E is a Young's modulus, and A is a cross-sectional area of stamp, respectively.

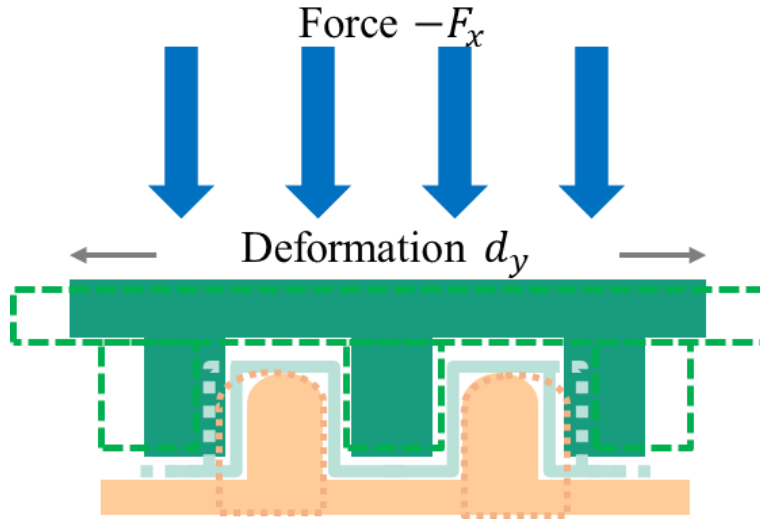


Figure 5.1. The schematic diagram of mechanical deformation of stamp during forming process

Figure 5.2 shows the photograph of experimental setup for rubber forming process monitoring. The sheet metal (1.2379, X5CrNi18–10, HSM Stahl– und Metallhandel GmbH, Germany) was placed on the top of rubber composed of polyurethane (PU) fabricated by molding process with hardness of 85 shore A standards which was contained in the rubber die. All experiments were conducted by press machine (Lauffer VA 850, Maschinenfabrik Lauffer GmbH & Co. KG, Germany) with attached printed sensor onto the stamp (1.2379, X153CrMoV12, HSM Stahl– und Metallhandel GmbH, Germany) in perpendicular direction to the direction of forming process to measure the mechanical deformation of the stamp.

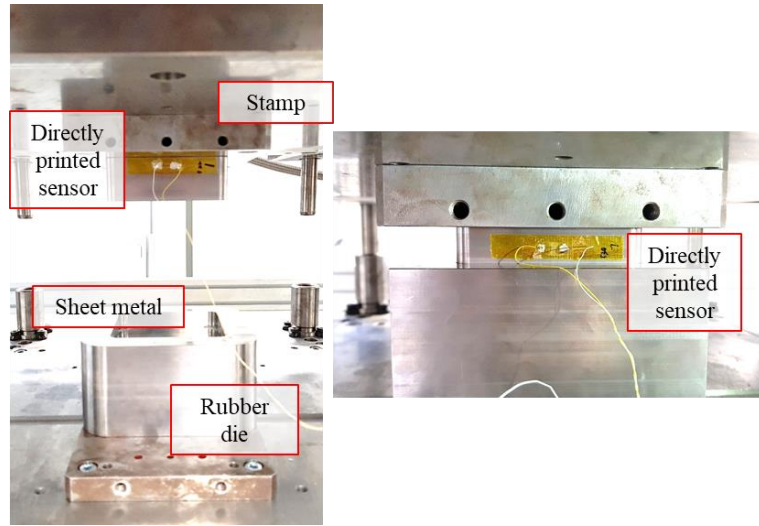


Figure 5.2. The photograph of experimental setup for forming process monitoring using printed sensor

The thickness of sheet metal, maximum force of rubber forming process, and its gradient were used as process parameters for this dissertation as shown in **table 5.1**. The parameter values were chosen for their commonly used value and 50 percent above and below. All experiments were conducted three times for reliability of results with all other parameters are fixed in experiment with one parameter.

Table 5.1. The process parameters of forming process monitoring

| Maximum force (kN) | Force gradient (kN/s) | Thickness (μm) |
|-----------------------|--------------------------|--------------------------------|
| 150 | 45 | 50 |
| 300 | 75 | 75 |
| 450 | 150 | 100 |

Figures 5.3–5.5 show the experimental results according to maximum force, force gradient, and sheet metal thickness, respectively. Since printed sensor is a resistive type passive sensor, the resistance of sensor was measured at a rate of 1,600 Hz by NI USB 9162 carrier, and NI 9234 modules, and DIAdem software (National Instruments, USA). To compare with actual force measured by dynamometer, relative resistance change which is defined by subtracting the initial resistance value from the current resistance value divided by the initial resistance was used.

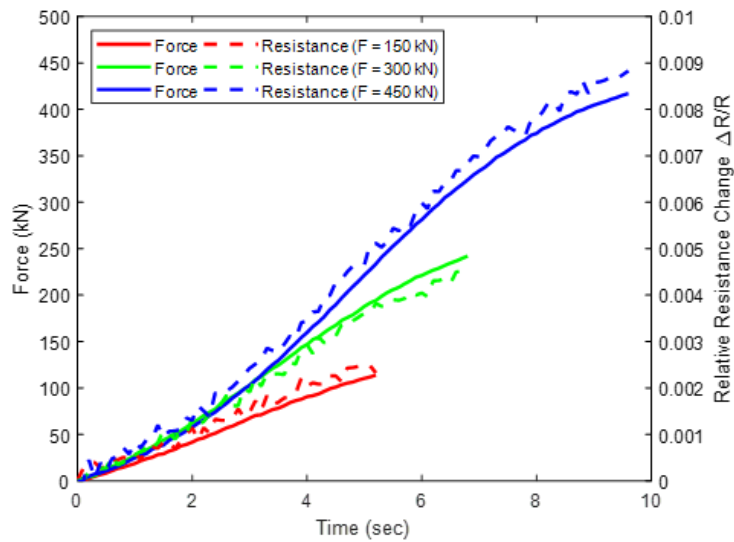


Figure 5.3. Comparison of relative resistance change of sensor to force obtained by dynamometer according to maximum force

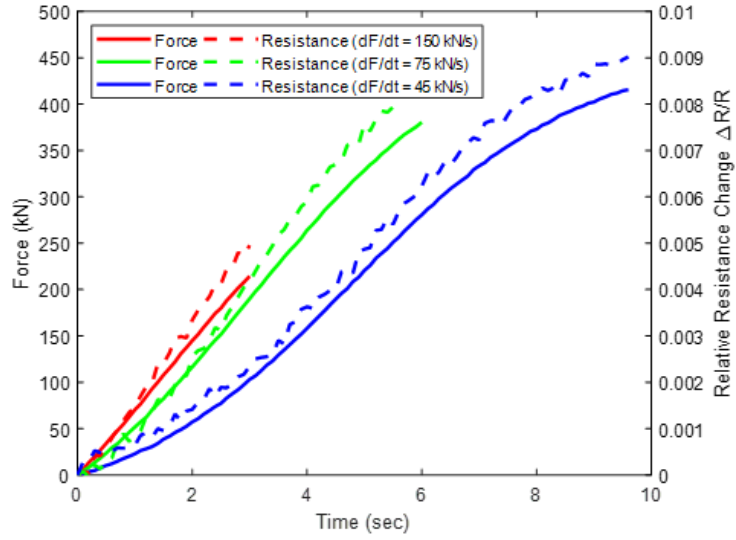


Figure 5.4. Comparison of relative resistance change of sensor to force obtained by dynamometer according to force gradient

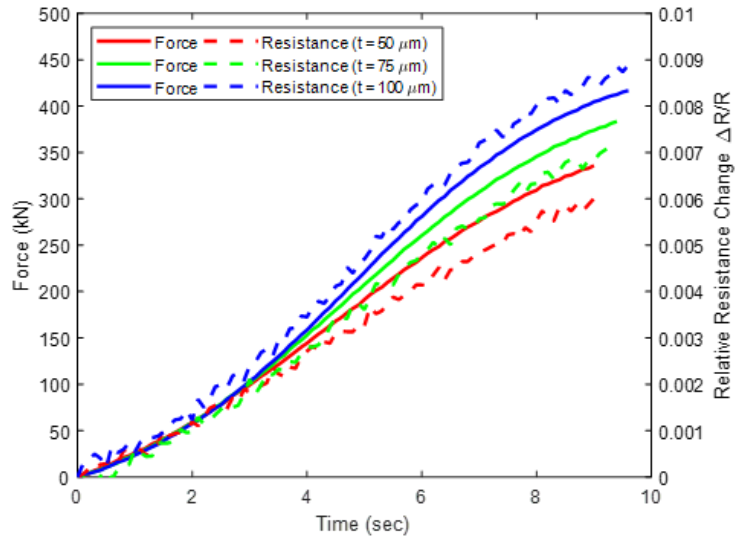


Figure 5.5. Comparison of relative resistance change of sensor to force obtained by dynamometer according to metal thickness

The measured relative resistance change of the sensor and the force value in the experiment showed significantly similar tendency in all experiments. The measured force did not increase linearly but growth rate decreased in actual forming process as also shown by the data obtained by attached sensor.

As shown in **figure 5.3**, the deformation of stamp increased as the maximum force increased. It was due to an increase in stress of stamp caused by increase in force. Furthermore, the high force gradient occurred the high mechanical deformation rate of stamp as shown in **figure 5.4**. Finally, **figure 5.5** showed the effect of sheet metal thickness in terms of force and deformation of stamp. Although the force and its gradient were expected to be constant with thickness, it was slightly different due to variation of the yield strength depending on the thickness. From the experimental results, it was confirmed that forming process monitoring according to the process parameters was available using printed sensor with much lower production cost in comparison to commercial dynamometer.

Figure 5.6 shows the photograph of formed sheet metal. It was demonstrated that each channel was depressed by forming process contrary to the stamp shape. Moreover, surface profile of each channel fabricated by rubber forming process was measured using surface profiler (InfiniteFocus G5, Alicona Imaging GmbH, Austria) as shown in **figure 5.7**. It was shown that elastic rubber generate the boundaries of the channels with a shape of not perpendicular but curvature.



Figure 5.6. The photograph of formed sheet metal fabricated by rubber forming process

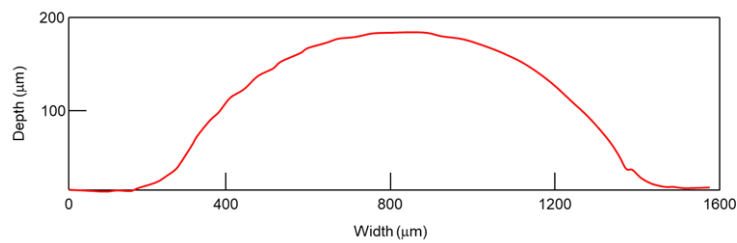


Figure 5.7. The surface profile measurement results of channel of formed sheet metal fabricated by rubber forming process

5.2. Milling process monitoring

Figure 5.8 shows the experimental setup for workpiece vibration measurement. The experiments were performed in a three-axis milling machine (DMG MORI HSC 55 Linear, DMG MORI AKTIENGESELLSCHAFT, Germany). A machine tool with 8 mm diameter and 4 flutes (Pro Steel VHM-Schruppfräser HPC TiAlN, 203052, Hoffmann Group, Germany) and a workpiece of 200 X 150 X 100 mm size (1.2738, 40CrMnNiMo8-6-4, Dörrenberg Edelstahl GmbH, Germany) were used. The printed sensors were directly attached to the workpiece in x, y, and z-directions without mechanical interruption to the milling process.

To validate the performance of printed sensor, a commercial three axes vibration sensor (Accelerometers, 356A26, PCB piezotronics, USA) was attached next to the printed sensor. The data from printed sensor and commercial vibration sensor were measured at a rate of 1,600 Hz per channel by NI USB 9162 carrier, NI 9234 modules, and DIAdem software (National Instruments, USA).

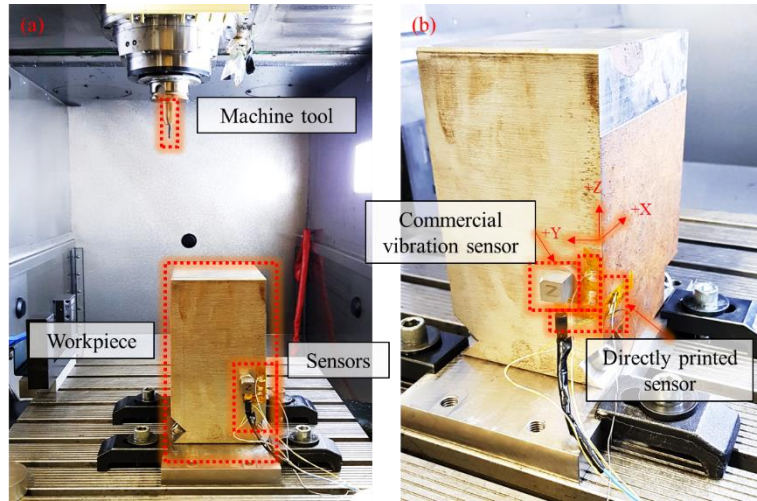


Figure 5.8. The photograph of experimental setup for milling process monitoring using printed sensor

Comparing the performance of printed sensor to commercial vibration sensor was conducted during milling process in x, y, and z-axis direction, respectively as shown in **figures 5.9–5.11**. As shown in **figures 5.9** and **5.10**, the relative resistance change of directly printed sensor exhibited similar signal to vibration measured by commercial vibration sensor in x and y axis direction. The vibration intensity was much greater in the milling state than in the idle state. However, since the milling process was only performed on a two-dimensional plane, there was less vibration measurement in the z-axis direction as shown in **figure 5.11**.

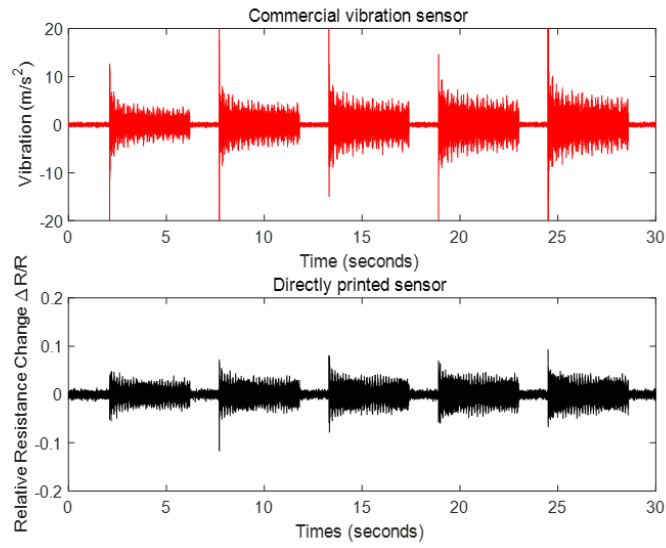


Figure 5.9. Comparison of relative resistance change of sensor to vibration obtained by accelerometer in x-direction

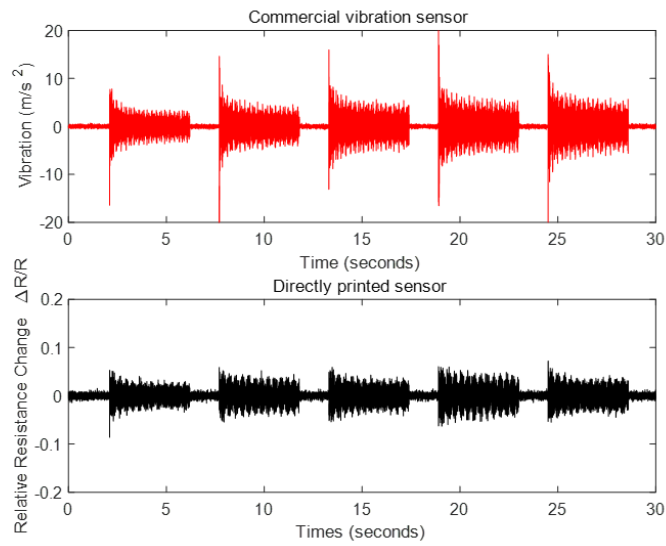


Figure 5.10. Comparison of relative resistance change of sensor to vibration obtained by accelerometer in y-direction

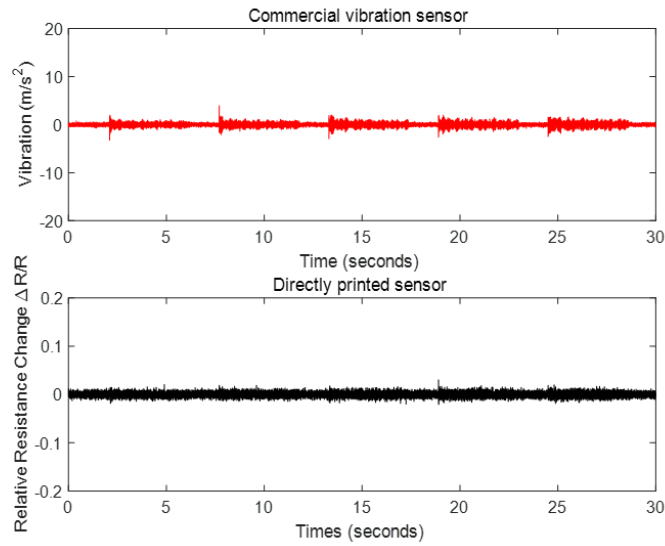


Figure 5.11. Comparison of relative resistance change of sensor to vibration obtained by accelerometer in z-direction

By comparing the measurement data of the commercial vibration sensor and printed sensor, it was confirmed that the power spectrum had peaks almost at identical frequency regardless of the axis direction according to the frequency power spectrum analysis as shown in **figure 5.12–5.14**. It was assumed that the peaks of power spectrum between 400 Hz and 450 Hz were due to the contact between the workpiece and the machine tool during the milling process. Hence, it was demonstrated that the printed sensor could obtain the comparable data to the commercial vibration sensor at a much lower cost with an easy operation method which is suitable for milling process monitoring.

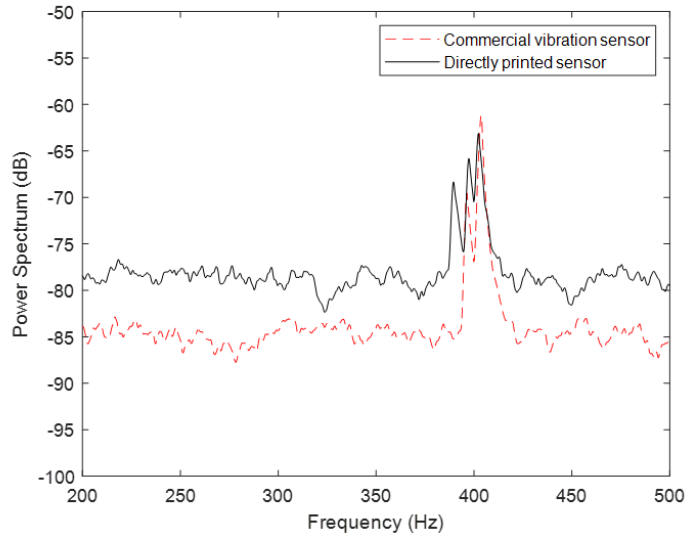


Figure 5.12. Comparison of power spectrum of relative resistance change to vibration in x-direction

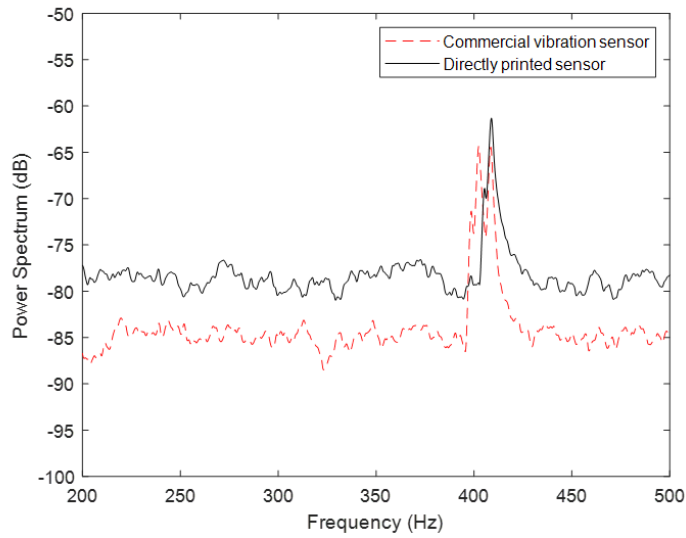


Figure 5.13. Comparison of power spectrum of relative resistance change to vibration in y-direction

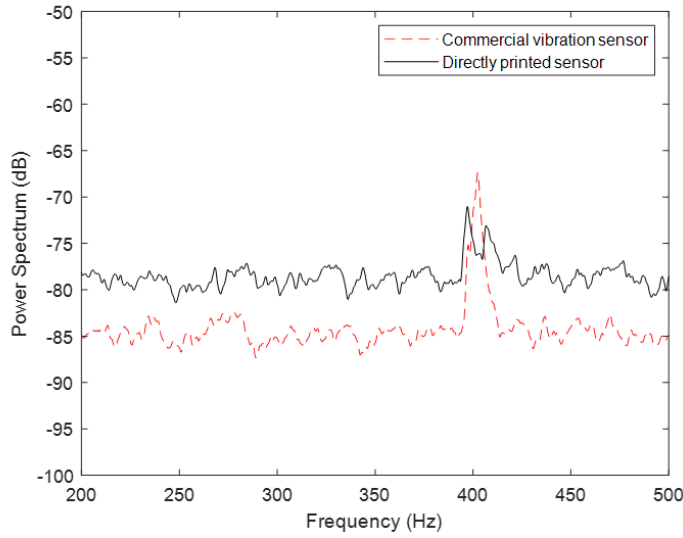


Figure 5.14. Comparison of power spectrum of relative resistance change to vibration in z-direction

Table 5.2. The process parameters of milling process monitoring

| RPM (1/min) | Feed rate (mm/min) | Cutting depth (mm) | Cutting side (mm) |
|-------------|-----------------------|-----------------------|----------------------|
| 5712 | 968 | 4 | 4 |
| 6800 | 1290 | 6 | 6 |
| 7900 | 1612 | 8 | 7.8 |

Further experiments were conducted at the same experimental setup to analyse the sensibility and validity of the printed sensor in different milling conditions as listed in **table 5.2**. Four process parameters including RPM, feed rate, cutting depth, and cutting side were varied. The parameters were chosen for their commonly used values and 15 to 20 percent above and below.

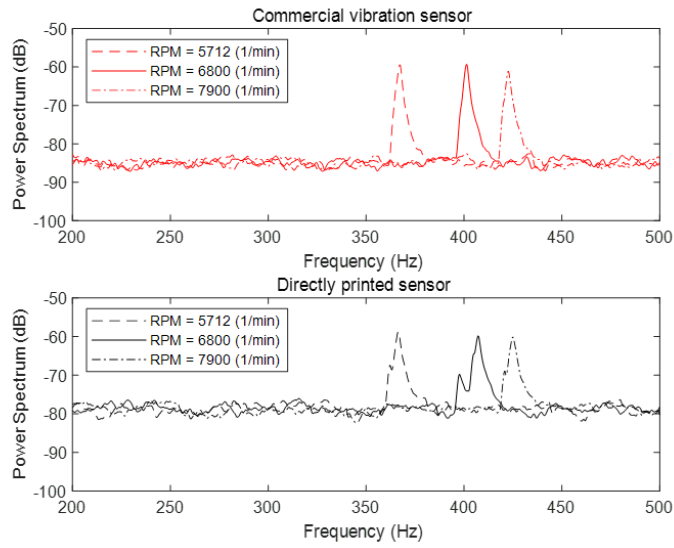


Figure 5.15. Comparison of power spectrum of relative resistance change to vibration according to RPM

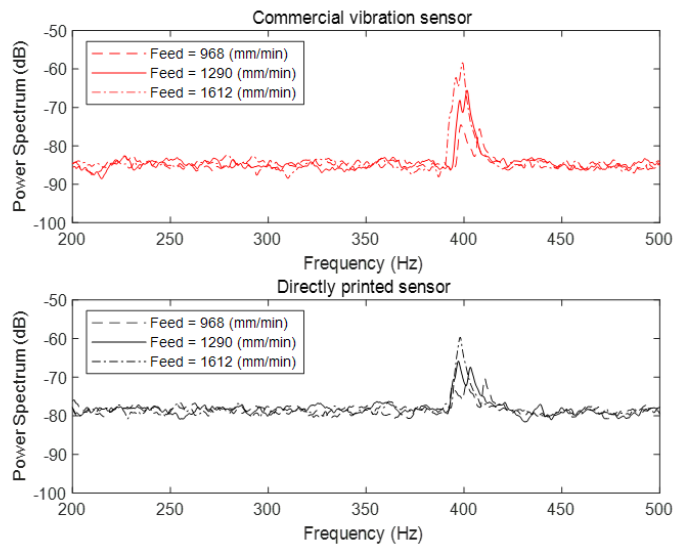


Figure 5.16. Comparison of power spectrum of relative resistance change to vibration according to feed rate

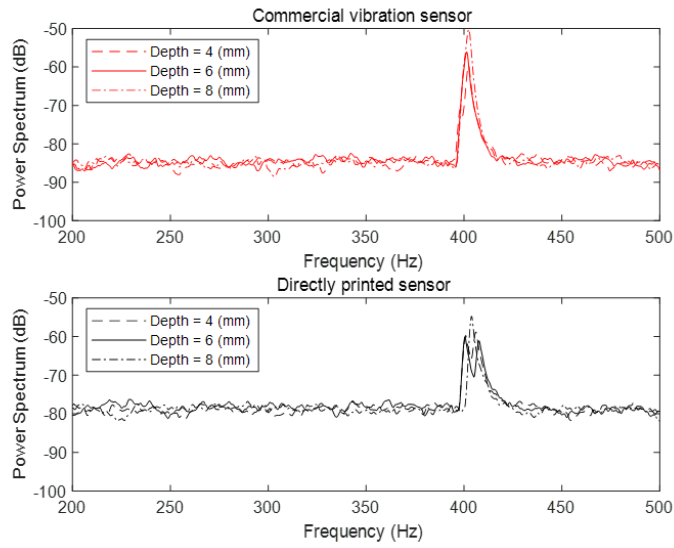


Figure 5.17. Comparison of power spectrum of relative resistance change to vibration according to cutting depth of spindle

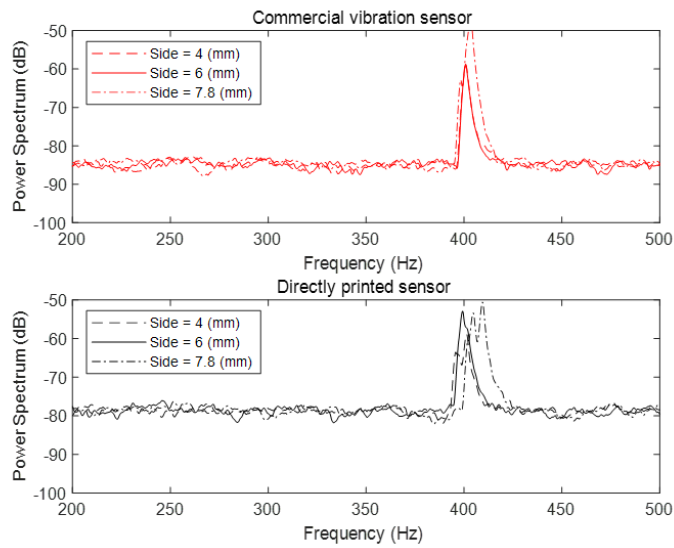


Figure 5.18. Comparison of power spectrum of relative resistance change to vibration according to cutting width of spindle

Figures 5.15–5.18 show the power spectrum analysis for each process parameter comparing the commercial vibration sensor and printed sensor. The experimental results for both sensors showed similar power spectrum. First, since the contact frequency between each tool flute and the workpiece depended on the spindle RPM, the peak frequency increased as the RPM increased while the intensity of the power was maintained at a certain level.

However, the three parameters except RPM affected the power of the peak frequency rather than the position of the peak frequency itself. The power at the peak increased as feed rate, cutting depth, and cutting side increased. It was due to the increase of cutting force applied to the workpiece as each process parameter increased. The higher cutting force occurred more strain on the workpiece which led to an increase of the vibration magnitude [118–120].

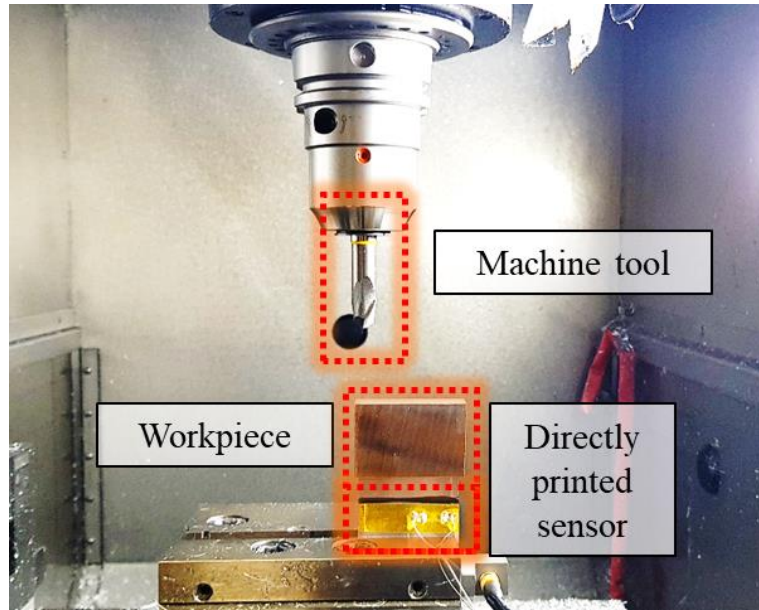


Figure 5.19. The photograph of experimental setup of turbine blade milling process monitoring using printed sensor

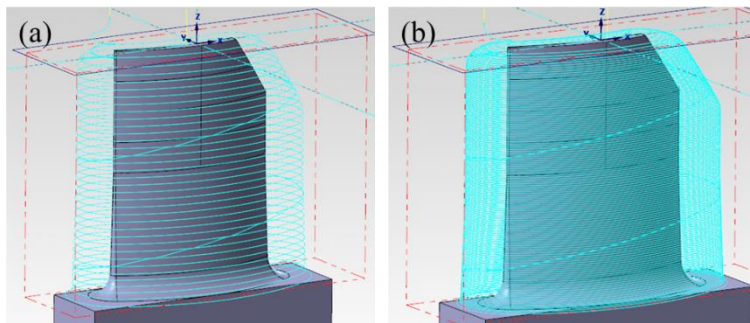


Figure 5.20. The schematic diagram of turbine blade milling process in order of (a) pre-finishing and (b) finishing

Figure 5.19 shows experimental setup for monitoring of turbine blade milling process using printed sensors attached on the workpiece. In order to serve the mass production of turbine components and provide the evidence for the compliance with certification requirements, vibration data should be obtained in real time during the whole milling process.

A tool with 12 mm diameter and 1.5 mm corner radius (GARANT VHM – Torusfräser, TiAlN, 206040, Hoffmann Group, Germany) and workpiece with 62 X 50 X 15 mm (EN AW 5083, AlMg4.5Mn0.7, GLEICH Aluminum GmbH, Germany) were used. The actual turbine blade milling process was conducted in order of roughing, pre-finishing, and finishing as shown in **figure 5.20**. However, the data for only finishing process was analysed which majorly affects the workpiece accuracy and surface quality.

Since the relative resistance change had a drift property according to operation time, envelope detection and subtracting lower envelope from raw data of printed sensor were required. To detect the lower envelope of sensor raw data, Hilbert transformation was implemented which imparts a phase shift of -90° to every Fourier component of a function. By Hilbert transformation, analytic representation of a real-valued signal was derived.

After subtracting the lower envelope, processed sensor data was compared to geometrical tool path data to find surface defect and achieve 3D data mapping in real time as shown in **figure 5.21**.

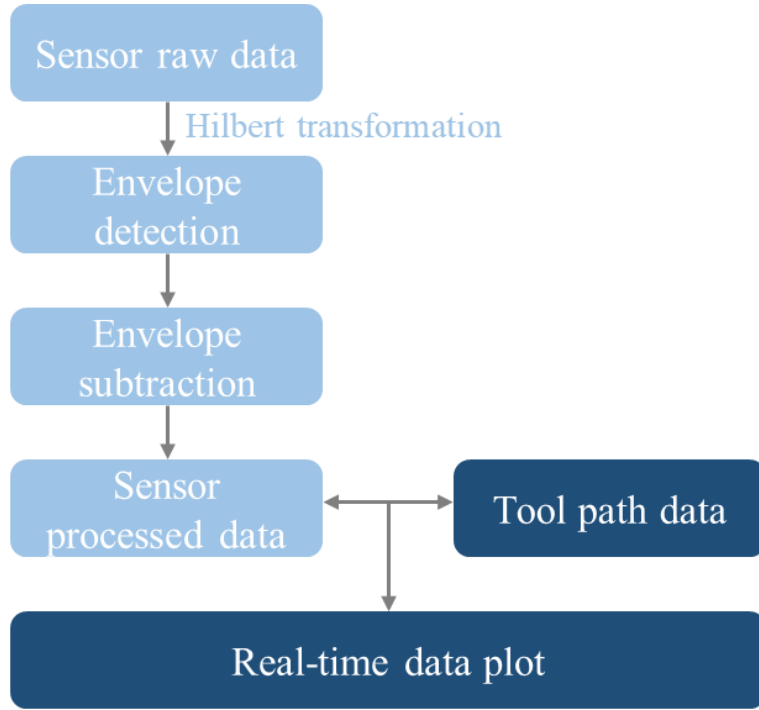


Figure 5.21. The schematic diagram of real time data processing of relative resistance change of sensor

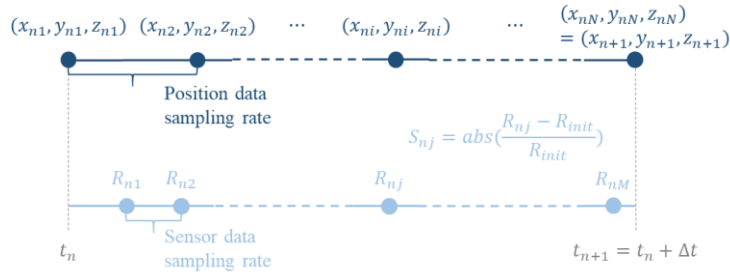


Figure 5.22. The schematic diagram of real time data fusion of tool path data and processed sensor data

Since the measurement frequency of the sensor data and tool path data were different each other, it was necessary to combine data in one identical time axis as shown in **figure 5.22**. First, tool path data in given time range was defined as shown in **equation 5.2**.

$$\begin{aligned} X_n &= \{X_{ni}\} \text{ for } i = 1, \dots, N \\ &= \{(x_{n1}, y_{n1}, z_{n1}), (x_{n2}, y_{n2}, z_{n2}), \dots, (x_{nN}, y_{nN}, z_{nN})\} \end{aligned} \quad \text{Equation 5.2}$$

It was needed to calculate the relative resistance change of sensor data from processed sensor data without the drift of sensor performance, **equation 5.3** was defined for further analyses.

$$\begin{aligned} S_n &= \left\{ \text{abs} \left(\frac{R_{nj} - R_{init}}{R_{init}} \right) \right\} \text{ for } i = 1, \dots, M \\ &= \left\{ \text{abs} \left(\frac{R_{n1} - R_{init}}{R_{init}} \right), \text{abs} \left(\frac{R_{n2} - R_{init}}{R_{init}} \right), \dots, \text{abs} \left(\frac{R_{nM} - R_{init}}{R_{init}} \right) \right\} \end{aligned} \quad \text{Equation 5.3}$$

Based on the measurement frequency of sensor, which has higher frequency than tool path data, the maximum value in given time scale was used. Finally, function for mapping from tool path data to processed sensor data was derived as shown in **equation 5.4**.

$$f(X_n) = \max(S_{nj}) \text{ for } i = 1, \dots, M \quad \text{Equation 5.4}$$



Figure 5.23. The photograph of fabricated turbine blade with good surface quality

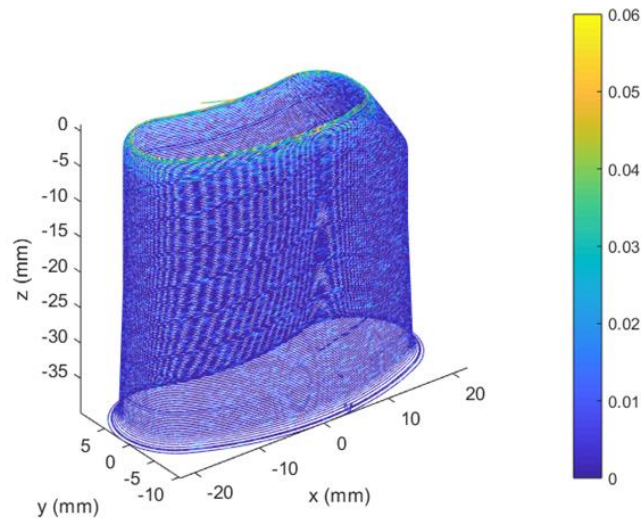


Figure 5.24. The sensor data visualisation of turbine blade with good surface quality



Figure 5.25. The photograph of fabricated turbine blade with bad surface quality

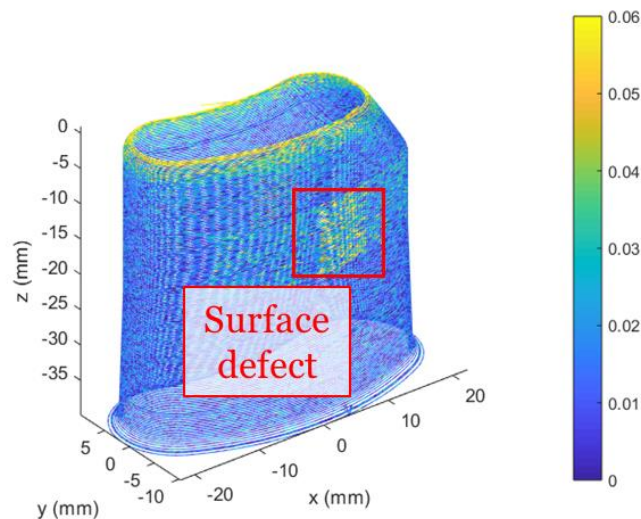


Figure 5.26. The sensor data visualisation of turbine blade with bad surface quality

As shown in **figures 5.23** and **5.25**, the milling process was performed multiple times with the same workpiece and machine tool with good surface quality and poor surface quality, respectively by adjustment of process parameters. Since the bigger cutting depth was used for the machining of turbine blade with poor surface quality, surface defects occurred while the overall shape was similar to the turbine blade with good surface quality. The vibration data was obtained in real time by printed sensor to monitor the vibrations during the machining process. The maximum value of the relative resistance change was plotted during the execution of each NC program line as shown in **figures 5.24** and **5.26**. According to results, much larger vibrations partly occurred at the turbine blade milling with poor surface quality in comparison to those of good surface quality. Moreover, it was confirmed that a larger vibrations occurred when machining the upper part of the turbine blade like a general thin wall milling process. In addition, since the prediction of actual visible surface defect using obtained data by the printed sensor was possible, high possibilities for application to digital twin for various machining applications is expected in the future.

5.3. Wireless communication monitoring

Since most of passive strain sensors directly measure their electrical properties including resistance and capacitance varied by strain, soldering and wiring process is needed for actual usage. However, electrical wires usually limit the usability of strain sensors and even increase the noise of the measured electrical signal which induces inaccurate information.

To overcome the limitation, radio frequency identification (RFID) technology have widely been used for wireless communication strain sensors [121–123]. RFID-based sensors have their advantage of wireless, passive, and low-cost production. Specifically, chipless RFID technology offers several advantages over the chipped RFID technology in terms of cost, simplicity, printability, and ability to operate in high-temperature environments [124–128]. One of the major reasons of low-cost production for chipless RFID sensor is unnecessariness of a reader for transmitting and receiving wave signals and power sources for active operation which are major components of conventional RFID sensor. In particular, LC resonance-based chipless RFID encodes the information using only the antenna by oscillation of LC circuit. Moreover, since LC resonance-based chipless RFID could be directly printed onto flexible and stretchable substrate with only conductive materials, there have been several efforts to utilise them as stretchable electronic devices [129–131].

In this dissertation, stretchable and chipless RFID strain sensors have been fabricated by AFN printing system onto flexible substrate. Schematic illustration of the fabrication process for stretchable RFID strain sensor is shown in **figure 5.27**. As mentioned above, aerosolised nanocomposite based on AgNPs and MWCNTs are directly printed onto PDMS substrate. Using mechanical translation of multi-axis stage and aerosolised nanocomposite beam spurting out from the fixed nozzle, RFID strain sensor was printed with desired design.

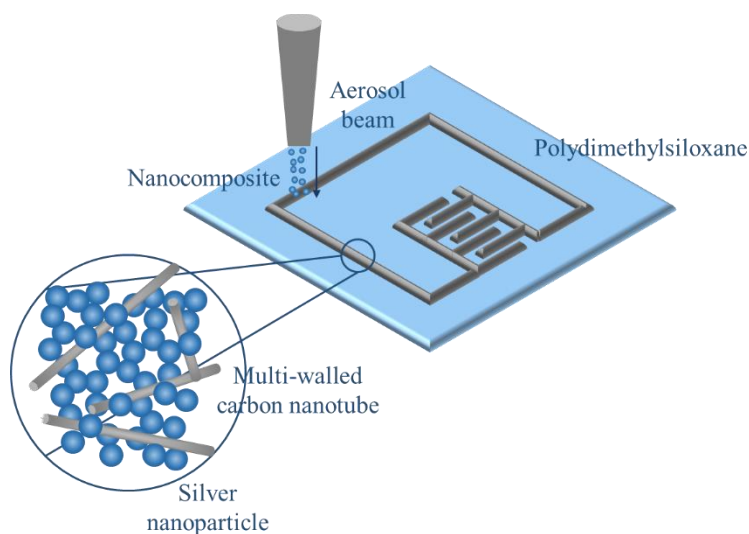


Figure 5.27. The schematic diagram of fabrication process for stretchable and wireless communication sensor

The optical images of fabrication process by each printing step are shown in **figure 5.28**. The conductive pattern was just scattered and not electrically conductive if the printing time for the pattern does not exceed the minimum value. In this dissertation, nanocomposite were printed enough to mechanically attached together and electrically stable through a few iterations of printing over the minimum value of scan time.

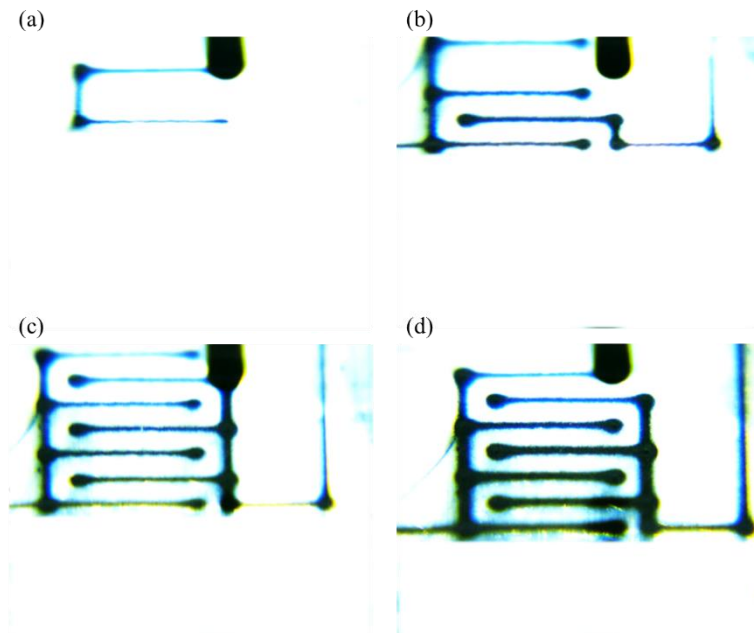


Figure 5.28. The optical microscopic image of stretchable and wireless communication sensor printing by printing steps

Figure 5.29 shows the optical image of the fabricated nanocomposite RFID strain sensor. It was transparent, flexible, stretchable, and has a total length of 3 mm in both horizontal and vertical directions.

Figure 5.30 is an optical image of magnified view for printed capacitance with finger shape. Parallel conductive plates composed of nanocomposite with a distance of several hundred micrometers were printed in the form of finger capacitors. The gap between the parallel plates was well maintained and not contacted each other on the PDMS substrate.

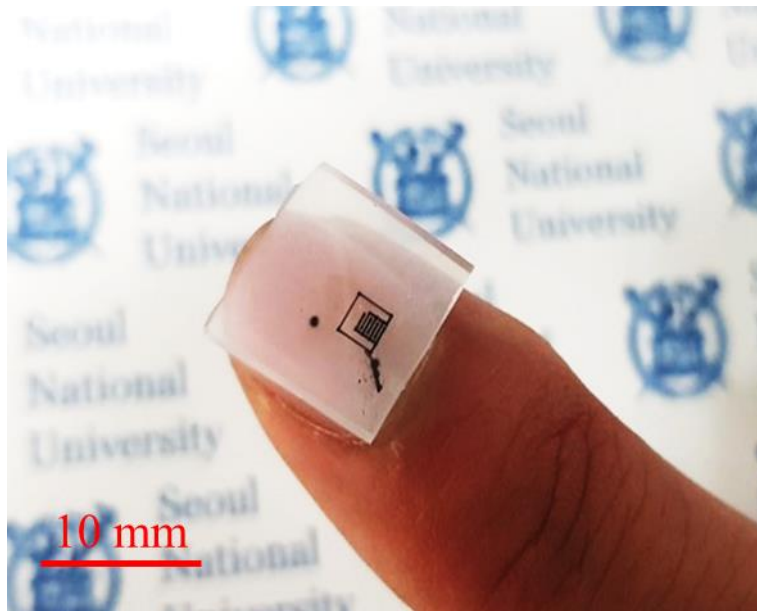


Figure 5.29. The photograph of fabricated stretchable and wireless communication sensor

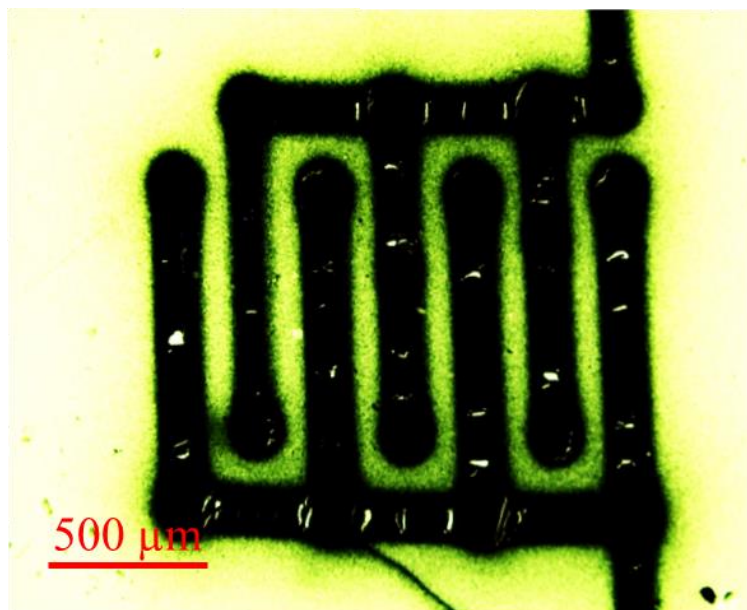


Figure 5.30. The optical microscopic image of finger capacitor in stretchable and wireless communication sensor

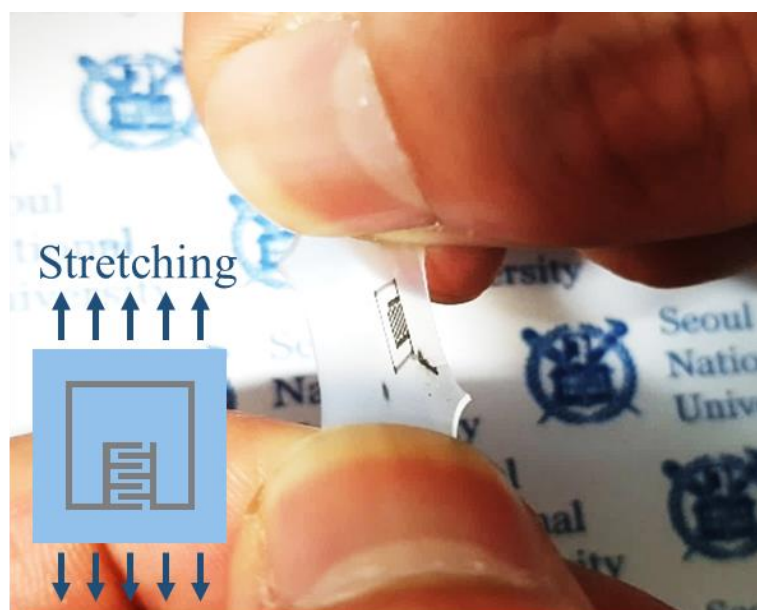


Figure 5.31. The photograph of stretching motion of stretchable and wireless communication sensor



Figure 5.32. The photograph of twisting motion of stretchable and wireless communication sensor



Figure 5.33. The photograph of folding motion of stretchable and wireless communication sensor

Figures 5.31–5.33 show stretched, twisted, and folded motion of fabricated RFID sensor. Since elastic material with high elongation at break as a substrate was used for RFID strain sensor, motion with the high degree-of-freedom was able without mechanical failure.

The chipless RFID sensor consists of a single antenna serving as both a transmitter and a receiver. The input signal from the vector network analyser (VNA) is the impulse used for interrogating the chipless RFID tag while the total received signal consists of three components including rejection and backscatter of structural mode and antenna mode, respectively as shown in **figure 5.34** and **equation 5.5**.

$$y(t) = y_r(t) + y_s(t) + y_a(t) \quad \text{Equation 5.5}$$

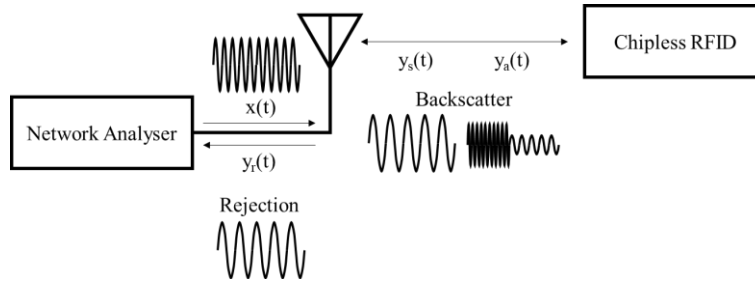


Figure 5.34. The schematic diagram of VNA of stretchable and wireless communication sensor

The largest and the first received component is the rejection of the transmit pulse $y_r(t)$ due to the return loss profile of the antenna which of transients gradually decay down to zero. At this moment in time, the reader antenna has fully transmitted and receptive to any backscatter coming from the tag. The structural mode of the backscatter $y_s(t)$ is followed by the antenna mode of the backscatter $y_a(t)$, which is the weakest and the last component to be received.

Due to the presence of a tag in front of transmit and receive antenna, the original return loss of the antenna slightly changes. The return loss of the antenna is affected by the backscatter incident on the antenna and is considered to be electromagnetically loaded by the chipless tag as shown in **equations 5.6** and **5.7** [132].

$$y_r(t) = F^{-1}\{S_{11}(f)X(f)\} \quad \text{Equation 5.6}$$

$$y_s(t) + y_a(t) = F^{-1}\{(S(f) - S_{11}(f))X(f)\} \quad \text{Equation 5.7}$$

Since the antenna mode of the backscatter is the weakest component as discussed above, this dissertation focused on the structural mode of the backscatter. Here, the structural mode backscatter is simply an attenuated version of the signal that is emitted by reader antenna into the free space, which is in turn picked up by the same antenna after a propagation delay through the wireless channel. By assuming the radar range equation for a bi-static radar, **equation 5.8** was derived as shown in below.

$$\frac{P_r}{P_t} = e_t(1 - |S_{11}(f)|^2) \frac{D_t(\theta_t, \phi_t)}{4\pi R_1^2} \sigma \frac{\lambda^2}{4\pi} \frac{D_r(\theta_r, \phi_r)}{4\pi R_2^2} e_r(1 - |S_{22}(f)|^2)$$

Equation 5.8

Where P_r and P_t are the received and transmitted power while $S_{11}(f)$ and $S_{22}(f)$ are the return loss of the transmitting and receiving antenna, respectively. $D_t(\theta_t, \phi_t)$ and $D_r(\theta_r, \phi_r)$ are the directivity of the transmit and receiving antenna. By taking a square root of **equation 5.8**, **equation 5.9** was derived where Z_0 is the characteristic impedance.

$$\frac{|Y_s(f)|/\sqrt{Z_0}}{|X(f)|/\sqrt{Z_0}} = (1 - |S_{11}(f)|^2) \sqrt{e_t \frac{D_t(\theta_t, \phi_t)}{4\pi R^2}} \sqrt{\sigma \frac{\lambda^2}{4\pi}} \sqrt{e_r \frac{D_r(\theta_r, \phi_r)}{4\pi R^2}}$$

Equation 5.9

Since chipless RFID system serves as both the transmitting and receiving antenna, $S_{11}(f)$ is assumed to equals to $S_{22}(f)$ and R_1 equals to R_2 . By including the propagation delay introduced to the signal when it is propagating through the forward and backward wireless channels as shown in **equation 5.10**, simplified equation is derived as shown in **equation 5.11** where η_T and η_R account for the antenna gain and other losses associated with the transmission and reception of signals, which is equal in this dissertation.

$$H_R(f) = H_T(f) = H(f) = \frac{1}{\sqrt{4\pi R}} \exp(-j2\pi f \frac{R}{c} t) \quad \text{Equation 5.10}$$

$$Y_s(f) = X(f) \eta_T (1 - |S_{11}(f)|^2) \eta^2 H(f) A(f) \quad \text{Equation 5.11}$$

Based on analytical study, the data by separating $Y_s(f)$ was measured from the total received signal. It was estimated that $Y_s(f)$ could evaluate the performance regarding the RFID characteristics of the fabricated RFID strain sensor.

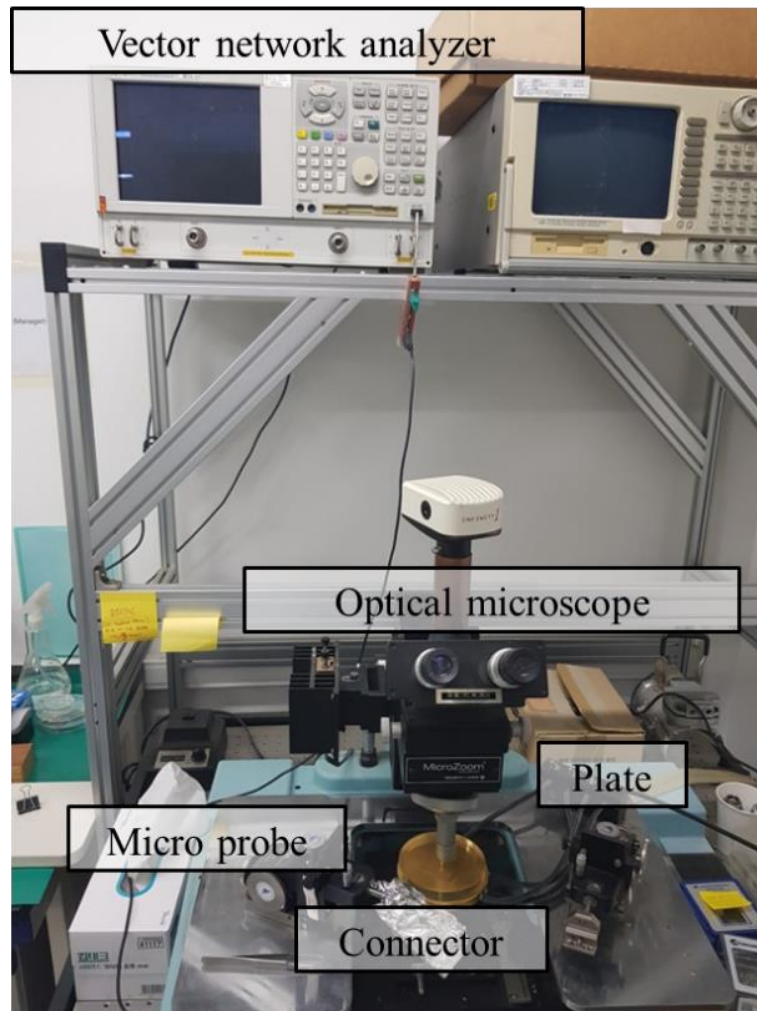


Figure 5.35. The photograph of experimental setup for vector network analysis of stretchable and wireless communication sensor

Figure 5.35 shows the experimental setup for VNA which is constructed for performance evaluation test of stretchable and wireless communication sensor. The characterisation of experiments was conducted by vector network analysis and scattering parameter (s-parameter) measurement. S-parameter is widely used indicator for networks operating at radio frequency (RF) and microwave frequency where signal power and energy considerations are more easily quantified than currents and voltages. Since s-parameter is changed with the measurement frequency, resonance frequency is denoted when the intensity of the radar cross-section (RCS) has a peak.

The VNA was used in the same conditions for all following experiments to measure s-parameter. The resonance frequency by various design variables of LC resonance based passive RFID sensor was measured for this dissertation.

Here, changes in inductance and capacitance by design variables occurred shift of resonance frequency as shown in below where **F** is the resonance frequency, **L** is the inductance, **C** is the capacitance, and **R** represents the resistance of sensor. In general, increase of inductance and capacitance decreases resonance frequency as shown in **equation 5.12**.

$$F = \frac{1}{2\pi} \sqrt{\frac{1}{LC} - \left(\frac{R}{L}\right)^2} \quad \text{Equation 5.12}$$

In this dissertation, finger capacitor and single turn inductor were used to generate resonance in LC circuit. Equations for single turn inductor and finger capacitor were demonstrated in previous studies as shown **equations 5.13** and **5.14** where **d** is the outer diameter, **A** is the outer area, **w** is the turn width, and ϵ_0 is vacuum permittivity, ϵ_r is relative permittivity of the substrate, **t** is the thickness of the electrode, **l** is the finger length, **m** is the gap from a finger to the main bar, **n** is the number of fingers, **g** is the gap between two adjacent fingers, C_p is a parasitic capacitance in farad for inductance and capacitance, respectively [133, 134].

$$L = 4 \left\{ d \ln \frac{8A}{(\sqrt{2}+1)dw} + w - (2 - \sqrt{2})d \right\} \quad \text{Equation 5.13}$$

$$C = \epsilon_0 \epsilon_r t (l - m) \left(\frac{2n-1}{g} \right) + nC_p \quad \text{Equation 5.14}$$

Since the resonance frequency of RFID strain sensor is regulated by feature sizes and geometry of the inductor and capacitor, the gap of finger capacitor **g**, the length of finger capacitor **l**, outer diameter **d**, and turn width **w** were used for dependent design variables for RFID strain sensor in this dissertation. According to above equations, it was estimated that increase of the gap of finger capacitor **g**, and turn with **w** increased resonance frequency while increase of the length of finger capacitor **l**, and outer diameter **d** decreased resonance frequency.

Using just simple process parametrisation for AFN printing process, finger gap, finger length and outer diameter were controlled. In terms of turn width, scan time defined as a pattern length by feed rate was regulated to control pattern width. All parameters consisted of four levels, and all experiments were repeated three times for reliability of experimental data as shown in **table 5.3**.

Table 5.3. The design parameters for resonance circuit printing

| Gap of finger capacitor g (μm) | Length of finger capacitor l (μm) | Outer diameter of inductor d (μm) | Turn width of inductor w (μm) |
|--|---|---|---|
| 200 | 800 | 2,600 | 16 |
| 250 | 1,000 | 2,800 | 27 |
| 300 | 1,200 | 3,000 | 42 |
| 350 | 1,400 | 3,200 | 52 |

Figures 5.36–5.39 show RCS spectra by four design variables for this dissertation. It was shown that precise control of the initial resonance frequency of sensors by modifying the values of capacitance and inductance was possible to match the operating frequency range of measuring devices.

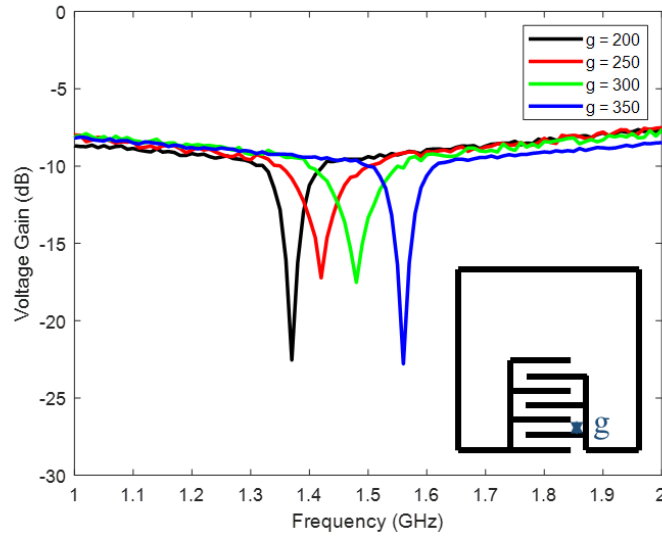


Figure 5.36. The experimental results of voltage gain of resonance circuit by frequency according to finger gap

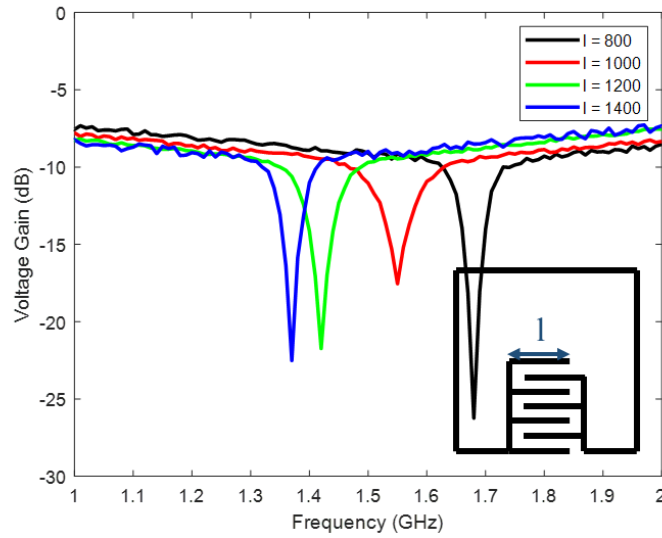


Figure 5.37. The experimental results of voltage gain of resonance circuit by frequency according to finger length

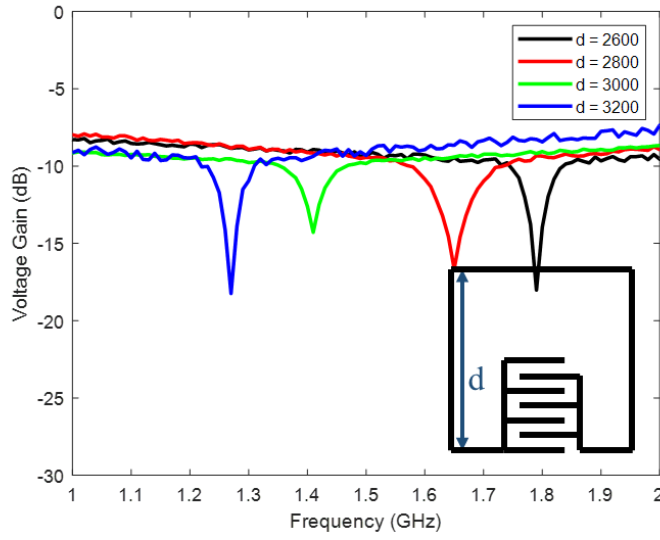


Figure 5.38. The experimental results of voltage gain of resonance circuit by frequency according to outer diameter

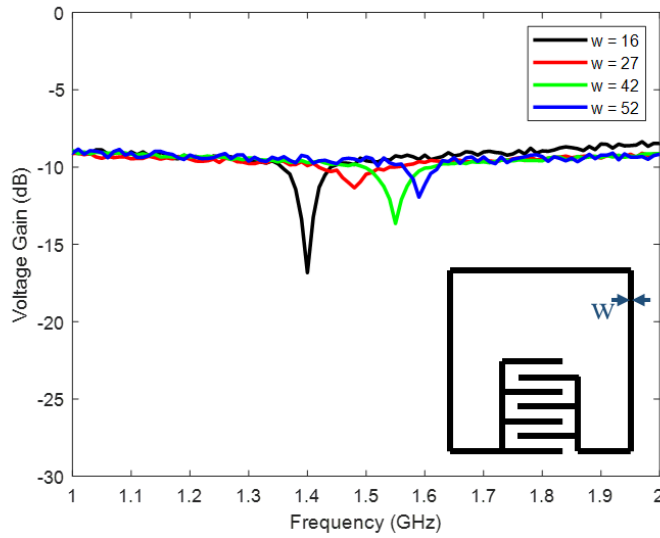


Figure 5.39. The experimental results of voltage gain of resonance circuit by frequency according to turn width

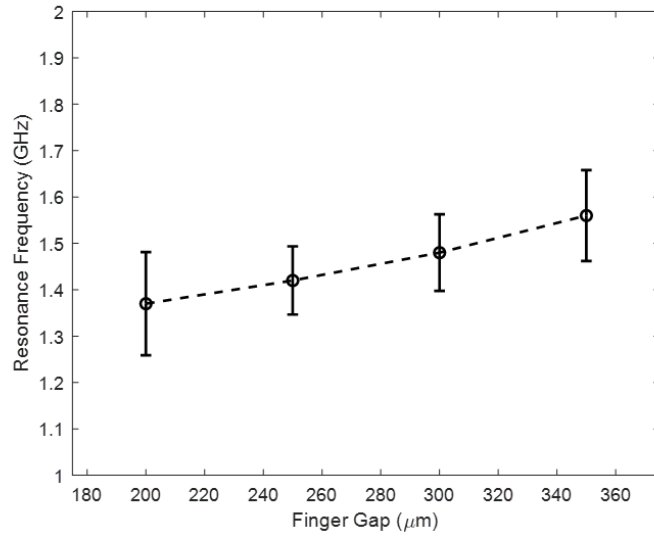


Figure 5.40. The experimental results of resonance frequency of AFN printed circuit by finger gap

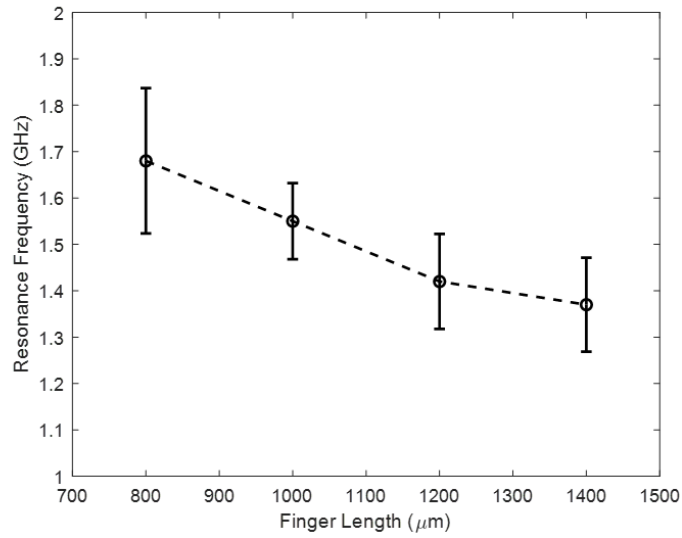


Figure 5.41. The experimental results of resonance frequency of AFN printed circuit by finger length

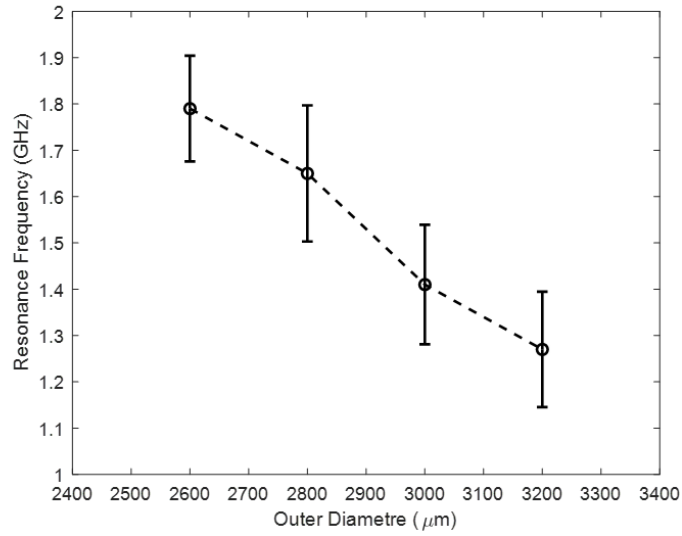


Figure 5.42. The experimental results of resonance frequency of AFN printed circuit by outer diameter

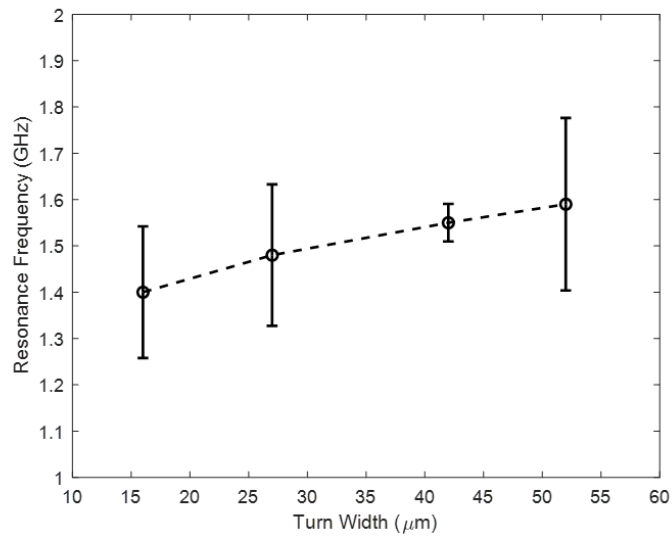


Figure 5.43. The experimental results of resonance frequency of AFN printed circuit by turn width

Figures 5.40–5.43 show resonance frequency shift by design variables for this dissertation. The resonance frequency was increased by the gap of finger capacitor and turn width while decreased by the length of finger capacitor and outer diameter of single turn inductor as expected. The increase of the gap of finger capacitor and turn width decreased capacitance and inductor respectively, while the length of finger capacitor and outer diameter caused the opposite result.

The resonance frequency shift was measured while stretching fabricated RFID strain sensor. **Figure 5.44**(a) shows schematic illustration for stretching RFID strain sensor in both horizontal ($\epsilon_2 = 0$) and vertical direction ($\epsilon_1 = 0$). The experiment was conducted discontinuously while gradually increasing in each direction using a jig. The jig for stretching RFID strain sensor was fabricated by 3D printer as shown in **figure 5.44**(b). It was used to hold both ends of the RFID sensor and maintained a constant distance while s-parameter measurement.

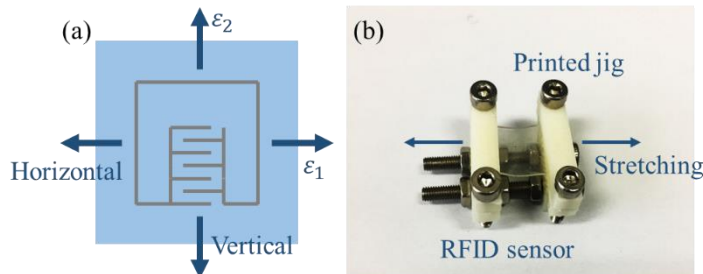


Figure 5.44. (a) The schematic diagram of resonance circuit stretching and (b) the photograph of 3D printed jig for stretching

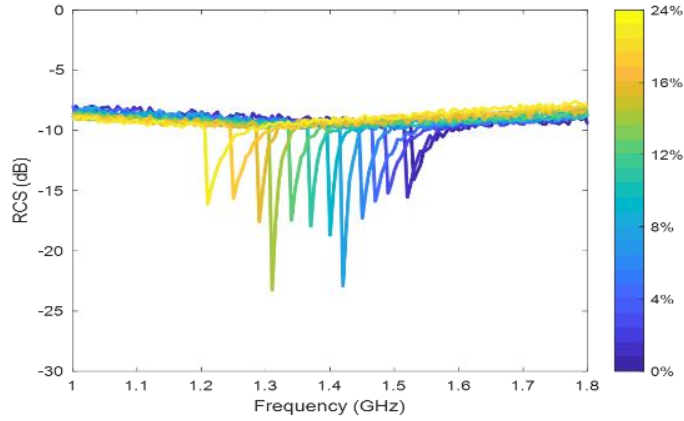


Figure 5.45. The experimental results of RCS spectrum during resonance circuit stretching in horizontal direction

Figure 5.45 shows RCS spectra of the RFID strain sensor according to tensile strain in horizontal direction over 20%. The resonance frequency decreased as RFID strain sensor gradually extended in horizontal direction. It was demonstrated that AgNPs enhanced MWCNTs conductive networks of conductive patterns fabricated by AFN printing increased the stretchability as discussed above.

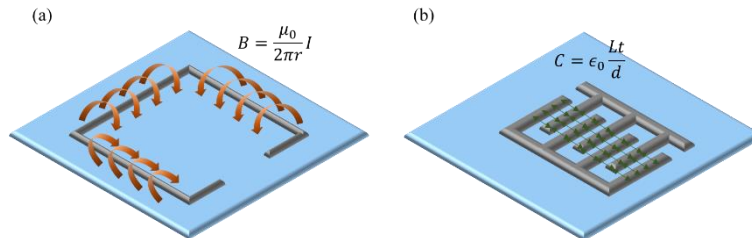


Figure 5.46. The schematic diagram of inductance and capacitance behaviour of resonance circuit

Since stretching sensor occurred decrease of the gap of finger capacitor and increase of the length of finger capacitor, resonance frequency was decreased by tensile strain. **Figure 5.46** shows the schematic diagram of inductance and capacitance behaviour of AFN printed RFID sensor which are also shown in **equations 5.15** and **5.16**.

$$B = \frac{\mu_0}{2\pi} I = \frac{\mu_0}{2\pi} \frac{dV}{dt} \frac{dt}{d\varepsilon} \frac{d\varepsilon}{dR} = -\frac{\mu_0 f_c}{GF} A \sin(2\pi f_c t) \frac{dt}{d\varepsilon} \quad \text{Equation 5.15}$$

$$C = \epsilon_0 \frac{Lt}{d} = \epsilon_0 \frac{L(1+\varepsilon)t(1-\gamma\varepsilon)}{d(1-\gamma\varepsilon)} \quad \text{Equation 5.16}$$

Since magnetic field impressed in sensor usually influenced by the current, magnetic field varied by the resistance of sensor with highly sensitive properties under same magnitude of impressed voltage. Otherwise, electrical field usually influenced by the length of pattern rather than the highly sensitive properties of AFN printed pattern which was related to the capacitance.

For the large-scale deformation, substrate and pattern transformed in vertical direction even they were stretched in horizontal direction due to Poisson's ratio. It was assumed that maximum measurable range and nonlinear properties were dominantly related to vertical deformation.

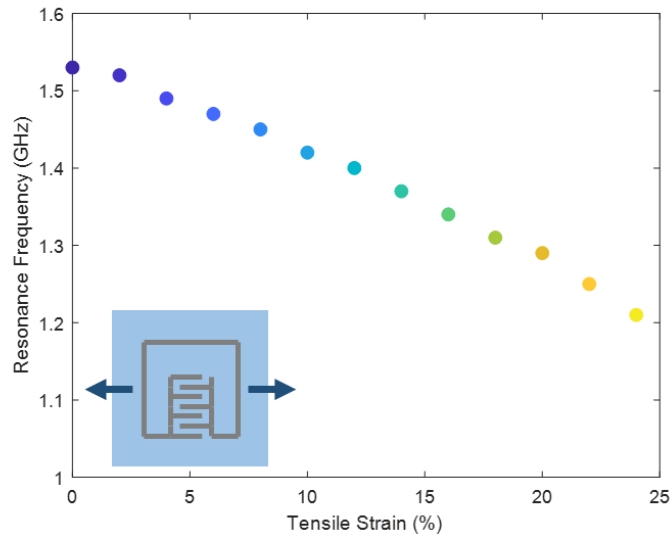


Figure 5.47. The experimental results of resonance frequency of printed circuit by tensile strain in horizontal direction

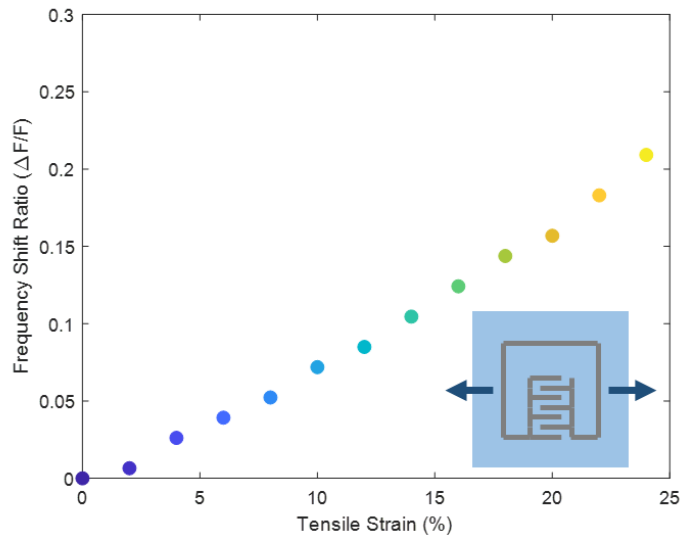


Figure 5.48. The experimental results of frequency shift ratio of printed circuit by tensile strain in horizontal direction

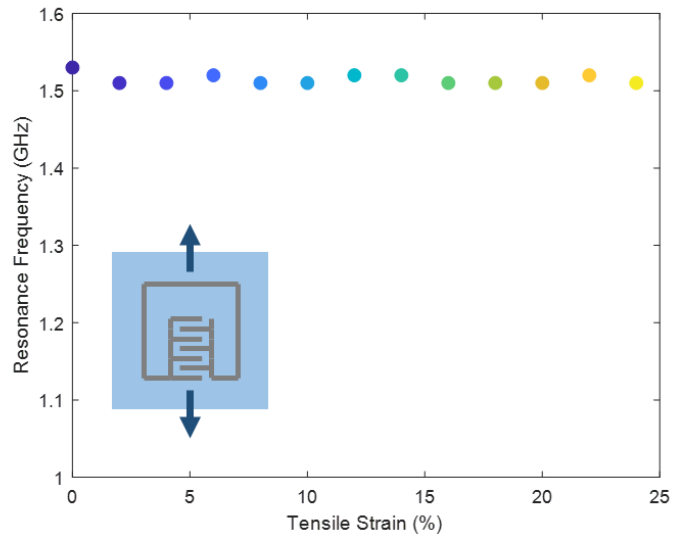


Figure 5.49. The experimental results of resonance frequency of printed circuit by tensile strain in vertical direction

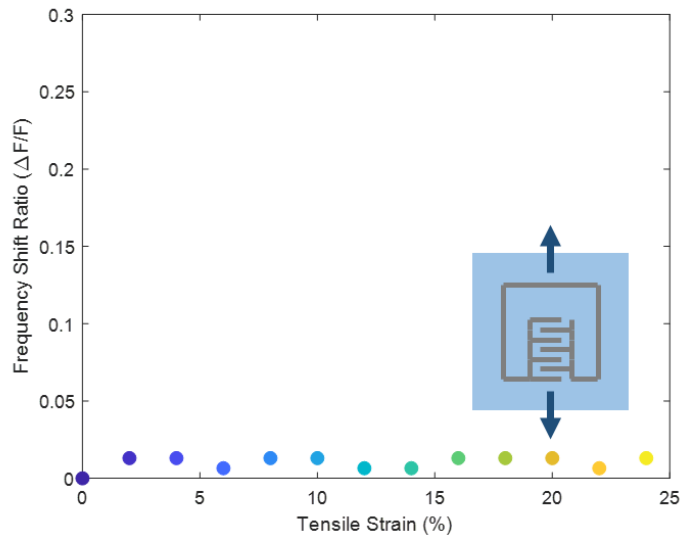


Figure 5.50. The experimental results of frequency shift ratio of printed circuit by tensile strain in vertical direction

The GF which is defined as resonance frequency shift ratio by tensile strain was calculated separately in horizontal and vertical direction. Since it is a commonly used indicator for evaluation of sensitivity of strain sensor regardless of physical properties, it was used to estimate the performance of printed sensor and compare with other commercial sensors.

Figures 5.47 and **5.48** show resonance frequency shift and frequency shift ratio of RFID strain sensor by strain in horizontal direction. As a result, the resonance frequency which was over 1.5 GHz initially decreased under the 1.2 GHz after elongation.

The fabricated strain sensor exhibited a high sensitivity of gauge factor over 0.6 in horizontal direction stretching. It was supposed that high sensitivity of fabricated sensor was caused by stretchable properties of AFN printed pattern composed of nanocomposite and Poisson' s ratio of PDMS substrate which increased the geometric variation of printed LC circuit.

However, resonance frequency was not shifted but remained by stretching in vertical direction as shown in **figures 5.49** and **5.50**. Hence, it was demonstrated that fabricated RFID sensors measured the strain in only one direction without influence on the strain in the other direction. As a result, a RFID strain sensor capable of measuring only one direction independently was developed.

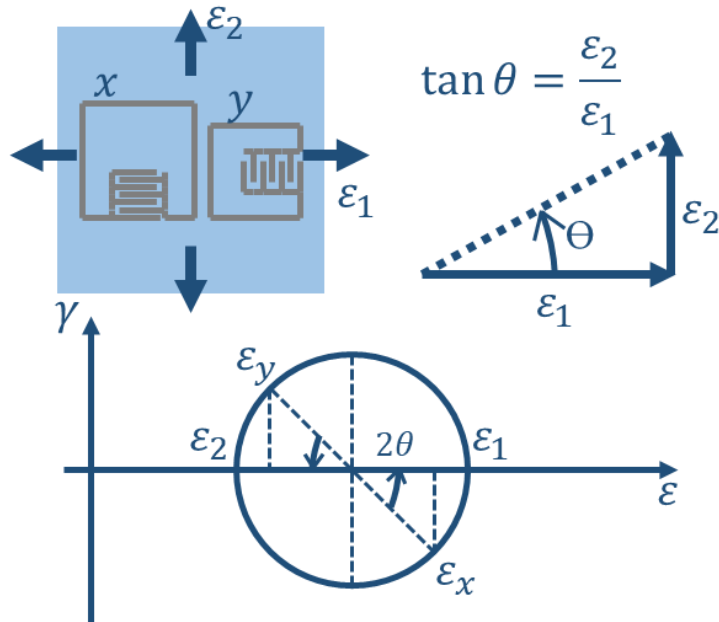


Figure 5.51. The schematic diagram of normal strain sensing in each direction explained by Mohr's circle

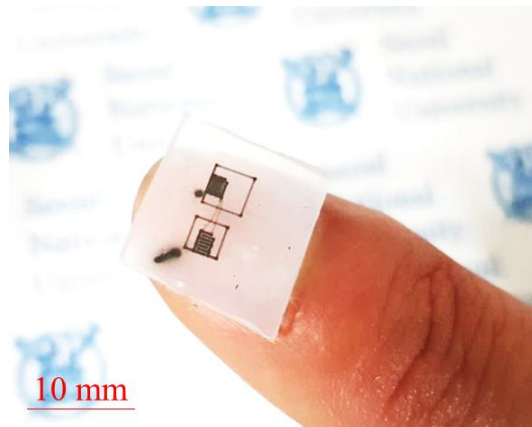


Figure 5.52. The photograph of fabricated normal strain sensor composed of two perpendicular resonance circuits

Using the one-directional characteristics of AFN printed RFID strain sensor, multi-directional RFID strain sensor was fabricated as shown in **figure 5.51**. The fabricated sensor patch has printed by two different RFID strain sensors with different design variable studied in above.

By regulation of finger gap, finger length, outer diameter, and turn width, a sensor patch composed of two different RFID strain sensors with two unique resonance frequencies was fabricated. Sensor **x** and **y** have $g = 250 \mu\text{m}$, $l = 800 \mu\text{m}$, $d = 2,400 \mu\text{m}$ and $g = 200 \mu\text{m}$, $l = 1,200 \mu\text{m}$, $d = 3,000 \mu\text{m}$, respectively. The resonance frequency for sensor **x** was about 1.35 GHz and resonance frequency for sensor **y** was about 1.7 GHz initially and two sensors were placed perpendicularly to separate into orthogonal strains.

Figure 5.52 shows the optical image of fabricated sample of multi-directional RFID normal strain sensor. Stretching in each direction was performed under the same condition using jig as discussed in above. The fabricated sensor patch was elongated in total 5 directions include θ equals to 0° , 30° , 45° , 60° , 90° as shown in **figures 5.53–5.57**.

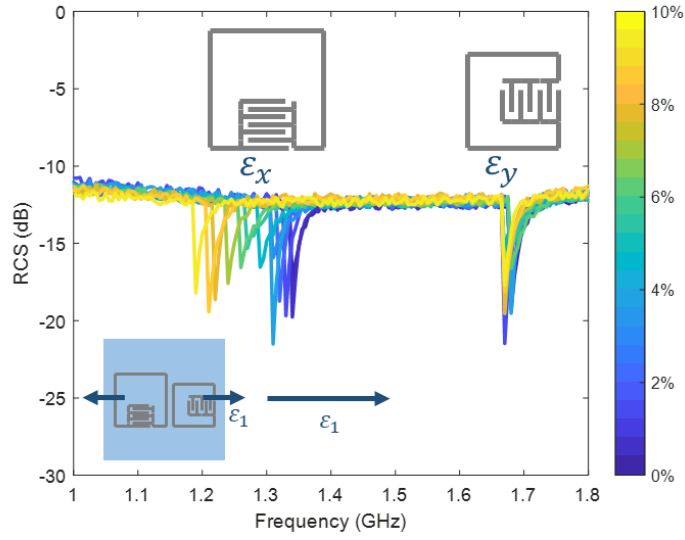


Figure 5.53. The experimental results of RCS spectrum of stretchable and wireless communication sensor for normal strain in horizontal direction

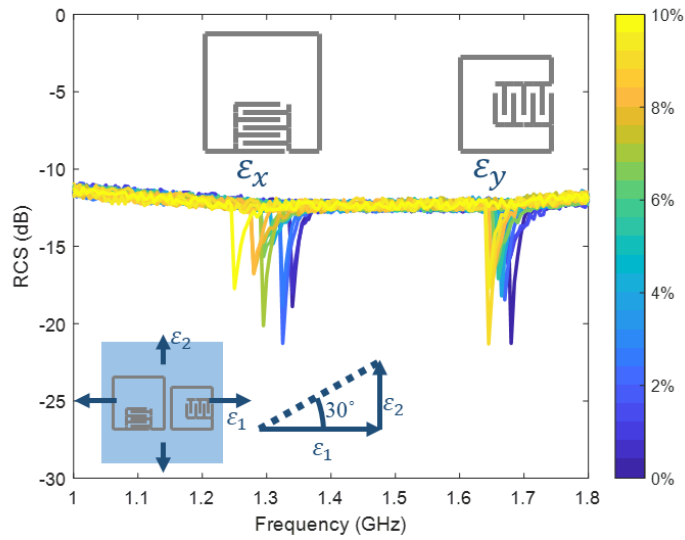


Figure 5.54. The experimental results of RCS spectrum of stretchable and wireless communication sensor for normal strain in 30 ° direction

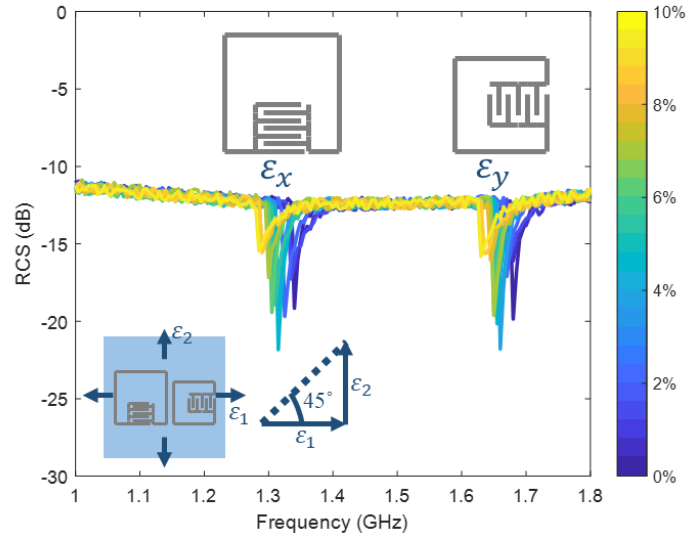


Figure 5.55. The experimental results of RCS spectrum of stretchable and wireless communication sensor for normal strain in 45 ° direction

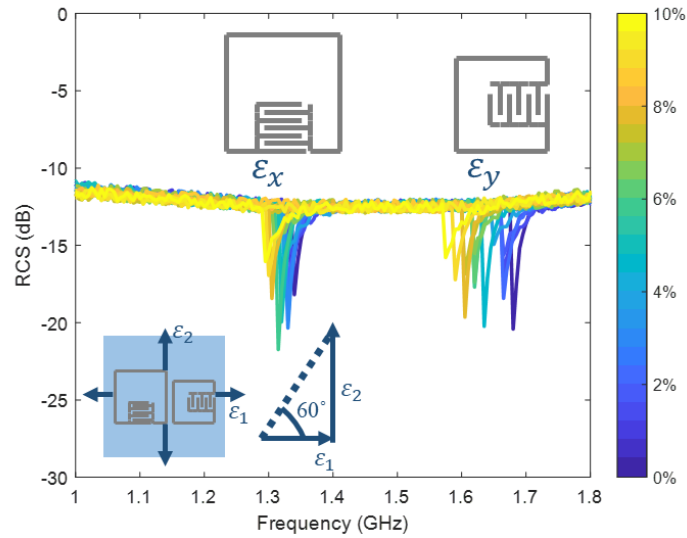


Figure 5.56. The experimental results of RCS spectrum of stretchable and wireless communication sensor for normal strain in 60 ° direction

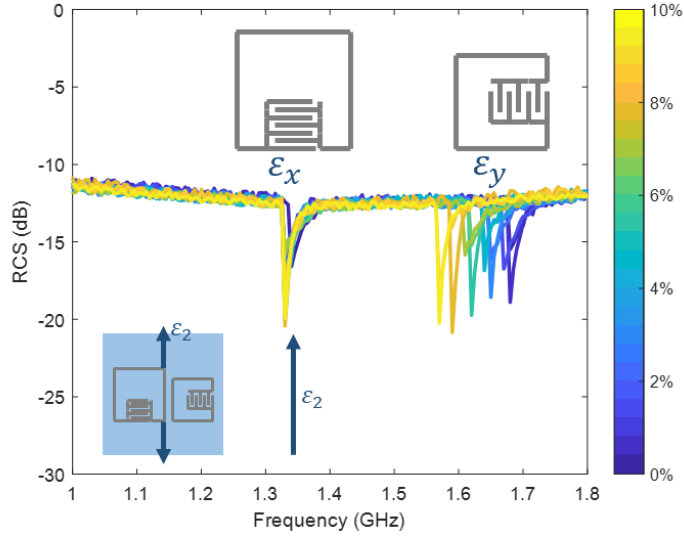


Figure 5.57. The experimental results of RCS spectrum of stretchable and wireless communication sensor for normal strain in vertical direction

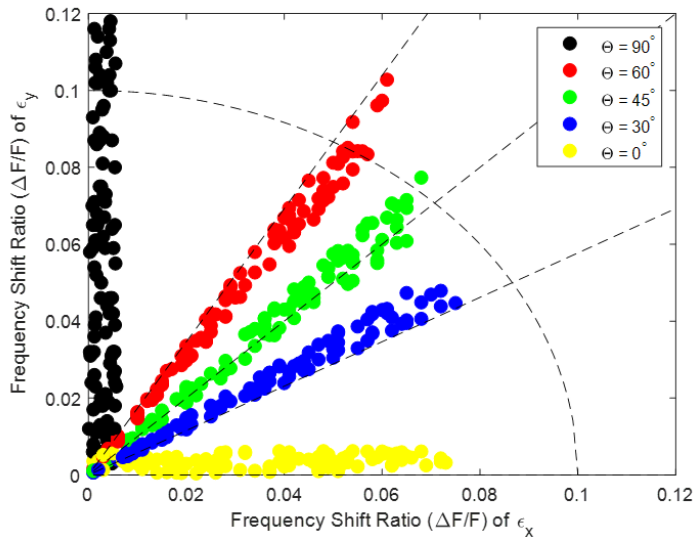


Figure 5.58. The experimental results of frequency shift ratio of stretchable and wireless communication sensor by normal strain

The fabricated sensor patch exhibited that only one of the two resonance frequencies decreased and the others were unchanged. In terms of 45 ° of elongation, both of the sensors responded to strain and the resonance frequencies decreased to about half of the intensity in comparison to one direction strain. Likewise, in the case of 30 ° and 60 ° of elongation, resonance frequency of one sensor decreased more than the other and it was able to estimate the direction of strain. To calibrate experimental results with actual induced strain, frequency shift ratio of each direction was calculated as shown in **equations 5.17** and **5.18**.

$$\varepsilon_x = \frac{f_x - f_{x,initial}}{f_{x,initial}} \quad \text{Equation 5.17}$$

$$\varepsilon_y = \frac{f_y - f_{y,initial}}{f_{y,initial}} \quad \text{Equation 5.18}$$

In this dissertation, frequency shift ratio of each RFID sensor was defined as a strain indicator of strain in each direction. The frequency at which no applied strain was assumed to be the initial frequency. **Figure 5.58** shows a plot of the strain indicator by gradually stretching the RFID sensor. Normal strain plot derived by fabricated RFID sensor usually matched well with the theoretical value of actual strain plot. Hence, it was well demonstrated that by using only one RFID strain sensor patch, not only the scale of strain on the two-dimensional plane but also the direction of strain could be measured at once.

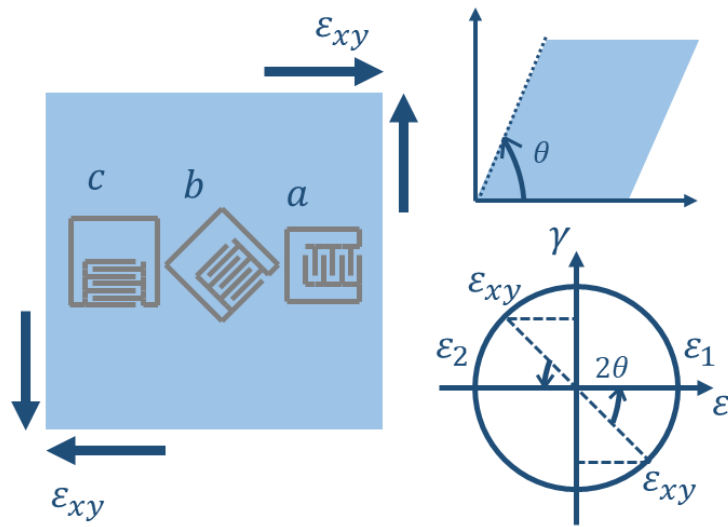


Figure 5.59. The schematic diagram of shear strain sensing in each direction explained by Mohr's circle

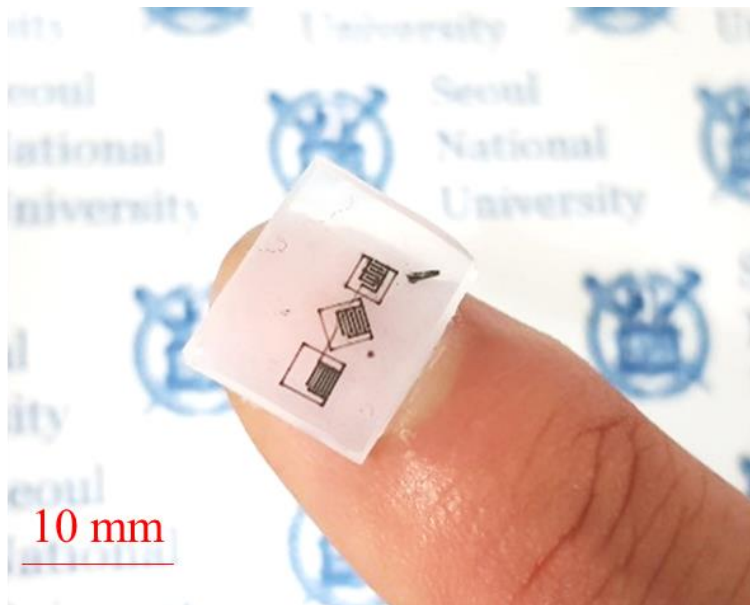


Figure 5.60. The photograph of fabricated shear strain sensor composed of three resonance circuits

In order to measure shear strain using fabricated RFID strain sensor, a similar design to the commercial rosette strain gauge was designed as shown in **figure 5.60** with three different strain sensors placed to resonate at different frequencies at angles of 0° , 45° , 90° . In the case of sensor **a**, it has $g = 250 \mu\text{m}$, $l = 800 \mu\text{m}$, and $d = 2,000 \mu\text{m}$. Sensor **b** and **c** have $g = 225 \mu\text{m}$, $l = 1,200 \mu\text{m}$, $d = 2,200 \mu\text{m}$ and $g = 200 \mu\text{m}$, $l = 1,400 \mu\text{m}$, $d = 2,400 \mu\text{m}$ respectively. Therefore, three different resonance frequencies of 1.55 GHz, 1.45 GHz, and 1.28GHz was achieved initially by sensor **a**, **b**, and **c**. Similar to the experiment conducted in above, the shear strain was applied in various directions using fabricated jig. **Figures 5.61–5.63** shows the experimental results for RCS spectra by shear strain with θ equals to 45° , 60° , 75° , respectively.

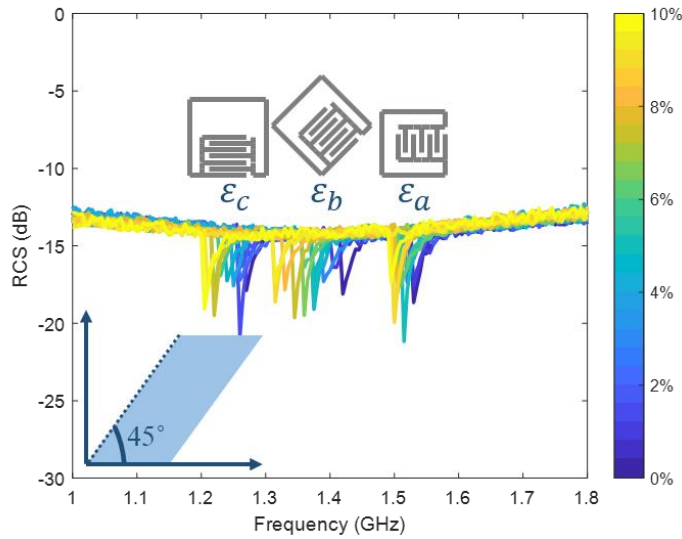


Figure 5.61. The experimental results of RCS spectrum of stretchable and wireless communication sensor for shear strain in 45° direction

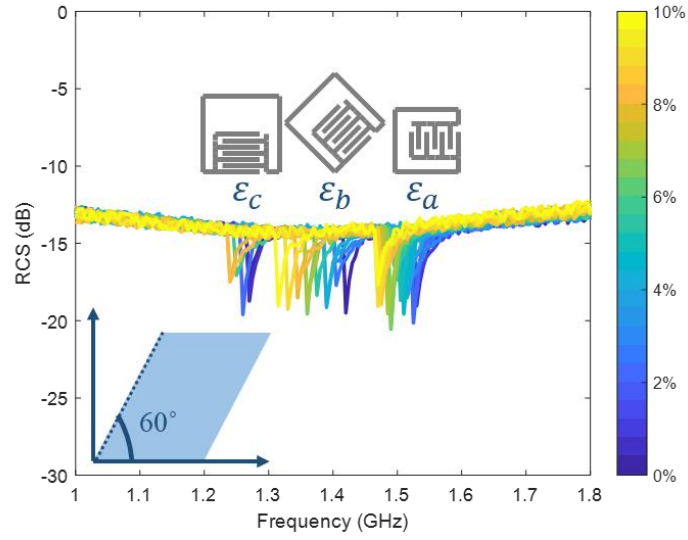


Figure 5.62. The experimental results of RCS spectrum of stretchable and wireless communication sensor for shear strain in 60 ° direction

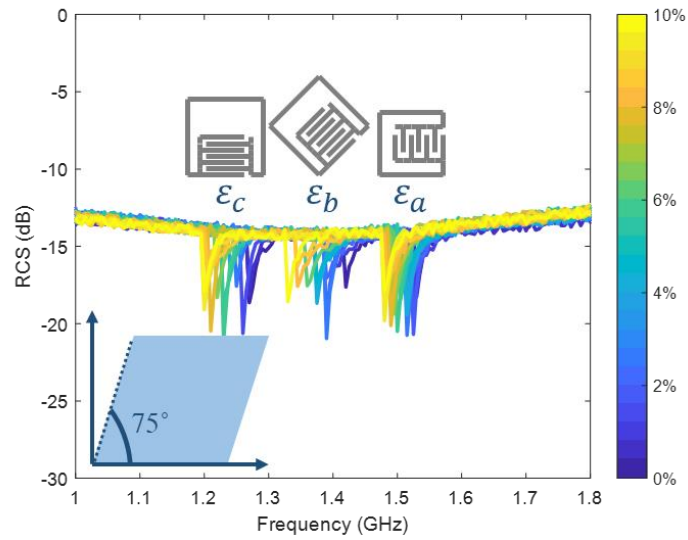


Figure 5.63. The experimental results of RCS spectrum of stretchable and wireless communication sensor for shear strain in 75 ° direction

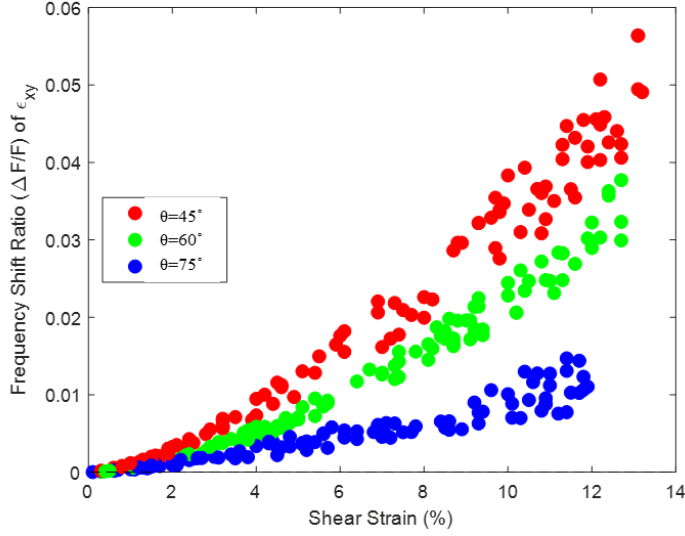


Figure 5.64. The experimental results of frequency shift ratio of stretchable and wireless communication sensor by shear strain

Unlike the experimental results of normal strain, frequency shift ratio of sensor **b** was larger than sensor **a** and **c** when the shear strain was induced. Furthermore, resonance frequency of sensor **b** changed more greatly as the angle of the shear strain increases. **Figure 5.64** shows shear strain plot measure by fabricated RFID strain sensor. The frequency shift ratio was used as an indicator of the actual strain and was calculated in the same way as previous experiment. The value of shear strain was obtained as **equation 5.19** as in the case of a typical rosette strain gauge in which three sensors were arranged at an angle of 45° .

$$\varepsilon_{xy} = \varepsilon_b - \frac{\varepsilon_a + \varepsilon_c}{2} \quad \text{Equation 5.19}$$

It was confirmed that the shear strain indicator increased with the angle and the size of shear strain. As in the case of using as a normal strain sensor, measured signal could be separated and recognised according to the shear angle.

Since AFN printed strain sensors are low-cost wireless communication sensors suitable for large strain measurements, their usage in soft and flexible manufacturing equipment or related applications is appropriate. To verify its possibilities of usage for large-scale production process that produces soft and flexible equipment, its performance was demonstrated by printing sensor onto the surface of air tube. The RFID strain sensor was printed on a commercial rubber air tube and confirmed that the sensor could measure the strain as the air tube was blowing. **Figure 5.65** shows the schematic diagram of RFID strain sensor to measure air in and out of the air tube. The printed RFID sensor onto the air tube is shown in **figure 5.66**. Since the rubber is also a type of polymer with similar physical properties to those used for this dissertation, printing the nanocomposite was available with a certain level of pre-tension to flatten the surface. As shown in **figure 5.67**, the resonance frequency decreased with the air tube swelled by air flow. In general, the inflated air tube had a similar physical role to the increased strain of the sensor which reduced resonance frequency as in the above experiments. Hence, it was demonstrated that AFN printed strain sensor could be used in the manufacturing process of flexible products including soft actuators and pneumatic process.

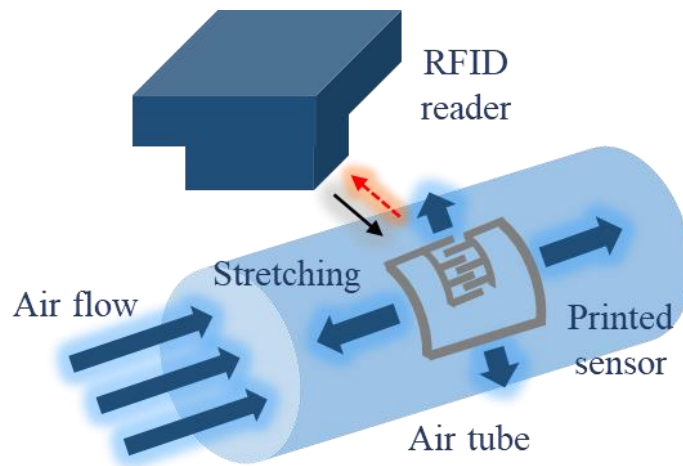


Figure 5.65. The schematic diagram of strain measurement of air tube by stretchable and wireless communication sensor



Figure 5.66. The photograph of printed stretchable and wireless communication sensor onto air tube

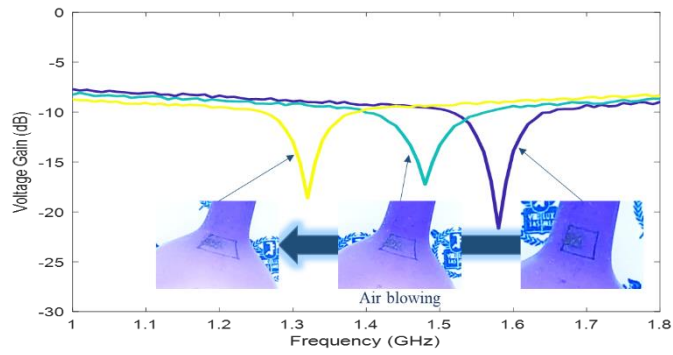


Figure 5.67. The experimental results of RCS spectrum of stretchable and wireless communication sensor by air blowing of air tube

Chapter 6. Conclusion

Complex manufacturing processes with particularly high quality requirements can benefit enormously from a detailed knowledge of all existing data and from the resulting insights into influencing factors and variables. Analyses of large data volumes can serve to convert information into predictive models, which then allow the configuration of processes within a range of optimum parameters. These ranges are customarily defined to lie safely within the specification limits while, at the same time, allowing high yields. A specific time and place must be recorded for each set of sensor data about default process parameters, the temperature in the hall or machine vibrations.

The shifting development of smart sensor has allowed companies to employ designers and engineers who live and breathe the subtleties of local requirement. When industries design manufacturing systems for sensor-enabled smart operation, they need to balance costs, flexibility, and the ability to adopt standard methods and practices across their worldwide operations. Manufacturing industry must make the most of the additional agility inherent in their production systems with lower personnel and operation costs to let them adopt more labour intensive methods.

This dissertation focused on the sensor as an enabler of digitised manufacturing systems with unattended and remote production. Since several researches have been reported nanomaterial for high quality

sensor fabrication, highly sensitive and wide measuring sensor was fabricated using AFN printing system. Distinguished from existing nanomaterials based strain sensors, it was possible to be fabricated by dry and direct printing method without chemical process using successive repetition of excitation and purging of aerosol. Moreover, porous properties of conductive patterns fabricated by AFN printing system overcame the challenge of high sensitivity of current strain sensor. However, generated mechanical cracks after strain exceeded a specific level decreased a measurable range and mechanical durability of sensor for industrial usage.

To expand the maximum strain limit of the sensor, the nanocomposite based on AgNPs and MWCNTs was printed on flexible and stretchable substrate. The printing mechanism in order of mechanical crack generation, seed layer deposition, partial aggregation, and fully deposition was demonstrated. Fabricated sensitive and wide measuring sensor exhibited GF of 58.7 and maximum strain limit of 74% with high mechanical stability during 1,000 times loading and unloading life cycle test. Furthermore, relative mass of AgNPs and MWCNTs and scan time of AFN printing process were used as process parameters for independent control of sensitivity and measurable range.

Using highly sensitive properties occurred by electron tunnelling effect, vibration measurement was also available. The performance of vibration measurement using vibration shaker was validated according to the vibration frequency and amplitude. Moreover,

frequency response of printed sensor according to induced frequency was demonstrated with Q-factor evaluation methods. Finally, independency of strain and vibration measurement was demonstrated by statistical methods.

For industrial usage of printed sensor, environmental validation and industrial analysis are required. This dissertation covers not only the XRD and DSC measurement for chemical characterisation of sensor but also the temperature and humidity characterisation for the validation in various environments that sensor would face in real industry. Furthermore, cost evaluation based cost-based pricing method was also conducted followed by low-cost smart sensor evaluation with indicators including essential, affordable, simple and interoperable properties.

Sensing mechanism of fabricated sensor heavily depended on electron tunnelling effect between nanomaterials. By basic assumptions that the electrical conductivity of nanocomposite was usually dominated by mechanical attachment among nanomaterials, statistical regression analysis of fabricated nanocomposite sensors was conducted using bivariate probit model. Suggested model was validated by comparison to empirical values according to composition ratio and packing ratio of printed pattern.

For accurate and versatile analysis, novel simulation method for nanocomposite strain sensor was proposed. Distinguished from existing simulation methods for strain sensor, developed method could simulate and estimate the electrical conductivity of

nanocomposite in dynamically changing condition with lower simulation cost. First, the distribution of nanocomposite was optimised using LJ potential mode to assume the actual distribution of AFN printed nanocomposite. Then, adjustment of boundary condition and repetition were conducted for the simulation of strain increase. By just counting the average attachment among nanomaterials using the voter model, it was available to estimate the change of electrical conductivity of nanocomposite. The simulation method was also validated by comparison to empirical values according to composition ratio and packing ratio.

Following the trends to the smart and intelligent manufacturing technology, the importance of process monitoring has been increased in various engineering fields. Among them, the forming and milling process are most widely used conventional machining process and expected as the most potential field along the digitization of manufacturing due to their high requirements of quality. This dissertation covers the measurement of force and vibration with low-cost and easy-to-use manner which are difficult to measure in terms of sensor cost and installation method.

Using Poisson's ratio of the stamp composed of elastic metal, the forming force from the mechanical deformation of the stamp was calculated. This dissertation compared the relative resistance change obtained by directly printed sensor with actual force obtained by commercial dynamometer in rubber forming process according to maximum force, force gradient, and sheet metal thickness. The

sensor values and actual force exhibited similar behaviour which means that printed sensor could replace the commercial dynamometer with lower production and labour cost.

To monitor milling process, comparison of directly printed sensor to commercial vibration sensor in milling process was conducted by attaching both to the workpiece. The relative resistance change of directly printed sensor also exhibited similar signal to actual vibration measured by commercial vibration sensor with low manufacturing and operation cost. Furthermore, an experiment comparing with the commercial vibration sensor was performed according to various process parameters such as RPM, feed rate, cutting depth, and cutting side. The peak frequency increased as RPM increased while power intensity was remained. In terms of feed rate, cutting depth, and cutting side, the intensity of the vibration increased at the same frequency due to the increase of cutting force as each process parameter increased. Finally, directly printed sensor was applied to turbine blade milling process which is highly susceptible to vibration. Using the vibration data obtained by attached sensor on turbine blades with good and poor surface quality, surface defect during milling process was predicted in real time.

Other technological limitations have lied in the connection and communication manner. Since most of passive strain sensors directly measure their electrical properties include resistance and capacitance varied by strain, soldering and wiring process is needed for actual usage. However, electrical wires usually limit the usability

of strain sensors and even increase the noise of the measured electrical signal which induces inaccurate information. To overcome the limitation, RFID technology is widely used for wireless communication strain sensors. Specifically, chipless RFID technology offers several advantages over the chipped RFID in terms of cost, simplicity, printability, and ability to operate in high-temperature environments.

This dissertation focused on the LC resonance-based chipless RFID printing using AFN printing system for stretchable and wireless communication sensor development which encodes the information using only the antenna by oscillation of LC circuit. Fabricated stretchable and wireless communication sensor was able to realise motion with a high degree-of-freedom including stretching, twisting, and folding. According to experimental results, resonance frequency was controlled by process parametrisation of AFN printing process including the gap of finger capacitor, the length of finger capacitor, outer diameter, and turn width. Moreover, AgNPs enhanced MWCNTs conductive networks of conductive patterns printed onto PDMS substrate expanded the maximum strain over 20% and GF over 0.5.

Using the characteristics of AFN printed RFID strain sensor which was capable of measuring only one direction independently, strain sensor has been developed that can measure all direction and intensities of a strain in a two-dimensional plane. Furthermore, using similar design with commercial rosette strain gauge, shear strain was

also measured by AFN printed RFID strain sensor. Finally, RFID strain sensors had printed onto air tube to verify the possibilities for applications to pneumatic process.

Low-cost smart sensor expects various return in various ways. They enables high production yield, OEE gain, labour cost reduction, less amorisation, and lowered CAPEX. Here, directly printed sensor was developed which can be applied to the digital twin for various manufacturing process with low manufacturing cost and easy-to-use manner. The process monitoring and predictive maintenance enabled by developed sensor could increase the operation cash flow and decrease the investing cash flow which would have a direct impact on manufacturing industry.

Low-cost smart sensor is also affecting unprecedented business models including wearable or skin-mountable devices, soft robotics, and human-machine interfaces (HMI). It is expected that digitalized, networked, and user-friendly manufacturing would be enabled by printed sensor from process and supply chains to all over the manufacturing industry.

Bibliography

1. Wagner, T., Hermann, C., and Thiede, S., *Industry 4.0 impacts on lean production systems*, Procedia CIRP, 2017, **63**: 125–131.
2. Wee, D., et al., *Industry 4.0—how to navigate digitization of the manufacturing sector*, McKinsey & Company, 2015, **58**.
3. Baur, C. and Wee, D., *Manufacturing's next act*, McKinsey & Company, 2015, **6**.
4. Löffler, M., and Tschiesner, A., *The Internet of Things and the future of manufacturing*, McKinsey & Company, 2013, **4**.
5. Lanza, G., Haefner, B., and Kraemer, A., *Optimization of selective assembly and adaptive manufacturing by means of cyber—physical system based matching*, CIRP Annals, 2015, **64**(1): 399–402.
6. Jeschke, S., et al., *Industrial internet of things and cyber manufacturing systems*, Industrial Internet of Things, 2017, pp. 3–19.
7. Stark, R., Kind, S., and Neumeyer, S., *Innovations in digital modelling for next generation manufacturing system design*, CIRP Annals, 2017, **66**(1): 169–172.
8. Monostori, L., et al., *Cyber—physical systems in manufacturing*, CIRP Annals, 2016, **65**(2): 621–641.
9. Lee, J., Bagheri, B., and Kao, H. A., *A cyber—physical systems architecture for industry 4.0—based manufacturing systems*,

- Manufacturing letters, 2015, **3**: 18–23.
10. Wu, D., et al., *Cloud-based manufacturing: old wine in new bottles?*, Procedia CIRP, 2014, **17**: 94–99.
 11. Zou, J., et al., *Production system performance identification using sensor data*, IEEE Transactions on Systems, Man, and Cybernetics: Systems, 2016, **48**(2): 255–264.
 12. He, Q. P., and Wang, J., *Statistical process monitoring as a big data analytics tool for smart manufacturing*, Journal of Process Control, 2018, **67**: 35–43.
 13. Möhring, H. C., Litwinski, K. M., and Gümmer, O., *Process monitoring with sensory machine tool components*, CIRP Annals, 2010, **59**(1): 383–386.
 14. Yun, H. T., et al., *Ploughing detection in micromilling processes using the cutting force signal*, International Journal of Machine Tools and Manufacture, 2011, **51**(5): 377–382.
 15. Tao, F., et al., *Digital twin-driven product design, manufacturing and service with big data*, The International Journal of Advanced Manufacturing Technology, 2018, **94**(9–12): 3563–3576.
 16. Schleich, B., et al., *Shaping the digital twin for design and production engineering*, CIRP Annals, **66**(1): 141–144.
 17. Müller, E., and Hopf, H., *Competence center for the digital transformation in small and medium-sized enterprises*, Procedia CIRP, 2017, **11**:1495–1500.
 18. Bär, K., Herbert-Hansen, Z. N. L., and Khalid, W.,

- Considering Industry 4.0 aspects in the supply chain for an SME*, Production Engineering, 2018, **12**(6): 747–758.
19. Bill, S., and Raymond, L., *Information technology: Threats and opportunities for SMEs*, International Journal of Information Management, 1993, **13**(6): 439–448.
 20. Moeuf, A., et al., *Identification of critical success factors, risks and opportunities of Industry 4.0 in SMEs*, International Journal of Production Research, 2020, **58**(5): 1384–1400.
 21. Chesney, M. and Scott, L., *Pricing European currency options: A comparison of the modified Black–Scholes model and a random variance model*, Journal of Financial and Quantitative Analysis, 1989, **24**(3): 267–284.
 22. Lauterbach, B., Schultz, P., *Pricing warrants: an empirical study of the Black–Scholes model and its alternatives*, The Journal of Finance, 1990, **45**(4): 1181–1209.
 23. Panizzolo, R., et al., *Lean manufacturing in developing countries: evidence from Indian SMEs*, Production Planning & Control, 2012, **23**(10–11): 769–788
 24. Kleindienst, M., and Ramsauer, C., *SMEs and Industry 4.0–Introducing a KPI based Procedure Model to identify Focus Areas in Manufacturing Industry*, Athens Journal of Business and Economics, 2016, **2**: 109–122.
 25. Durlauf, S. N., Kourtellos, A., and Minkin, A., *The local Solow growth model*, European Economic Review, 2001, **45**(4–6): 928–940.

26. Lee, K., Pesaran, M. H., and Smith, R., *Growth and convergence in a multi-country empirical stochastic Solow model*, Journal of applied Econometrics, 1997, **12**(4): 357–392.
27. Drossel, W.G., et al., *Performance of a new piezoceramic thick film sensor for measurement and control of cutting forces during milling*, CIRP Annals, 2018, **67**(1): 45–48.
28. Nguyen, V., Fernandez–Zelaia, P., and Melkote, S. N., *PVDF sensor based characterization of chip segmentation in cutting of Ti–6Al–4V alloy*, CIRP Annals, 2017, **66**(1): 73–76.
29. Huang, C. T., et al., *A wearable yarn–based piezo–resistive sensor*, Sensors and Actuators A: Physical, 2008, **141**(2): 396–403.
30. Lee, G. Y., et al., *Highly Sensitive Solvent–free Silver Nanoparticle Strain Sensors with Tunable Sensitivity Created using an Aerodynamically Focused Nanoparticle (AFN) Printer*, ACS applied materials and interfaces, 2019, **11**(29): 26421–26432.
31. Sangeetha, N. M., et al., *Nanoparticle–Based Strain Gauges Fabricated by Conductive Self Assembly: Strain Sensitivity and Hysteresis with Respect to Nanoparticle Sizes*, The Journal of Physical Chemistry C, 2013, **117**: 1935–1940.
32. Yi, L., et al., *Nanoparticle monolayer–based flexible strain gauge with ultrafast dynamic response for acoustic vibration detection*, Nano Research, 2015, **8**(9): 2978–2987.

33. Jeong, Y. R., et al., *Highly stretchable and sensitive strain sensors using fragmentized graphene foam*. Advanced Functional Materials, 2015, **25**(27): 4228–4236.
34. Kong, J. H., et al., Simple and rapid micropatterning of conductive carbon composites and its application to elastic strain sensors, Carbon, 2014, **77**:199–207.
35. Amjadi, M., et al., *Highly Stretchable and Sensitive Strain Sensor Based on Silver Nanowire – Elastomer Nanocomposite*, ACS Nano, 2014, **8**(5): 5154–5163.
36. Yao, S., and Zhu, Y., *Wearable multifunctional sensors using printed stretchable conductors made of silver nanowires*, Nanoscale, 2014, **6**(4): 2345–2352.
37. Hwang, B. U., et al., *Transparent stretchable self-powered patchable sensor platform with ultrasensitive recognition of human activities*, ACS Nano, 2015, **9**(9): 8801–8810.
38. Shin, U. H., et al., *Highly stretchable conductors and piezocapacitive strain gauges based on simple contact-transfer patterning of carbon nanotube forests*, Carbon, 2014, **80**: 396–404.
39. Liao, X., et al., A Highly stretchable ZnO@ Fiber-Based Multifunctional Nanosensor for Strain/Temperature/UV Detection, Advanced Functional Materials, 2016, **26**(18): 3074–3081.
40. Cai, L., et al., *Super-stretchable, Transparent Carbon Nanotube-Based Capacitive Strain Sensors for Human Motion*

- Detection*, Scientific Reports, 2013, **3**: 3048.
41. Amjadi, M., Yoon, Y. J., and Park, I., *Ultra-stretchable and skin-mountable strain sensors using carbon nanotubes-Ecoflex nanocomposite*, Nanotechnology, 2015, **26**: 375501
 42. Boland, C. S., et al., *Sensitive, high-strain, high-rate bodily motion sensors based on graphene-rubber composites*, ACS Nano, 2014, **8**(9): 8819–8830.
 43. Fan, W., Bu, W., and Shi, J., *On the Latest Three-Stage Development of Nanomedicines based on Upconversion Nanoparticles*, Advanced Materials, 2016, **28**(21): 3987–4011.
 44. Kim, D.H., et al., *Inorganic semiconductor nanomaterial for flexible and stretchable bio-integrate electronics*, NPG Asia Materials, 2012, **4**(4): e15.
 45. Liu, Y., Pharr, M., and Salvatore, G. A., *Lab-on-skin: a review of flexible and stretchable electronics for wearable health monitoring*, ACS Nano, 2017, **11**(10), 9614–9635.
 46. Kim, D. H., and Rogers, J. A., *Stretchable electronics: materials strategies and devices*, Advanced Materials, 2008, **20**(24): 4887–4892.
 47. Rogers, J. A., Someya, T., and Huang, Y., *Materials and mechanics for stretchable electronics*, Science, 2010, **327**(5973): 1603–1607.
 48. Trung, T. Q., and Lee, N. E., *Flexible and stretchable physical sensor integrated platforms for wearable human-activity*

- monitoring and personal healthcare*, Advanced Materials, 2016, **28**(22): 4338–4372.
49. Kim, H. J., et al., *Rubbery electronics and sensors from intrinsically stretchable elastomeric composites of semiconductors and conductors*, Science Advances, 2017, **3**: e1701114.
50. Qi, K., et al., *A Highly Stretchable Nanofiber-Based Electronic Skin with Pressure-, Strain-, and Flexion-Sensitive Properties for Health and Motion Monitoring*, ACS Applied Materials and Interfaces, 2017, **9**: 42951–42960.
51. Lee, J., et al., *A stretchable strain sensor based on a metal nanoparticle thin film for human motion detection*, Nanoscale, 2014, **6**: 11932.
52. Liu, Z., et al., *Surface Strain Redistribution on Structured Microfibers to Enhance Sensitivity of Fiber-Shaped Stretchable Strain Sensors*, Advanced Materials, 2018, **30**: 1704229.
53. Pang, C., et al., *A flexible and highly sensitive strain-gauge sensor using reversible interlocking of nanofiber*, Nature Materials, 2012, **11**: 795–801.
54. Gong, S., et al., *Tattolike Polyaniline Microparticle-Doped Gold Nanowire Patches as Highly Durable Wearable Sensors*, ACS Applied Materials and Interfaces, 2015, **7**: 19700–19708.
55. Amjadi, M., et al., *Stretchable, Skin-Mountable, and Wearable Strain Sensors and Their Potential Applications: A*

- Review*, Advanced Functional Materials, 2016, **26**: 1678–1698.
56. Puyoo, E., et al., *Metallic nanoparticle–based strain sensors elaborated by atomic layer deposition*, Applied Physics Letters, 2017, **110**: 123103.
 57. Lee, S., et al., *Metal microparticle – Polymer composites as printable, bio/ecoresorbable conductive inks*, Materials Today, 2018, **21**(3): 207–215.
 58. Hermann, J., et al., *Nanoparticle films as sensitive strain gauges*, Applied Physics Letters, 2007, **91**: 183105.
 59. Suzuki, K., et al., *Rapid–response, widely stretchable sensor of aligned MWCNT/elastomer composites for human motion detection*, ACS Sensors, 2016, **1**(6): 817–825.
 60. Mohammed, M. G., and Kramer, R., *All–Printed Flexible and Stretchable Electronics*, Advanced Materials, 2017, **29**(19): 1604965.
 61. Sekitani, T., et al., *Stretchable active–matrix organic light–emitting diode display using printable elastic conductors*, Nature Materials, 2009, **8**(6): 494.
 62. Takei, K., et al., *Highly sensitive electronic whiskers based on patterned carbon nanotube and silver nanoparticle composite films*, Proceedings of the National Academy of Sciences of the United States of America, 2014, **111**(5): 1703–1707.
 63. Shi, J., et al., *Graphene Reinforced Carbon Nanotube*

- Networks for Wearable Strain Sensors*, Advanced Functional Materials, 2016, **26**: 2078, 2084.
64. Yamada, T., et al., *A stretchable carbon nanotube strain sensor for human-motion detection*, Nature Nanotechnology, 2011, **6**: 296–301.
 65. Ryu, S., et al., *Extremely Elastic Wearable Carbon Nanotube Fiber Strain Sensor for Monitoring of Human Motion*, ACS Nano, 2015, **9**(6): 5929–5936.
 66. Roh, E., et al., *Stretchable, Transparent, Ultrasensitive, and Patchable Strain Sensor for Human-Machine Interfaces Comprising a Nanohybrid of Carbon Nanotubes and Conductive Elastomers*, ACS Nano, 2015, **9**(6): 6252–6261.
 67. Lee, G. Y., et al., *Aerodynamically Focused Nanoparticle (AFN) Printing: Novel Direct Printing Technique of Solvent-Free and Inorganic Nanoparticles*, ACS Applied Materials and Interfaces, 2014, **6**: 16466–16471.
 68. Rahimi, R., et al., *Highly Stretchable and Sensitive Unidirectional Strain Sensor via Laser Carbonization*, ACS Applied Materials and Interfaces, 2015, **7**: 4463–4470.
 69. Lee, G. Y., *Multi-material direct printing by Pulsed-Nano Particle Deposition System (P-NPDS)*, in *School of Mechanical and Aerospace Engineering, Ph. D. Thesis*, 2013, Seoul National University.
 70. Hanft, D., et al., *An overview of the aerosol deposition method; process fundamentals and new trends in materials*

- applications*, Journal of Ceramic Science and Technology, 2015, **6**(3): 147–182.
71. Stoltenhoff, T., Kreye, H., and Richter, H. J., *An analysis of the cold spray process and its coating*, Journal of Thermal Spray Technology, 2002, **11**(4): 542–550.
 72. Chun, D. M., et al., *Nano-particle deposition system (NPDS): Low energy solvent-free dry spray process for direct patterning of metals and ceramics at room temperature*, International Journal of Precision Engineering and Manufacturing, 2012, **13**(7): 1107–1112.
 73. Dykhuizen, R. C., Smith, M. F., *Gas dynamic principles of cold spray*, Journal of Thermal Spray Technology, 1998, **7**(2): 205–212.
 74. Min, S. H., Lee, G. Y., and Ahn, S. H., *Direct printing of highly sensitive, stretchable, and durable strain sensor based on silver nanoparticles/multi-walled carbon nanotubes composites*, Composites Part B: Engineering, 2019, **161**: 395–401.
 75. Kim, C. S., *Nanoscale 3D printing process using nano particle deposition system and focused ion beam*, in *School of Mechanical and Aerospace Engineering, Ph. D. Thesis*, 2013, Seoul National University.
 76. Klinkov, S. V., Kosarev, V. F., and Rein, M., *Cold spray deposition: Significance of particle impact phenomena*, Aerospace Science and Technology, 2005, **9**(7): 582–591.

77. Chun, D. M., and Ahn, S. H., *Deposition Mechanism of Dry Sprayed Ceramic Particles at Room Temperature Using a Nano-Particle Deposition System (NPDS)*, Acta Materialia, 2011, **59**(7): 2693–2703.
78. Zhang, S., et al., *Highly stretchable, sensitive, and flexible strain sensors based on silver nanoparticles/carbon nanotubes composites*, Journal of Alloys and Compounds, 2015, **652**: 48–54.
79. Selesnick, I. W., *Wavelet transform with tunable Q-factor*, IEEE transactions on signal processing, 2011, **59**(8): 3560–3575.
80. Feir-Walsh, B. J., and Toothaker, L. E., *An empirical comparison of the ANOVA F-test, normal scores test and Kruskal-Wallis test under violation of assumption*, Education and Psychological Measurement, 1974, **34**(4): 789–799.
81. Westfall, P. H., and Young, S. S., *Resampling-based multiple testing: Examples and methods for p-value adjustment*, 1993, **279**.
82. Brown, J. D., *The Cronbach alpha reliability estimate*, JALT Testing & Evaluation SIG Newsletter, 2002, **6**(1)
83. Liu, W. Q., et al., *Novel piezoelectric bistable oscillator architecture for wideband vibration energy harvesting*, Smart Materials and Structures, 2013, **22**(3): 035013.
84. Roy, B. K., Chakraborty, S., and Mihsra, S. K., *Robust optimum design of base insulation system in seismic vibration*

- control of structures under uncertain bounded system parameters*, Journal of Vibration and Control, 2014, **20**(5): 786–800.
85. Speller, K. E., and Yu, D., *A low-noise MEMS accelerometer for unattended ground sensor applications*, Unattended/Unmanned Ground, Ocean, and Air Sensor Technologies and Application, 2004, **5417**.
 86. Chiu, Y., and Tseng, V. F., *A capacitive vibration-to-electricity energy converter with integrated mechanical switches*, Journal of Micromechanics and Microengineering, 2008, **18**(10): 104004.
 87. Gerfers, F., et al., *A 0.2–2 Gb/s 6x OSR receiver using a digitally self-adaptive equalizer*, IEEE Journal of Solid-State Circuits, 2008, **43**(6): 1436–1448.
 88. Yaghootkar, B., Azimi, S., and Bahreyni, B., *A high-performance piezoelectric vibration sensor*, IEEE Sensors Journal, 2017, **17**(13): 4005–4012.
 89. Stobinski, L., et al., *Graphene oxide and reduced graphene oxide studied by the XRD, TEM and electron spectroscopy methods*, Journal of Electron Spectroscopy and Related Phenomena, 2014, **195**: 145–154.
 90. Barton, J. M. *The application of differential scanning calorimetry (DSC) to the study of epoxy resin curing reactions*, Epoxy resins and composites, 1985, 111–154.
 91. Noel, M. D., *Edgeworth price cycles, cost-based pricing and*

- sticky pricing in retail gasoline markets*, The Review of Economic and Statistics, 2007, **89**(2): 324–334.
92. Meservey, R., and Tedrow, P. M., *Spin-polarized electron tunnelling*, *Physics Reports*, 1994, **238**(4): 173–243.
 93. BenDaniel, D. J., and Duke, C. B., *Space-charge effects on electron tunnelling*, *Physical review*, 1966, **152**(2): 683.
 94. Min, S. H., et al., *Simulation of electrical conductivity for nanoparticles and nanotubes composite sensor according to geometrical properties of nanomaterial*, *Composites Part B: Engineering*, 2019, **174**: 107003.
 95. Poirier, D. J., *Partial observability in bivariate probit models*, *Journal of econometrics*, 1980, **12**(2): 209–217.
 96. Meng, C. L., and Schmidt, P., *On the cost of partial observability in the bivariate probit model*, *International Economic Review*, 1985, 71–85.
 97. Detcheverry, F. A., et al., *Monte Carlo simulations of a coarse grain model for block copolymers and nanocomposite*, *Macromolecules*, 2008, **41**(13): 4989–5001.
 98. Song, J. H., et al., *Controlled kinetic Monte Carlo simulation of laser improved nano particle deposition process*, *Powder Technology*, 2018, **325**: 651–658.
 99. Djebara, Y., et al., *Modeling of the effect of particles size, particles distribution and particles number on mechanical properties of polymer-clay nano-composites: numerical homogenization versus experimental results*, *Composites Part*

- B: Engineering, 2016, **86**: 135–142.
100. Narayanunni, V., Gu, H., and Yu, C., *Monte Carlo simulation for investigating influence of junction and nanofiber properties on electrical conductivity of segregated–network nanocomposite*, Acta Materialia, 2011, **59**(11): 4548–4555.
101. Hackett, E., Manias, E., and Giannelis, E. P., *Computer simulation studies of PEO/layer silicate nanocomposite*, Chemistry of Materials, 2000, **12**(8): 2161–2167.
102. Spanos, P. D., and Kontsos, A., *A multiscale Monte Carlo finite element method for determining mechanical properties of polymer nanocomposite*, Probabilistic Engineering Mechanics, 2008, **23**(4): 456–470.
103. Li, T. I., et al., *Modeling the crystallization of spherical nucleic acid nanoparticle conjugates with molecular dynamics simulations*, Nano Letters, 2012, **12**(5): 2509–2514.
104. Jeng, M. S., et al., *Modeling the thermal conductivity and phonon transport in nanoparticle composites using Monte Carlo simulation*, Journal of Heat Transfer, 2008, **130**(4): 042410.
105. Lin, F., Xiang, Y., and Shen, H. S., *Temperature dependent mechanical properties of graphene reinforced polymer nanocomposite—a molecular dynamics simulation*, Composites Part B: Engineering, 2017, **111**: 261–269.
106. Liu, J., et al., *Nanoparticle dispersion and aggregation*

- in polymer nanocomposite: insights from molecular dynamics simulation*, Langmuir, 2011, **27**(12): 7926–7933.
107. Li, Y., et al., *Molecular dynamics simulations of tribology properties of NBR (Nitrile–Butadiene Rubber)/carbon nanotube composites*, Composites Part B: Engineering, 2016, **97**: 62–67.
 108. Heinz, H., et al., *Accurate simulation of surfaces and interfaces of face–centered cubic metals using 12–6 and 9–6 Lennard–Jones potentials*, The Journal of Physical Chemistry C, 2008, **112**(44): 17281–17290.
 109. Fu, S. P., et al., *Lennard–Jones type pair–potential method for coarse–grained lipid bilayer membrane simulations in LAMMPS*, Computer Physics Communications, 2017, **210**: 193–203.
 110. Lima, N. W., et al., *Molecular dynamics simulation of polymerlike thin films irradiated by fast ions: A comparison between FENE and Lennard–Jones potentials*, Physical Review B, 2016, **94**(19): 195417.
 111. Rutkai, G., et al., *How well does the Lennard–Jones potential represent the thermodynamic properties of noble gases?*, Molecular Physics, 2017, **115**(9–12): 1104–1121.
 112. Bramson, M., Cox, J. T., and Le Gall, J. F., *Super–Brownian limits of voter model clusters*, Annals of Probability, 2001, **29**(3): 1001–1032.
 113. Cox, J. T., and Klenke, A., *Recurrence and ergodicity*

- of interacting particle systems*, Probability Theory and Related Fields, 2000, **116**(2): 239–255.
114. Hu, R., and Durrett, R., *Latent voter model on locally tree-like random graphs*, Stochastic Processes and their Applications, 2018, **128**(5): 1590–1614.
115. Heislitz, F., et al., *Simulation of roll forming process with the 3-D FEM code PAM-STAMP*, Journal of Materials Processing Technology, 1996, **59**(1–2): 59–67.
116. Elyasi, M., Ghadikolaee, H. T., and Hosseinzadeh, M., *Fabrication of metallic bipolar plates in PEM fuel cell using semi-stamp rubber forming process*, The International Journal of Advanced Manufacturing Technology, 2017, **92**(1–4): 765–776.
117. Liu, Y., and Hua, L., *Fabrication of metallic bipolar plate for proton exchange membrane fuel cells by rubber pad forming*, Journal of Power Sources, 2010, **195**: 3529–3535.
118. Hong, Y. S., et al., *Tool-wear monitoring during micro-end milling using wavelet packet transform and Fisher's linear discriminant*, International Journal of Precision Engineering and Manufacturing, 2016, **17**(7): 845–855.
119. Marinescu, I., and Axinte, D. A., *A critical analysis of effectiveness of acoustic emission signals to detect tool and workpiece malfunctions in milling operations*, International Journal of Machine Tools and Manufacture, 2008, **48**(10): 1148–1160.

120. Lee, J. Y., et al., *A simplified machine-tool power consumption measurement procedure and methodology for estimating total energy consumption*, Journal of Manufacturing Science and Engineering, 2016, **138**(5): 051004.
121. Domdouzis, K., Kumar, B., and Anumba, C., *Radio-Frequency Identification (RFID) applications: A brief introduction*, Advanced Engineering Informatics, 2007, **21**(4): 350–355.
122. Occhiuzzi, C., Cippitelli, S., and Marrocco, G., *Modelling, design and experimentation of wearable RFID sensor tag*, IEEE Transactions on Antennas and Propagation, 2010, **58**(8): 2490–2498.
123. Catarinucci, L., Colella, R., and Tarricone, L., *Enhanced UHF RFID sensor-tag*, IEEE Microwave and Wireless Components Letters, 2013, **23**(1): 49–51.
124. Preradovic, S., and Karmakar, N. C., *Chipless RFID: Bar code of the future*, IEEE Microwave Magazine, 2010, **11**(7): 87–97.
125. Zhang, J., et al., *A review of passive RFID tag antenna-based sensors and systems for structural health monitoring applications*, Sensors, 2017, **17**(2): 265.
126. Marindra, A. M. J., and Yian, G. Y., *Chipless RFID Sensor Tag for Metal Crack Detection and Characterization*, IEEE Transactions on Microwave Theory and Techniques, 2018, **66**(5): 2452–2462.

127. Shao, B., et al., *Chipless RFID tags fabricated by fully printing of metallic inks*, Annals of Telecommunications, 2013, **68**: 401–413.
128. Shrestha, S., et al., *A chipless RFID sensor system for cyber centric monitoring applications*, IEEE Transactions on Microwave Theory and Techniques, 2009, **57**(5): 1303–1309.
129. Vena, A., Perret, E., and Tedjini, S., *High-capacity chipless RFID tag intensive to the polarization*, IEEE Transactions on Antennas and Propagation, 2012, **60**(1): 4509–4515.
130. Lu, H. M., et al., *MEMS-based inductively coupled RFID transponder for implantable wireless sensor applications*, IEEE Transactions on Magnetics, 2007, **43**(6): 2412–2414.
131. Vena, A., Perret, E., and Tedjini, S., *A fully printable chipless RFID tag with detuning correction technique*, IEEE Microwave and Wireless Components Letters, 2012, **22**(4): 209–211.
132. Kalansuriya, P., Karmakar, N. C., Viterbo, E., *On the detection of frequency-spectra-based chipless RFID using UWB impulsive interrogation*, IEEE Transactions on Microwave Theory and Techniques, 2012, **60**(12): 4187–4197.
133. Wheeler, H. A., *Inductance formulas for circular and square coils*, Proceedings of the IEEE, 1982, **70**(12): 1449–1450.

134. Matsuzaki, R., and Todoroki, A., *Wireless flexible capacitive sensor based on ultra-flexible epoxy resin for strain measurement of automobile tires*, Sensors and Actuators A: Physical, 2007, **140**(1): 32–42.

Abstract in Korean

스트레인 및 진동 측정을 위한 직접 인쇄 나노물질 센서

민 수 홍

서울대학교 일반대학원

기계공학부

4차 산업혁명에 대한 대부분의 논의는 많은 양의 데이터를 처리하고 평가하는 시스템을 암묵적으로 가정한다. 특히, 복잡한 생산 공정을 운영하기 위해서는 안정적이고 신뢰할 수 있는 데이터 측정 및 통신 시스템이 필요하다. 하지만, 최신 센서 기술은 광범위한 기계 및 생산 공정 중 데이터를 수집하는 것이 가능하지만 측정하기 쉽지 않은 데이터를 측정하고 분석하여 그 결과를 최적화된 생산 공정에 신속하게 제공하는데 한계를 가지고 있다. 때문에, 유연하고 적응 가능한 제조 공정을 위한 센서의 가격과 설치 방법, 데이터 수집 및 전송 시스템이 실제 산업의 요구 사항에 도달하지 못하고 있다.

이 학위 논문에서는 유연 기판에 전도성 및 신축성 패턴을 직접 인쇄할 수 있는 공기역학적 나노물질 집속 인쇄 시스템을 사용하여 높은 민감도와 넓은 측정 가능 범위를 가진 변위 및 진동 센서를 개발하였다. 구체적으로, 은 나노입자와 다중 벽 탄소 나노튜브로 구성된 나노

복합재를 폴리디메틸실록산 위에 직접 인쇄하였다.

유연 기관 위에 공기역학적 나노물질 집속 인쇄 시스템을 사용한 나노 복합재 인쇄 방법의 기작이 기계적 균열 발생, 시드층 적층, 부분 응집 및 완전 증착 순으로 논의 및 실험적으로 검증되었다. 인쇄된 나노 복합재 센서는 58.7의 게이지 팩터, 0.74의 측정 가능 범위를 나타내었으며 1,000번 반복된 수명 주기 평가에서 5% 미만의 정점 저항 변화를 확인할 수 있었다. 또한 Q 인자 평가 및 통계 검증을 사용하여 진동의 진폭 및 주파수에 따른 진동 측정 성능을 평가하였다.

나노 복합재 센서에 대한 측정 기작 또한 해석적 및 통계적 방법으로 분석되었다. 먼저, 나노물질 간 터널 효과가 이변량 프로빗 모델을 통해 통계적으로 분석되었다. 센서의 전기적 물성이 나노물질의 기하학적 물성에 따라 상이하기 때문에 변위에 따른 나노물질의 동적인 이해를 위해 레너드존스 전위 및 유권자 모델을 기반으로 한 몬테카를로 시뮬레이션 방법이 개발되었다. 이를 활용하여 나노물질 간 평균 부착 수를 계산하여 낮은 비용으로 전기전도도를 추정할 수 있었다.

첨단 제품을 제조하기 위한 모든 공정의 주요 목표는 지정된 범위의 허용 가능한 변동을 준수하는 것이다. 이를 위해 공정 중 어디에서나 상태 변경의 증거를 제공할 수 있는 모든 데이터를 기록하는 것이 필수적이다. 이 학위 논문에서는 제작된 센서를 통해 성형 및 절삭 공정의 데이터를 기록함으로써 공정을 모니터링하였다. 성형 공정 동안 스탬프의 기계적 변형을 측정함으로써 최대 힘, 힘의 구배 및 판금의 두께를 포함하는 다양한 공정 변수에 따라 성형 힘을 추정할 수 있었다. 또한, 절삭 공정 중 공작물에 제작된 센서를 직접 부착하여 정확하고 안정적인 진동 모니터링을 수행하였다. 얻어진 데이터의 주파수 및 전력 스펙트럼 분석을 이용하여, 분당 회전 수, 이송 속도, 스핀들의 절삭

깊이 및 너비에 따른 공작물의 진동을 측정하였다. 마지막으로 제조된 센서를 진동이 제품 품질에 큰 영향을 미치는 터빈 동익 제조 공정의 디지털 트윈으로 적용하여 실시간으로 공정 결함을 예측하였다.

유선 데이터 수집 및 전송 시스템을 극복하기 위해 칩리스 무선 주파수 식별 기술을 사용하여 직접 인쇄된 무선 통신 센서를 개발하였다. 칩리스 무선 주파수 식별 기술은 저비용, 인쇄성 및 공정의 평이성으로 인해 사물 인터넷 장치에 널리 사용되는 기술 중 하나이다. 개발된 유연한 칩리스 센서는 0.6 이상의 게이지 팩터와 0.2 이상의 측정 가능 범위를 나타냈다. 또한 제작된 센서는 한 방향의 변위만 독립적으로 측정할 수 있는 특성을 가지고 있기 때문에, 모든 방향의 수직 및 전단 변형을 측정할 수 있는 다양한 공진 주파수로 구성된 센서 패치가 개발되었다.

기계 및 장비의 센서는 실제 값이 공차 범위에 속하는지 여부에 대한 중요한 단서를 제공할 수 있다. 이러한 측면에서, 정확하고 신뢰할 수 있는 실시간 공정 모니터링은 지능형 제조 공정 및 디지털 트윈으로의 응용을 위한 기본적이고 결정적인 요소이다. 이 학위 논문에서 개발된 센서는 낮은 제조 비용과 높은 민감도 및 신축성을 가지고 있기 때문에 성형 공정, 절삭 공정, 무선 통신을 포함한 다양한 제조 공정에서 응용되었다. 뿐만 아니라 제작된 센서는 디지털 트윈 및 공정 결함의 실시간 예측을 위해 다양하게 사용될 수 있을 것으로 예상된다.

주요어: 센서, 나노물질, 공기역학적 나노물질 집속 인쇄, 민감도, 신축성, 제조 공정 모니터링, 스마트 제조

학번: 2016-20684